HYBRID CUTTING EXTRUSION OF COMMERCIALLY PURE ALUMINUM ALLOYS

by

Mohammed Naziru Issahaq

A Dissertation

Submitted to the Faculty of Purdue University

In Partial Fulfillment of the Requirements for the degree of

Doctor of Philosophy

School of Materials Engineering

West Lafayette, Indiana

May 2021

THE PURDUE UNIVERSITY GRADUATE SCHOOL
STATEMENT OF COMMITTEE APPROVAL

Kevin Trumble, Chair
School of Materials Engineering

Srinivasan Chandrasekar
School of Industrial Engineering

David Johnson
School of Materials Engineering

Xinghang Zhang
School of Materials Engineering

Approved by:
Dr. David Bahr

Dedicated to my Mom, Wife and Daughter

ACKNOWLEDGMENTS

All Praise be to Allah, who has equipped me with the strength, resilience, and fortitude throughout my journey in this program.

I would like to thank my advisors, Prof. Kevin Trumble, and Prof. Srinivasan Chandrasekar, for all the inspiration, support, guidance, criticisms, and motivation you have gave me throughout my research. You laid for me a solid foundation to grow and settle into my research and further gave me reason to believe in my ability to get this done and done well. Thank you! I would also like to thank Profs. Johnson and Zhang for making themselves available for any additional guidance and support I needed in my research.

I have high praise for all my friends who have maintained faith in me and provided the motivation and support I needed to keep going even in the direst of circumstances. I cannot thank all my colleagues in our research group enough, for our idea-sharing sessions and the casual tête-à-tête that strengthened our ties beyond research. You made this possible for me.

Finally, and most importantly, I would like to thank my wife, Sahada Issah, for all her patience, love, motivation, resilience, and belief in our endeavor. You simply made life worth living. Fareeda and I thank you very much for keeping our household. Our hay days are just beginning!
I will also want to thank my Mom, Hajia Rabi, and all my siblings for keeping faith in me and supporting me with prayers. May Allah grant us the benefit of our toil and strengthen the string that binds us together as a Family.

This work was supported in part by NSF grants CMMI-1562479 and DMR-1610094 and the US DOE-EERE program via Award DE-EE0007868. We would like to thank Prysmian Group (General Cable), Indianapolis for providing us with commercial samples of the 1350 and 8040 aluminum alloys and for all the discussions we had.

TABLE OF CONTENTS

LIST OF TABLES

LIST OF FIGURES

LIST OF SYMBOLS

LATIN SYMBOLS

FM	Free Machining
HCE	Hybrid Cutting Extrusion
HV	Vickers hardness
k	Shear strength
T	Temperature
t_o	Uncut chip thickness
t_c	Chip thickness
w_c	Chip width
V	Velocity
L_{ct}	Chip-tool contact length
TD	Transverse Direction
RFN	Rake face Normal
CFD	Chip Flow Direction
c	Specific heat capacity
F	Force
Us	Shear energy per unit volume
FFT	Fast Fourier Transform
PSD	Power Spectral Density
Rmax	Maximum peak-to-valley height
PIV	Particle Image Velocimetry
ROI	Region of Influence
L_{sk}	Sticking length
L_{sd}	Sliding length
PDZ	Primary Deformation Zone
SDZ	Secondary Deformation Zone
R_a	Arithmetic mean height
R_q	Root mean square height

R_p	highest peak of a surface profile
R_v	Lowest valley of a surface profile
S	peak density parameter
S_m	Zero crossings parameter

GREEK SYMBOLS

α	Rake angle
ε	Effective strain
λ	Chip thickness ratio
φ	Shear angle
ρ	Density
Γ	Fraction of heat, generated at the shear plane, that enters of the workpiece

ABSTRACT

Commercial sheets, strips and wires are currently produced from aluminum alloys by multi-step deformation processing involving rolling and drawing. These processes typically require 10 to 20 steps of deformation, since the plastic strain or reduction that can be imposed in a single step is limited by material workability and process mechanics. In this work, a fundamentally different, single-step approach is demonstrated for producing these aluminum products using machining-based deformation that also enables higher material workability in the formed product. Two process routes are proposed: 1) chip formation by Free Machining (FM), and 2) constrained chip formation by Hybrid Cutting Extrusion (HCE).

Using the very soft and highly ductile commercially pure aluminum alloys as representative systems, various material flow transitions in response to the concentrated shear deformation are observed in FM including plastic instabilities. The flow instabilities usually manifested as folds of varying amplitudes on the unconstrained surface of the chips, are features that limit the desirability of the chip and potential use for strip applications. To suppress these instabilities, two strategies both involving deformation geometry design are outlined: 1) By using large positive rake angle, the flow can be transformed to be more laminar and thus reduces to a substantial amount, the flow instabilities. This also makes it possible for light rolling/drawing reductions to be adopted to smoothen the residual surface folds to improve the strip finish. 2) By using a constraining tool coupled with the cutting tool in what is referred to as HCE, the initial instability that leads to plastic buckling of the material is suppressed, thereby making the flow laminar and thus improve the quality of the strips.

Key property attributes of the chips produced by the shear-based deformation processes such as improved mechanical properties and in the case of HCE, superior surface finish compared to conventional processes of rolling/drawing are highlighted. Implications for commercial manufacture of sheet, strip and wire products are discussed.

1. INTRODUCTION

Aluminum is one of the most relevant metals used in modern societies. The combination of its physical and mechanical properties has resulted in its use in a wide variety of products, many of which are indispensable to modern life. For instance, due to its light weight and high electrical conductivity, aluminum wires have gained prominence for use in long distance transmission of electricity over its main copper counterpart [1]. The combination of strength, low weight and high workability has increased the use of the metal in transportation systems including light vehicles, railcars and aircrafts as the desire to increase fuel consumption efficiency becomes ever important in the transportation industry [2–4]. Aluminum has also found usefulness in the area of air conditioning, refrigeration, and heat exchange systems due to the excellent thermal properties and resistance to corrosion. In addition, the excellent malleability (ductility) of aluminum makes it easier for shape transformation through rolling and drawing into thin sheets for use in the packaging, aerospace and automotive industries [5]. Many applications of aluminum alloys require strip, sheet, and foil forms of the material.

Generally, the specifications of physical and mechanical properties of aluminum alloys tailored for any application is achieved by alloying and processing. More than three hundred alloy compositions are commonly recognized, and many additional variations are being developed [6,7]. Therefore, alloy nomenclature and temper designation were developed by the Aluminum Association to classify the alloys and the various processing treatments that are carried out on the alloys [6]. Table 1.1 shows the general classifications of the alloys.

The processing treatments on the other hand, are encapsulated in the temper designation which permits an understanding of the manner in which a product from the alloys system has been fabricated [6]. The designation is based on a sequence of mechanical or thermal treatment, or both, used to produce the various conditions. The main letters used are: O – annealed, F – as fabricated, H – Strain hardened, T – Thermally treated and W – Solution heat treated (**Table 1.1**) [8].

Table 1.1 Aluminum alloy system [9,10]

Alloy Series	Principal Alloying Element	Temper Designation
1xxx	Unalloyed (≥ 99.0% Pure)	H
2xxx	Cu	T/W
3xxx	Mn	H
4xxx	Si	H/T
5xxx	Mg	H
6xxx	Mg+Si	T/W
7xxx	Zn	T/W
8xxx	Open category	H/T/W

Based on these designations, alloys can be differentiated in relation to the primary mechanism of property development, or the designations can be used as processing blueprint to tailor or select the properties of alloys for specific applications. For instance, in electrical conductor applications, alloys within the 1xxx and 6xxx are generally preferred. But, the latter, which promises higher strength through precipitation hardening in heat treatment, suffers slightly lower electrical conductivity compared to the commercially pure 1xxx alloys. On the other hand, tending to their high purity due to low alloying content, the commercially pure 1xxx alloys, have high electrical conductivity but low strength and therefore are strengthened through strain hardening. In fact, the strengthening mechanism of strain hardening is intrinsic to the deformation (shape change) processing in the 1xxx alloys and as a result, draws in the current motivation to adopt machining-based deformation as a processing technique for transforming bulk forms such as sheets, strip and wire products.

Conventionally, plastic deformation techniques such as cold rolling and wire drawing are the primary processes used for producing the strip and wire products from the 1xxx alloys [8,9]. However, these deformation techniques, despite attractive benefits like high production rate and capacity for continuous production, also have disadvantages. The latter arise from the fact that the processes are typically multi-stage/pass processes, with high logistical and energy requirements; offer only limited control of microstructure and crystallographic texture due to less than adequate controllability of deformation path; and are sometimes difficult to apply to alloys of poor workability. For these reasons, we are exploring alternative deformation processing routes that can produce sheet and strip in a single process step, such as via machining-based deformation processing. The challenge, however, lies in the fact that the 1xxx have “poor machinability

(workability)" despite their low strengths (UTS < 90 MPa), and high ductility (elongation > 40% in 50 mm) [10]. This is because the large ductility tends to promote "gummy" flow behavior under shear deformation. The occurrence of the gummy flow behavior has been attributed to a highly sinewy mesoscale deformation mode – sinuous flow - in simple shear deformation of these alloys. The sinuous flow is characterized by unsteady flow with significant rotation components and large-amplitude material folding in the deformation process zone. This shear deformation flow behavior of these gummy alloys is an intriguing phenomenon and merits further exploration especially in the context of strip and wire making; the latter constitutes the focus of this study.

Two machining-based deformation techniques, Free Machining (FM) and Hybrid Cutting Extrusion (HCE) are explored for production of strip, sheet and foil using model alloys from the 1xxx series. Unlike regular machining processes where the emphasis is on the workpiece, the present techniques focus on chip formation primarily as a means for producing strip and foil for flat-wire applications. This requires solution of the gummy machining problem, that is tailoring of the plastic flow to be uniform and laminar, by suppressing the sinuous flow mode and associated flow instabilities. The work builds on prior successes of these techniques in producing bulk foil and strip forms, with fine-grained microstructures and improved mechanical properties (strength and formability) from structural alloys such as magnesium, copper, aluminum and iron [11–13].

1.1 Problem Statement

The challenge with the 1xxx alloys, as already indicated, involves the ease with which good strips can be produced from the alloys by machining. Typically, chip formation by machining involves intense shear deformation and as a result, work materials depending on their initial condition, tend to have different responses to the machining conditions. The mode of plastic flow in the chip during the deformation is a direct consequence of the nature of the chip surfaces that are produced. Plastic instabilities in general, play a role in machining especially in metals of low-to-medium workability such as hard steels, Ti, and Mg alloys where the deformation is typified by ductile failure and shear banding resulting in chips with segmented and saw-tooth surfaces [14]. In the very ductile alloys, however, the flow instabilities in cutting are completely different. Although at first glance they appear very workable and indeed they may be so in the conventional sense, but the high ductility and strain-hardening capacity of these alloys promotes a plastic flow behavior that is highly unsteady in simple shear deformation. These flow modes are typically characterized by material folding, extensive redundant deformation, and vortex-like flow components. This results in extreme thickening of the chips with a propensity for side flow, a characteristic often referred to as 'gummy'. The flow instability, typically buckling, is usually manifested as folds of varying amplitudes on the unconstrained surface of the chips (**Fig. 1.1**). The fold features limit the desirability of the chip for strip applications.

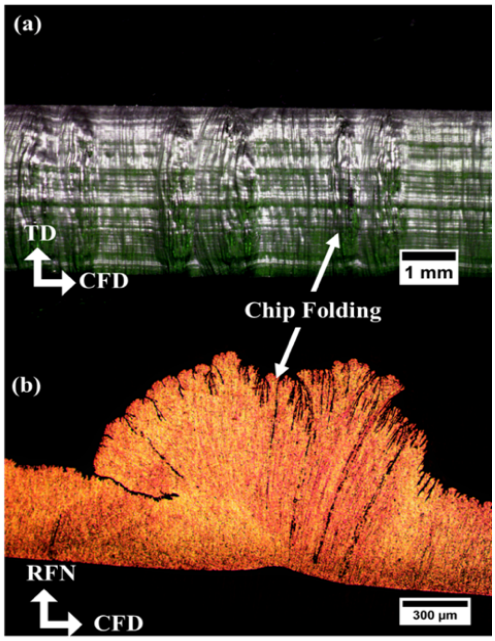

Fig. 1.1 Large amplitude folding typical of dry cutting of soft aluminum. a) Shows the rake face normal (RFN) view of the chip, b) views a single fold in the transverse direction (TD). CFD is the chip flow direction.

The aluminum alloys of the 1xxx type exhibit these unstable flow characteristics. Hence, we use this alloy system to examine the flow instabilities and the underlying mechanics. Based on this examination, we formulate approaches on how to reduce or possibly suppress the instabilities in a deformation framework so that we can get good quality strips. Two flow control strategies, both

involving deformation geometry design, are outlined: 1) Firstly, by using a tool with a large positive rake angle, we show that the flow can be transformed to be more laminar and steadier, and thus reduce the folding features on the free surface of the chip. This makes it possible for subsequent light rolling/drawing reductions to be adopted to smoothen the residual surface folds and improve the strip finish to usable quality. 2) Secondly, by constraining the chip formation using a second constraining tool that is coupled with the cutting tool – Hybrid Cutting Extrusion (HCE) – we show that the initial plastic buckling instability that causes material folding can be suppressed. This makes the plastic flow quite laminar, enabling high-quality strips.

The origins of the flow instability and surface fold formation are investigated using *in situ* imaging and Particle Image Velocimetry (PIV) analysis. Various attributes of the process such as multiscale folding, topography of the strip, and mechanical and physical properties of the strip (chip) are characterized via surface metrology, optical and scanning electron microscopy, hardness and electrical conductivity measurements. Implications of the techniques as viable strip and flat wire making processes are discussed.

2. FUNDAMENTALS OF METAL CUTTING

This chapter provides the historical evolution of machining as a manufacturing process. The first part looks at the history of machining through the ages. The second part introduces modern machining techniques including Free Machining (FM) and Hybrid Cutting Extrusion (HCE).

2.1 Historical Background of Machining

The technology of machining has an enormous historical and economic range. While metal cutting dates back to the industrial revolution, it keeps extending its frontiers in response to everyday needs for a wide range of industries [15]. For standard consumer products such as cars, aircrafts, and household applications, metal cutting remains the primary production method. Increased competition by industries in the manufacture of these basic consumer products has demanded greater efficiency and productivity, a challenge that has motivated for the constant transformation of machining technology.

While there is no precise definition for metal cutting or machining, the term is intended to include operations involving the removal of a thin layer of material, the chip, from a bulk workpiece by the use of a wedge-shaped tool [16]. There are no hard-lines separating chip forming operations such as shearing, punching, and cropping. These also are metal cutting processes, but the action of the tools and the process of cutting are different from those of chip-forming operations [17]. In the engineering industry, machining is used to cover chip-forming operations and this definition appears in many dictionaries [18,19]

Before the middle of the 18^{th} century, wood was the main material used in engineering applications [20,21]. However, the boring of cannons and the production of metal screws and small instrument parts were exceptions; these processes required metal tools. The steam engines, with its large metal cylinders and other parts that required unprecedented dimensional accuracy, led to the first major developments in metal cutting in the 1760s [15]. At the inception of the steam engine, no machine tool industry existed. Between 1760 to 1860, industries dedicated to the production of machine tools began to spring up [22]. Henry Maudslay and Eli Whitney, among many other great engineers, made threads, grooves, slots and holes in metallic components, that were required by

developing industries [23–25]. The lathe, milling machines and drill machines all developed into the rigid equipment, capable of turning out large amounts of accurate parts that had never been possible [15,25]. Shown in Fig. 2.1 is the Maudslay's first screw-cutting lathe.

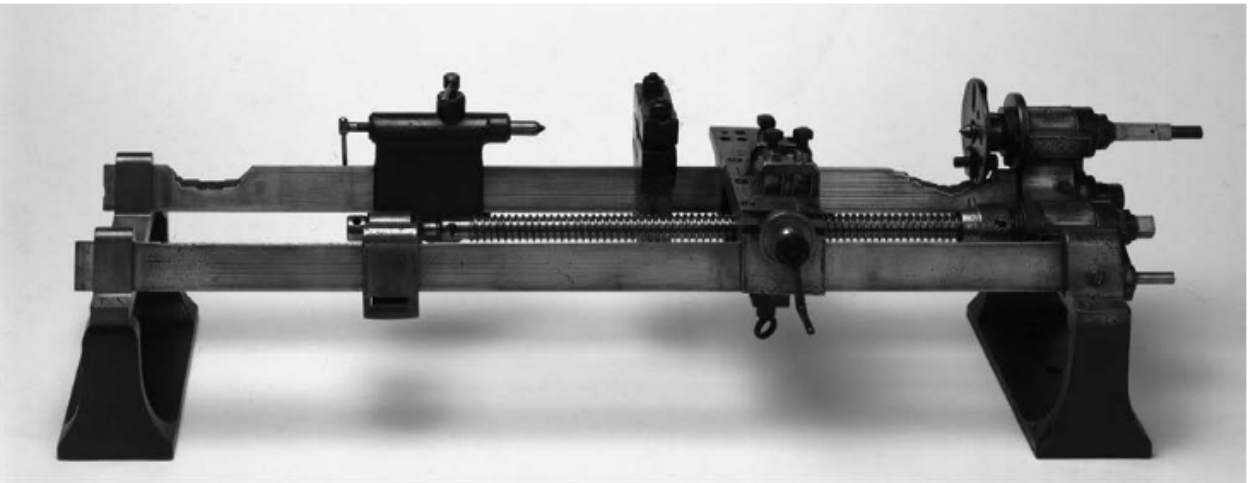

Fig. 2.1 Henry Maudslay's first screw-cutting lathe of 1797 [22,25]

From the mid-1880s onwards, innovation in manufacturing shifted from developing machine tools to cutting new types of metals at reduced costs [15]. Wrought iron which was the workhorse of construction materials was replaced by steel. As the evolution of machining technology evolved in response to the needs of our industrial civilization, many new alloys have been developed [26]. Some of these materials such as aluminum and magnesium are easy to cut, but others such as high-alloy steels, and nickel-based alloys are more difficult to cut due to their high strength [12,27–29].

In recent years, materials processed by cutting have expanded to non-metal materials, such as ceramics and glass; although, metals are still the most important materials used for machining [30,31]. Today, cutting technology is quite mature with increased complexity and machining precision for a wide variety of machined products. Adapting to the rapid development of cutting technology has increased the systematic research on the basic theory of metal cutting, which also has more than a century worth of history [17]. Over this period, countless researches conducted in metal cutting theory have guided and facilitated the development of cutting technology and machining [20,32–34].

2.2 Fundamentals of Chip Formation

Chip formation by machining is a concentrated shear-based deformation process occurring by the action of a hard cutting tool against a workpiece. **Fig. 2.2a** shows a schematic of the basic operation in Free Machining (FM). The process is called FM, for emphasis here, because the exit chip thickness (t_c) is not set *a priori* but determined by the nature of the (unconstrained) deformation process. Ideally, the workpiece is held in the chuck of a lathe and rotated. The cutting tool is held rigidly and moves at a constant feed rate into the rotating workpiece, cutting away a layer of material in the form of a chip from the surface of the workpiece. The major operating parameters specified in the chip formation process include, but are not limited to, the tool geometry, the cutting speed (V_o), and the feed (f).

Fig. 2.2b shows the main features of a wedge-shaped cutting tool. The rake face is the surface over which the chip flows. The cutting edge is formed at the intersection between the rake face and the clearance face. The need for the clearance face is to avoid the rubbing of the face against the freshly cut workpiece surface. The clearance angle is often varying between 6-10^o [35]. The rake face is inclined at an angle (rake angle, α) which can be adjusted to achieve optimum cutting performance depending on the particular tool material, workpiece materials and cutting conditions. Both positive and negative rake angles can be used for cutting operations. Large positive rake angles make easy cuts but often lead to accelerated tool damages. On the other hand, smaller rake angles (zero or negative angles) offer greater robustness of tools thereby limiting tool damages [15].

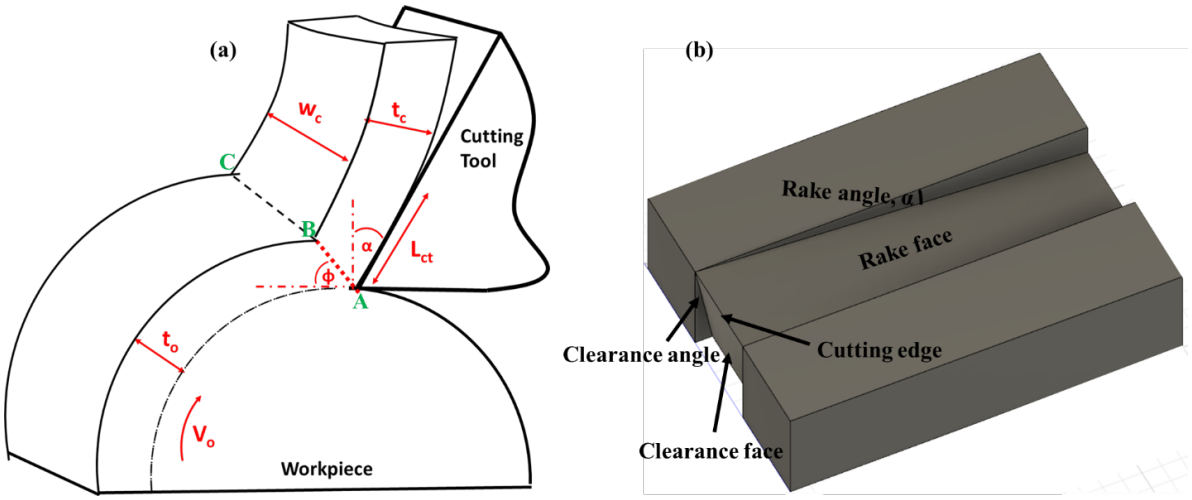

Fig. 2.2 Schematics showing a) a basic cutting operation in FM involving a cutting tool and a workpiece, b) a wedge-shaped tool geometry highlighting the essential features of the tool.

In the lathe, the workpiece is rotated by the action of a rotating spindle. The cutting speed V_o, is therefore, determined by the rotational speed of the spindle, N and the initial and final workpiece diameters, d_1 and d_2 (**eq. 2.1**) [22].

$$V_o = \pi N\left(\frac{d_1 + d_2}{2}\right) \tag{2.1}$$

The feed (f) is basically the tool advancement into the workpiece per revolution along its cutting path. In FM, this is the same as the undeformed chip thickness (t_o). This is typically measured in mm/rev. The feed rate (f_r), therefore, is the speed at which the tool advances into the workpiece in mm/min. These two parameters are related by the spindle speed, N (**eq. 2.2**) [22].

$$f_r = fN \tag{2.2}$$

2.3 Nature of Chips in FM

Machined chips largely vary in shape and size (**Fig. 2.3**). The formation of the different types of chips involves the response of the work material to the shearing phenomenon that occurs in a region extending from the tool edge to the upper surface of the chip (see ABC in **Fig. 2.2a**). A very large amount of strain occurs in this region in a very short period of time, and not all metals

and alloys can withstand this strain without fracture. Whereas certain materials such as some alloys of brass and magnesium will produce discontinuous (discrete) chips, many alloys of copper, aluminum, and steel tend to produce continuous chips. Based on the material and cutting conditions, continuous chips may adopt many shapes - straight, coiled, or with different forms of helix (**Fig. 2.3**).

Fig. 2.3 An image showing chip types and shapes. Depending on material and cutting conditions, some chips are discrete, others are continuous with varying shapes including straight, coiled and helically wound shapes.

The material flow response to the intense shear deformation is also often reflected in the thickness of the chip which is used as an estimate of the deformation strain. The challenge, however, is that the cross-sections of the chips are usually not regular. Typically, the chip thickness is greatest in the middle and tapering off towards the sides due to minor side spread (**Fig. 2.4**). Although, in wider chips where the chip width $\geq 10t_c$, plane strain conditions may be imposed on the chip to limit the extent of the side spread, thus generating chips with near perfect rectangular cross-sections. In narrow chips however, the side spread persists, making the complete description of the chip quite complex.

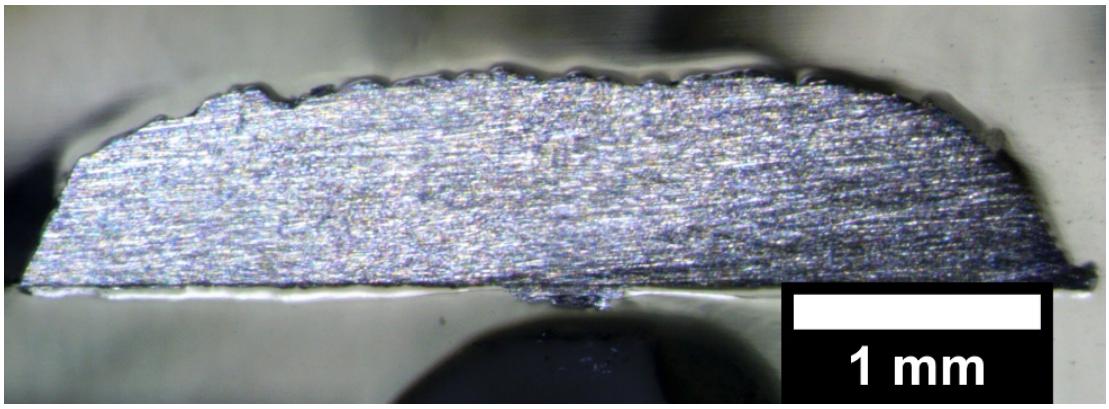

Fig. 2.4 An image showing the irregular cross-section of FM chips.

Due to the unconstrained nature of the FM deformation, the free surface of the chips are also always somewhat rough, with minute corrugations and periodic cracks [36]. A superficial examination of many of these chips may lead one to innumerable classification of the chips based on their morphologies. But through a more detailed examination of the chips, Nakayama grouped them into four principal classes as shown in **Fig. 2.5** [14]. The wrinkled back surface of type 1 is peculiar to ductile alloys (e.g., Al, Cu etc.), while type 2 is regularly seen in strain hardened materials. Both type 3 and 4 produce saw-tooth structures which typically occur in materials with limited ductility such as in Ti and some alloys of Brass and Mg [36,37]. These irregularities, therefore, makes many details of the chip to be ignored by assuming a rectangular cross-section whose height is the measured mean chip thickness along the length of the chip, and width equal to the depth of cut. The avoidance of many of these irregularities motivated for the development of a variant of the FM model, Hybrid Cutting Extrusion, HCE [38,39].

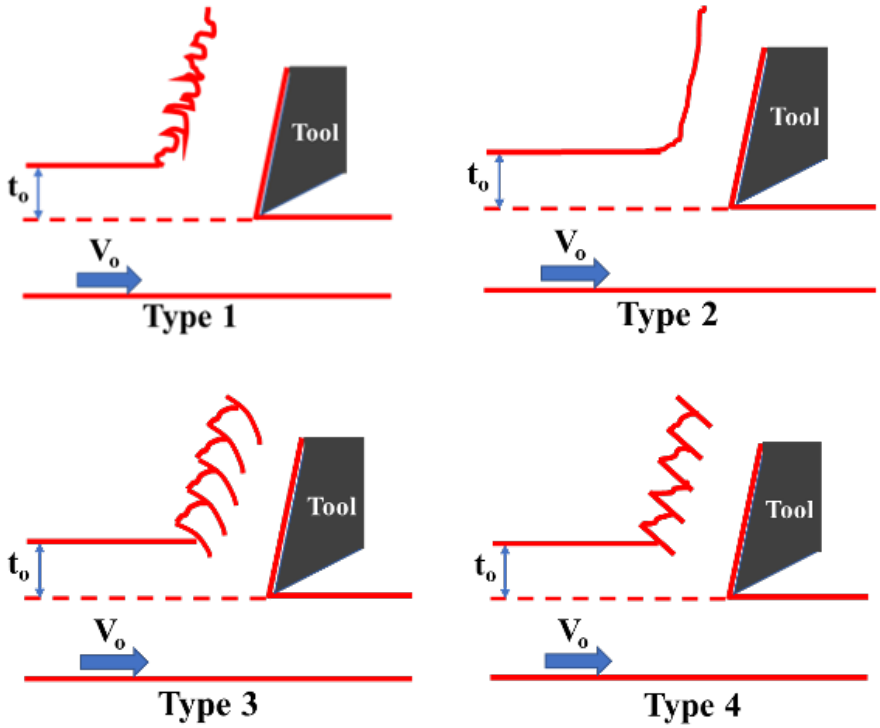

Fig. 2.5 Schematics of the four principal chip types. Type 1 regularly seen in soft and highly ductile metals, Type 2 seen in strain hardened materials, Type 3 and 4 typical of low-to medium strain hardening materials. After [36,37,40].

2.4 Hybrid Cutting Extrusion (HCE)

In FM, the chip is formed by feeding the cutting tool, set at a rake angle (α), radially into a rotating workpiece, at preset undeformed chip thickness (feed), t_o, as shown in **Fig. 2.6a**. This produces a chip of thickness, $t_c > t_o$, formed by intense shear confined to a narrow region called the Primary Deformation Zone (PDZ) (AB in **Fig. 2.6a**). The exaggerated corrugated surface in the schematic (**Fig. 2.6a**) is meant to highlight the irregularities associated with the FM chip as indicated previously. In HCE, a constraining tool that is located directly across from the main cutting tool (**Fig. 2.6b)** is adopted to set the exit chip thickness (t_c) *a priori*. The chip exit channel (now an extrusion opening) allows for a hybrid cutting and extrusion in a constrained deformation. The chip thickness is not only controlled by the process, but it can also be set even smaller than t_o, a control which is not feasible in FM.

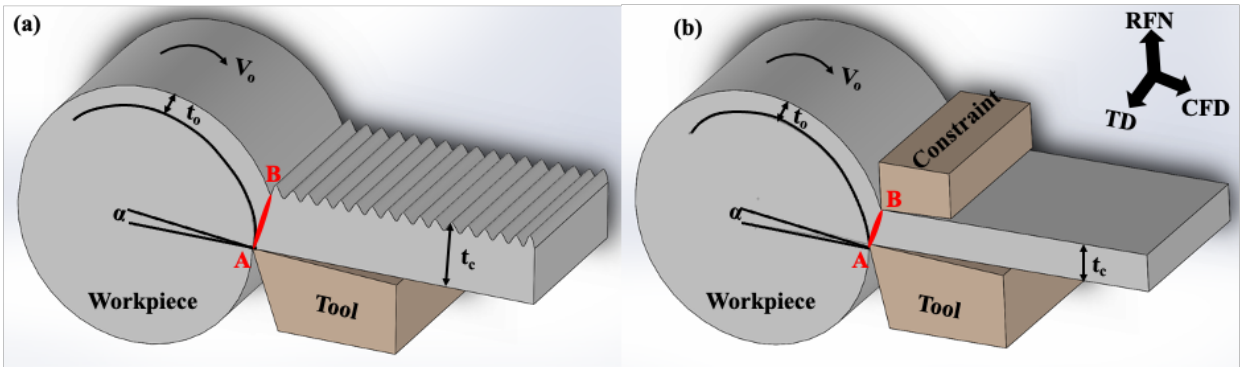

Fig. 2.6 Rotary configured schematics of plane-strain shear-based deformation processing in a) FM and b) HCE. The tool is fed radially into the workpiece to produce the chip. Various process variables are defined; primary deformation zone AB is shown in red. RFN, TD and CFD are the Rake Face Normal, Transverse and Chip Flow directions, respectively.

2.5 Deformation Mechanics of FM and HCE

The mechanism of chip formation is by a process of shear which is approximately confined to a single plane extending from the cutting edge to the workpiece surface ahead of the cutting tool (see primary deformation zone (PDZ), AB in Fig. 2.6). By idealizing the PDZ as a plane of infinitesimal thickness - a shear plane, the von Mises effective strain imposed in the chip is obtained, based on upper-bound analysis, as [33,39].

$$\varepsilon = \frac{1}{\sqrt{3}}\left(\frac{\lambda}{\cos\alpha} + \frac{1}{\lambda\cos\alpha} - 2\tan\alpha\right) \tag{2.3}$$

where the chip thickness ratio, $\lambda = {}^{t_c}\!/_{t_o}$. Strains of 1 to 10 can be imposed in the chip in a single deformation pass using these processes.

Unlike conventional cold rolling and drawing processes, the strain imparted in FM and HCE can be controlled independent of the final chip thickness, via α and λ. In FM, λ increases with decreasing α, but is otherwise governed by the material deformation response; the more ductile alloys tend to give larger λ and thus a higher strain at a given α. Whereas, in the HCE, both α and λ (and thus chip thickness and strain) can be set *a priori* (**Fig. 2.6**). For any given rake angle, the minimum strain occurs at a $\lambda = 1$. In fact, the minimum effective strain (ε) at $\lambda = 1$ for $\alpha = 5^o$ (a

typical angle for cutting most metals) is 1.1 which is substantially larger than conventional processes.

Another special feature of HCE in the PDZ is the high hydrostatic pressure (**Fig. 2.7**) due to the "compression coupling" of the cutting tool with the constraining tool. The hydrostatic pressure can be determined from slip line field analysis along the deformation zone [13,41]. This pressure, normalized by the shear flow stress, k, can be as high as 3.2 if λ is made substantially small (< 1) [13] (**Fig. 2.7**). In contrast, in the deformation zone of (frictionless) conventional extrusion, it is only ~ 0.85 for a die half angle of 30° [42]. The combination of high hydrostatic pressure and adiabatic heating in HCE are favorable for alloy workability, and hence beneficial for continuous chip formation [12,43,44].

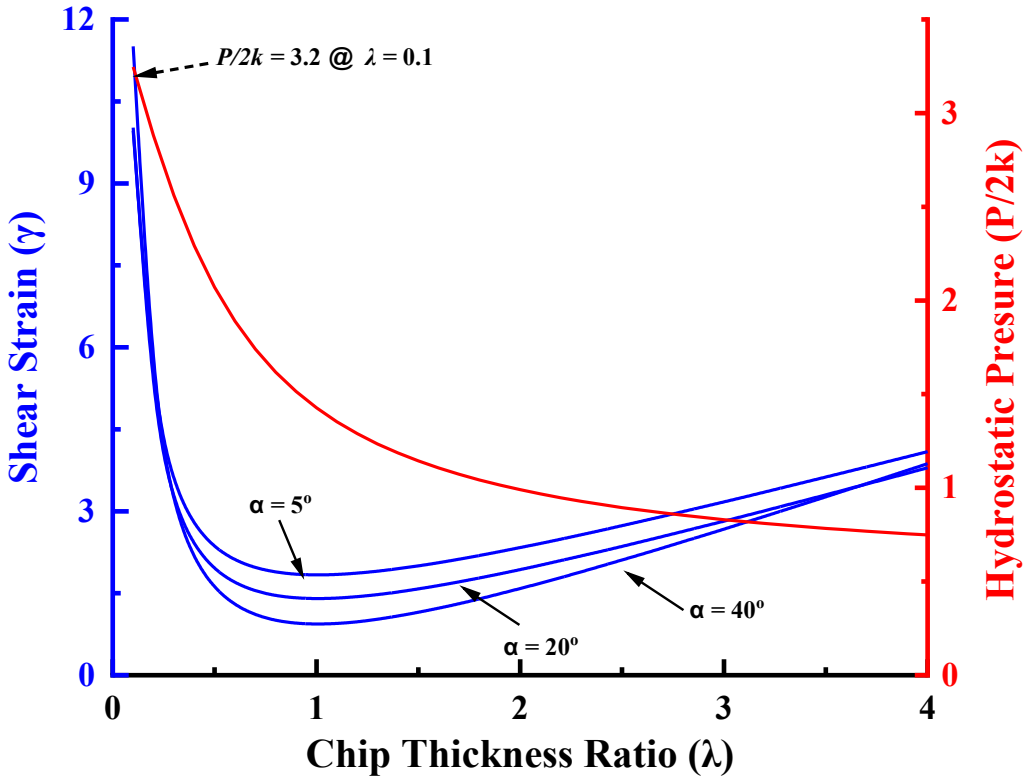

Fig. 2.7 The effect of chip thickness ratio and rake angle on the effective strains and hydrostatic pressure in HCE. The strain is minimum for any given rake angle at λ = 1 and increases steeply with decreasing λ from 1. A shallow rise in strain is observed with increasing λ above 1. The hydrostatic pressure increases with decreasing λ due to the higher constraining effect at lower λ.

Another important attribute of the HCE process is the deformation temperature. Due to the high strain rates and large deformation strains localized in the PDZ, high deformation temperatures can be achieved. The deformation temperature, T can be determined based on the shear plane model as [13],

$$T = U_s \frac{(1-\Gamma)}{\rho c} + T_o \tag{2.4}$$

Where T_o is initial temperature of the workpiece, ρ is the density of the material, c is the specific heat capacity, Γ is the fraction of heat generated at the shear plane that enters the workpiece and U_s is the shear energy per unit volume dissipated at the shear plane during the chip formation. U_s is determined by the ratio of the cutting force to the chip cross-sectional area. Γ is a function of the chip geometry, the cutting speed V_o, the chip thickness ratio λ, and the thermophysical properties of the material [13,41,45,46]. Adiabatic temperatures as high as 350°C have been obtained in cutting Fe-Si from initial workpiece temperature of 300°C [11]. Such significant rise in temperature has drastic effects on the microstructure of the chips. In fact, the commercially pure aluminum alloys, in the strain-hardened condition, are highly susceptible to recovery and recrystallization, even at temperatures as low as 80°C [8,44]. The adiabatic temperature rise, calculated based on measured cutting forces for λ = 5, in EC 1350 was determined to be in the range of 100°C to 125°C and increases with decreasing λ [44]. With greater deformation-induced adiabatic heating, the HCE chips undergo dynamic recovery or recrystallization depending on the extent of the constraint used.

As a whole, shear-based deformation allows for significant deformation control to produce continuous chips at very high strains, large hydrostatic pressures and high adiabatic temperatures. Thus, allowing for the independent control of the material properties for desired applications.

3. EXPERIMENTAL MATERIALS AND METHODS

This chapter outlines the materials and general overview of the experiments conducted in this work. Specific experimental details pertaining to any set of results will be recapped to bring the subject matter into perspective in the following chapters. The first part of this chapter presents the model materials used for the experiments, with highlights of their metallurgical state and mechanical properties. The second part looks at the deformation conditions that were imposed on the materials and the various techniques used to characterize the chips therefrom.

3.1 Workpiece Materials

Three different materials were used as our model alloys: two of which (Al 1100 and EC 1350) from the 1xxx series and the third alloy (AA8040) from 8xxx alloys. All three alloys are classified as commercially pure aluminum alloys due to their low impurity content (most importantly, Fe and Si). **Table 3.1** gives the nominal chemical composition of the alloys. The main difference between the alloys is in their impurity content levels. Whereas the maximum impurity content allowable in the 1350 is 0.5 wt% (Fe+Si), the 1100 can contain up to a maximum of 1wt%. The 8040 on the other hand, although classified as an 8xxx series alloy, is a commercially pure alloy that is analogous to the 1100 with the only difference being the addition of Zr in the composition of the 8040. The impurity content (Fe+Si) in the alloy is also capped at 1 wt% but with the Zr content ranging between 0.1 - 0.3 wt%. The addition of Zr allows for the precipitation of Al_3Zr particles that enhances high temperature strength stability of the alloy. The strength properties (hardness) for all three alloys in the soft conditions (as-cast or O-temper) are between 25 and 30 HV (**Table 3.2**). These low strength values make the alloys suitable models for the study of machining in the soft state of the aluminum alloys.

Table 3.1 Chemical composition limits for the alloys [10].

Alloy	Si	Fe	Cu	Mn	Cr	Zn	Zr	B	Ga	Others	Al
Al 1100	1.0		0.05-0.2	0.05		0.1				0.15	99.0
EC1350	0.1	0.4	0.05	0.01	0.01	0.05		0.05	0.03	0.1	99.5
AA8040	1.0		0.2	0.05		0.2	0.1-0.3				Rem

Table 3.2 Vickers hardness of the alloys

Alloy	Condition	Vickers Hardness
Al 1100	O-Temper	27 ± 2
EC 1350	O-Temper	25 ± 2
AA 8040	As-cast	28 ± 1

3.2 Workpiece Microstructure

The examination of the microstructure is a principal means of evaluating alloys to determine the effects of processing and thermal treatments on the material. For the 1xxx series alloys, annealed workpiece conditions were selected for deformation. These conditions are analogs to the as-cast condition since some of the key attributes with regard to deformation characteristics (e.g., large grain size) are quite similar. This was also necessitated by the constraint of not obtaining the two 1xxx series alloys in the as-cast condition to make direct comparison. The as-cast ingot of the 8040, however, was processed in the as-cast condition.

The fully annealed microstructures of the 1100 and 1350 workpieces are shown in **Fig. 3.1**. These initial workpiece conditions were chosen intentionally, so that process capability to make sheet and chip could be demonstrated even for alloys of low workability arising from gummy behavior. Both alloys exhibit equiaxed grain structure with average grain size of ~50 μm in the Al 1100 **(Fig. 3.1a)** and ~200 μm in the EC1350 alloy **(Fig. 3.1b)**. The variation in the grain size of the alloys after the same annealing treatment (300^{o}C/2 h), can be attributed mainly to their impurity differences. Because Fe and Si are ever-present impurity elements in Al and the solid solubility of Fe in Al is very small (0.05 wt%), phases of Al-Fe or Al-Fe-Si are seen in the microstructures of all the 1xxx alloys (**Fig. 3.1**) except for the super-pure Al [47–49]. Minor impurity elements such as Cu and Mn are not in sufficient amounts to form their own phases to influence the type and quantity of less stable phases. The higher concentrations of Al-Fe particles due to the high impurity content in the Al 1100 alloy **(Table 3.1),** inhibits recrystallization and grain growth during annealing, thus, producing smaller grains at same annealing treatment.

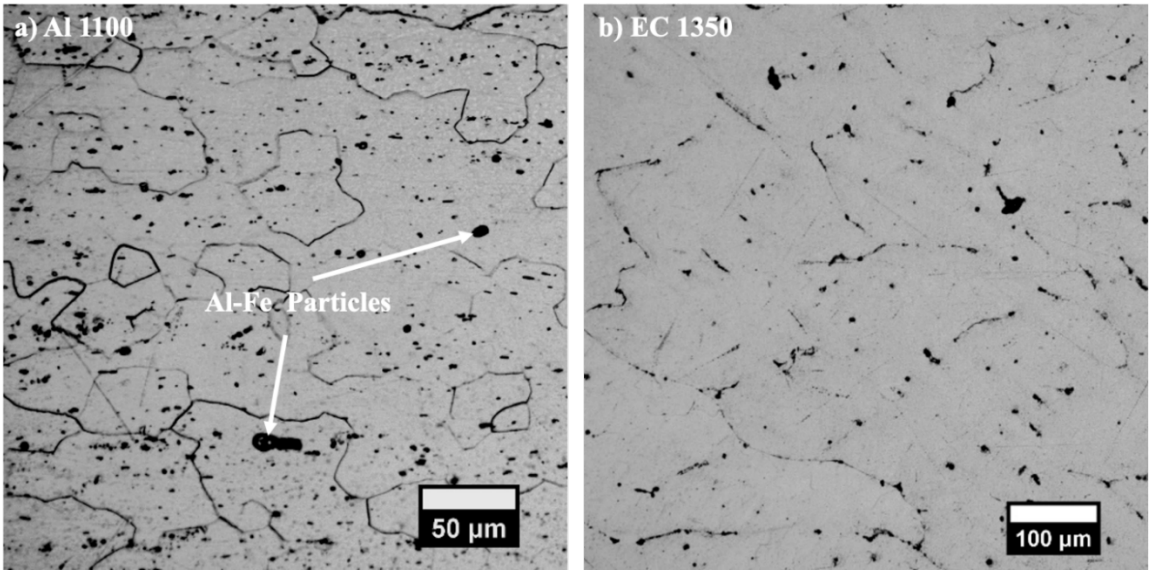

Fig. 3.1 Optical micrographs showing annealed microstructure of the a) Al 1100 and b) EC1350 workpiece disks.

For the 8040 alloy, an as-cast ingot **(Fig. 3.2a)** was acquired from Prysmian Group (General Cable), Indianapolis, IN. USA. The initial metallography revealed the cast microstructure to contain both columnar and equiaxed grains resulting from directional solidification as expected (**Fig. 3.2b**). During solidification, the columnar grains grow in a preferred crystallographic direction, opposite to the direction that heat is conducted away. Since the last bit of liquid solidifies near the center of the ingot due to directional solidification, large porosities are observed at the central regions of the ingot **(Fig. 3.2c)**. The pores may also have developed from the interdigitation of dendrite arms that restrict liquid flow. Solidification in aluminum alloys is typically dendritic, even in the commercially pure alloys because only a slight freezing range is required to enable constitutional supercooling to cause dendrite formation and consequent pore development. Traditionally, rod rolling is performed on the cast ingots to close these porosities.

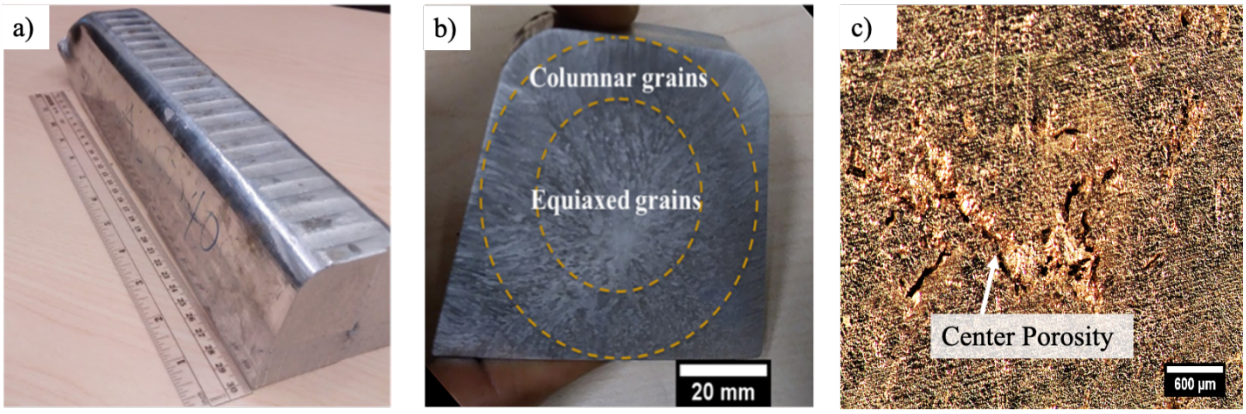

Fig. 3.2 Images showing a) the cast ingot and b) the cross-section of the ingot containing cast microstructure of equiaxed grains near the ingot center and columnar grain away from the center, c) optical stereoscope micrograph showing the porosity near the center of the of the ingot.

Quite large intermetallic particles are also prominent within the aluminum matrix of the 8040 alloy. The particles in this alloy are dispersed sparsely and in clusters **(Fig. 3.3b and c)** within the matrix. These particles are shown to have different shapes (blocky and needle-like platelets **(Fig. 3.3d)**) and ranges in size from 50 – 100 µm. Such large particles may present problems especially for wires of diameters in the range of the particle sizes (< 100 µm) or thickness for the cases of sheets or strips. Energy Dispersive Spectroscopy (EDS) spot analysis of the particles gave 78.7 at% Al and 21.3 at% Zr, which is very close to Al_3Zr.

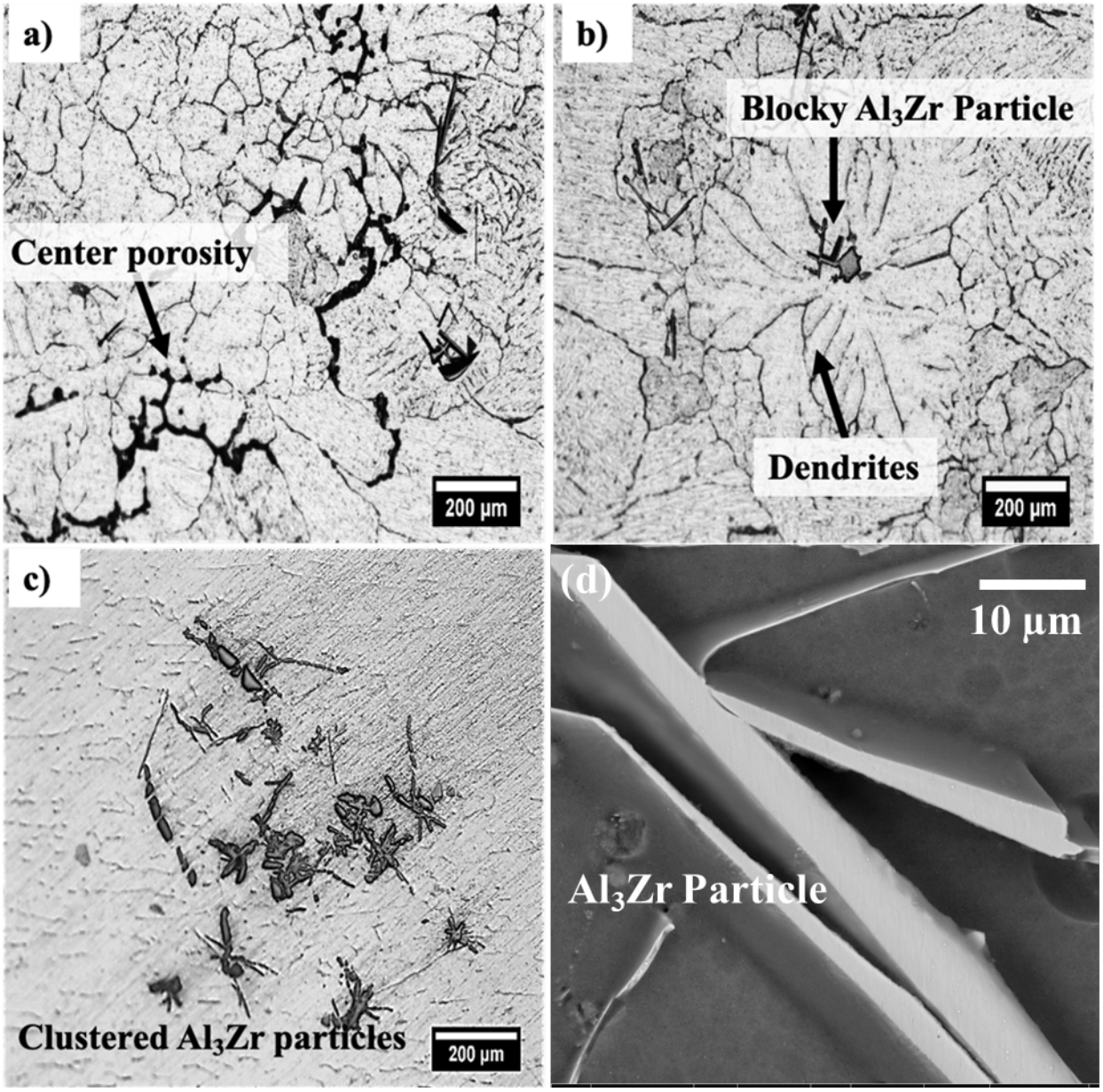

Fig. 3.3 Micrographs showing, a) the cast porosity near the center of the ingot, b) blocky Al_3Zr particles with dendrite arms around the particle, c) clustered Al_3Zr particles, and d) Platelet morphology of the Al_3Zr.

3.3 Deformation Conditions

In the plane-strain, rotary configuration of FM (**Fig. 2.2a and 2.6a**), disk-shaped workpieces, 6 mm thick x 140 mm diameter, were machined from annealed plates of the 1100 and 1350 alloys.

The 1100 workpiece disks were machined from ¼-in thick plate in the half-hard (H14) condition (McMaster-Carr, Elmhurst, IL). The EC1350 was not available in plate form. Hence, plates were produced by melting, casting, and cold rolling certified wirerod obtained from a leading flat wire manufacturer, Prysmian Group, Indianapolis, IN. The disks were then annealed at 300 ^{o}C for 2 h prior to FM and HCE. The 8040 disks were cut with a band saw and milled to the desired diameter and thickness. The prepared disks remained in the cast condition for machining. During the deformation, the cutting tool is fed radially into the workpiece at a rate of t_o per revolution. The width of the chip produced is equal to the workpiece disk thickness; therefore, any desirable chip width can be produced by adjusting the thickness of the workpiece. A range of deformation conditions were chosen for the experiments: the cutting speeds ranged between 1 m/s to 6 m/s, rake angles (α) used were between 5 and 45^{o} at initial cutting depths (t_o) ranging between 25 to 200 μm. The cutting was done dry, and forces were measured using a multi-component dynamometer with a measuring range of up to 10kN (KISTLER Type: 9257B)

In the linear cutting mode, rectangular workpieces of dimensions 65 x 45 x 6 mm were used. The workpiece was moved relative to a stationary cutting tool. A schematic of the linear setup is shown in **Fig. 3.4**. The setup consists of a glass plate that is attached to the side of the workpiece in a manner that constrains the deformation and prevents out-of-plane flow. A high-speed camera (Photron FASTCAM Mini) coupled to a compact optical microscope (InfiniFlex with high definition DS 4x lenses of 0.13 NA) is positioned at a working distance of 20 mm and focused to the deformation zone. A sequence of high resolution images is captured at a frame rate of 500 fps and collected for further processing in a computer. The image sequences were then processed and characterized using Particle Image Velocimetry (PIV) for studying the deformation flow behavior. PIV is an image correlation technique that quantifies the particle velocity fields of flow during the deformation. A relatively low cutting speed (3 mm/s) was used for rake angles between 20 and 40^{o}. In contrast to deformation in the rotary setup where cutting was done dry, the linear cutting experiments were done under lubricated conditions using oil as the lubricating medium. The cutting forces were measured using a compact dynamometer (KISTLER Type: 9254).

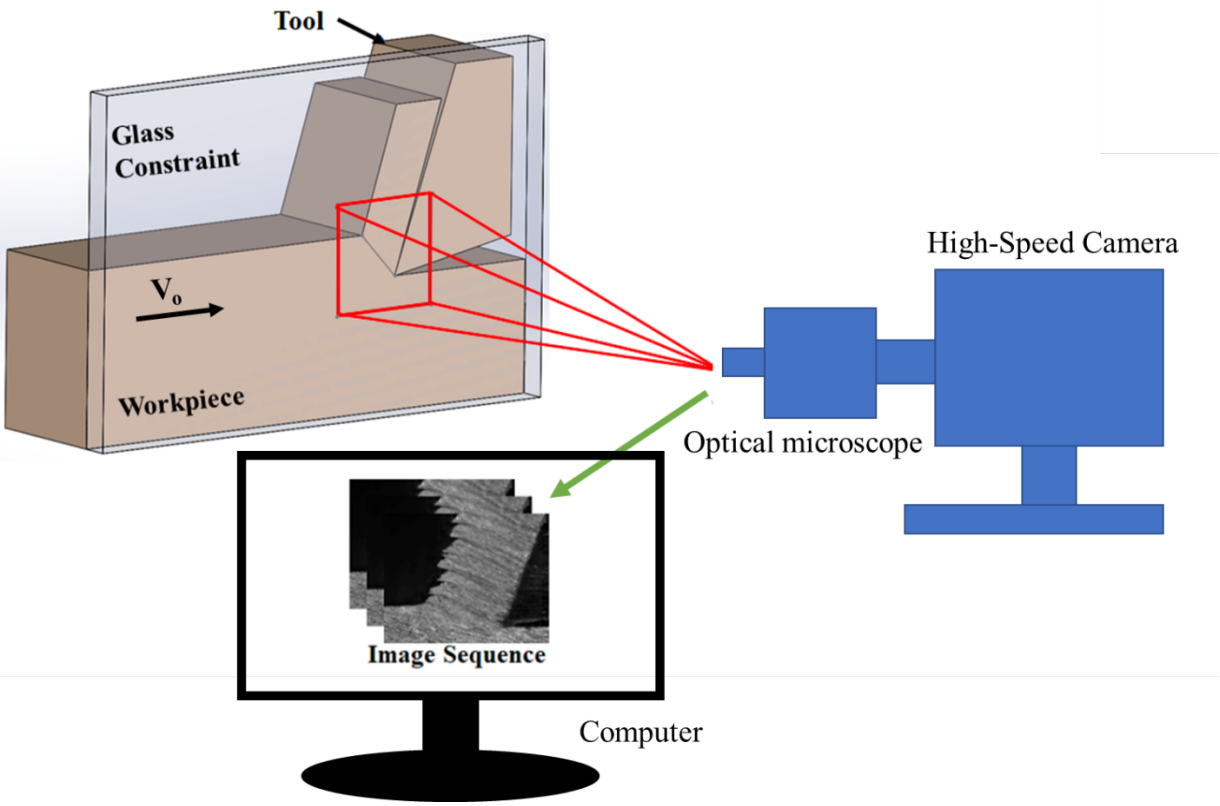

Fig. 3.4 A schematic setup for linear cutting configuration with high-speed camera for *in situ* imaging of deformation

In HCE, the conditions were set based on the flow response of the material during FM. All HCE experiments were conducted in the rotatory setup (**Fig. 2.6b**) under dry deformation conditions. Using similar cutting conditions as in FM, the thickness of the chip produced in the (unconstrained) FM, sets the upper limit for HCE chip thickness. Hence, any desirable chip thickness, lower than that of the FM chip, can be obtained in HCE by adjusting the constraint level (chip thickness ratio, λ). This capability is demonstrated in the study by performing HCE under different levels of constraint (λ value) in the range of 1-8 for natural FM chip thickness ratios (λ_{Nat}) of between 5 and 10. All cutting both in linear and rotary setups were done using high speed steel tools.

Microstructure of workpiece and chip samples was analyzed by metallography. Specimens were mounted in epoxy, polished with various grit sizes of SiC paper and finally etched in NaOH etchant for 5-10 minutes depending on the specimen. The microstructure was then studied using optical microscopy. Surface quality (topography, roughness) of the chips was measured with a 3D optical

profilometer (Zygo NewView 8000).

When chips are adopted for wire applications, two key property performance measures the wire usefulness: the strength and electrical conductivity (=1/resistivity). The strengths of the workpiece and chips were characterized by Vickers hardness measurements using a Wilson microhardness tester (Tukon 1202). At least 10 indents at 50 gf load were made on each sample; the indent separation distance was kept sufficiently large, so as to avoid any errors due to overlapping of plastically deformed regions of neighboring indents.

The electrical resistivity was determined from resistance measurements on the long continuous chips (flat wires) with gauge lengths > 0.5 m in line with ASTM B193 [50]. The 4-point probe technique, which eliminates contact and lead wire resistances, was used to achieve high accuracy in these measurements. Due to the low resistivity of the alloys, the resistance is sensitive to small variations in wire dimensions. Therefore, chip cross-sectional areas were computed from density and measured mass of the samples for given wire lengths. The electrical conductivity in %IACS (International Annealed Copper Standard) are calculated by taking the ratio of the Cu standard resistivity of 1/58 $\mu\Omega mm^2/m$ [51] to the measured resistivity of the wires. The wires were also annealed, and the microhardness and electrical resistivity measurements repeated, to determine the properties of the same wires in the O-temper condition.

4. FORMATION AND SUPPRESSION OF FLOW INSTABILITIES

This chapter focuses on the flow behavior of the soft pure aluminum alloys under the intense shear deformation in metal cutting. Flow instabilities such as fold formation, which are consequences of the material response, are highlighted. In the first part, results of multiscale folding and the mechanisms of fold formation are presented. The second part discusses various measures for suppressing the folds, including the variation of cutting parameters and the use of HCE.

4.1 Multiscale Folding in the Cutting of Soft Aluminum

The concentrated shear deformation during machining processes results in different material flow responses. This mode of plastic flow during the deformation directly determines the nature of the chip surfaces that are produced. **Fig. 4.1a and c** shows the chip surface of a soft and ductile Al chip that manifests a very distinct morphology from its less ductile brass counterpart (**Fig. 4.1b and d**). These chips surface morphologies arise from the unsteady flow of materials during the cutting process and forms the basis for the chip classifications as demonstrated previously in **Fig. 2.5**. The most common of these chip types are those that form from segmentation (**Fig. 2.5** Type 3) or from shear banding/localization (**Fig. 2.5** Type 4) [52,53]. The former which is typified by the partial forming of segments and occurrence of rupture to produce segments with periodicity that are in tune with segmentation is what is reflected in the brass chip (see segmented face **Fig 4.1d**). Segmentation was first discovered in machined chips of Ti alloys by Shaw and Rice via high-speed imaging and metallographic observations [52,53]. The chip morphology which has been widely described as “saw-tooth”, (see broken line traces in **Fig. 4.1b**) is attributed to the machining deformation behavior of metals with very limited ductility [14]. Shear banding (**Fig. 2.5** Type 4) which also causes the formation of saw-tooth chips involves the cyclic chip formation with periodic localization of the flow to a few microns thick layer, referred to as shear bands [54]. The distinction between segmentation and shear banding depends on how localized the flow is. In shear banding the chips are characterized by very narrow bands of intense shear, separated by large regions of relatively unstrained material [40]. The first observation of shear-banded chips appear to have been made independently by Shaw and Merchant [52,55], coincidentally around the same time, when they studied machining of Ti alloys [36]. Shear banded chips were also documented

later in other materials including hardened steels, Ni-based superalloys, high-strength Al alloys and magnesium [56–58].

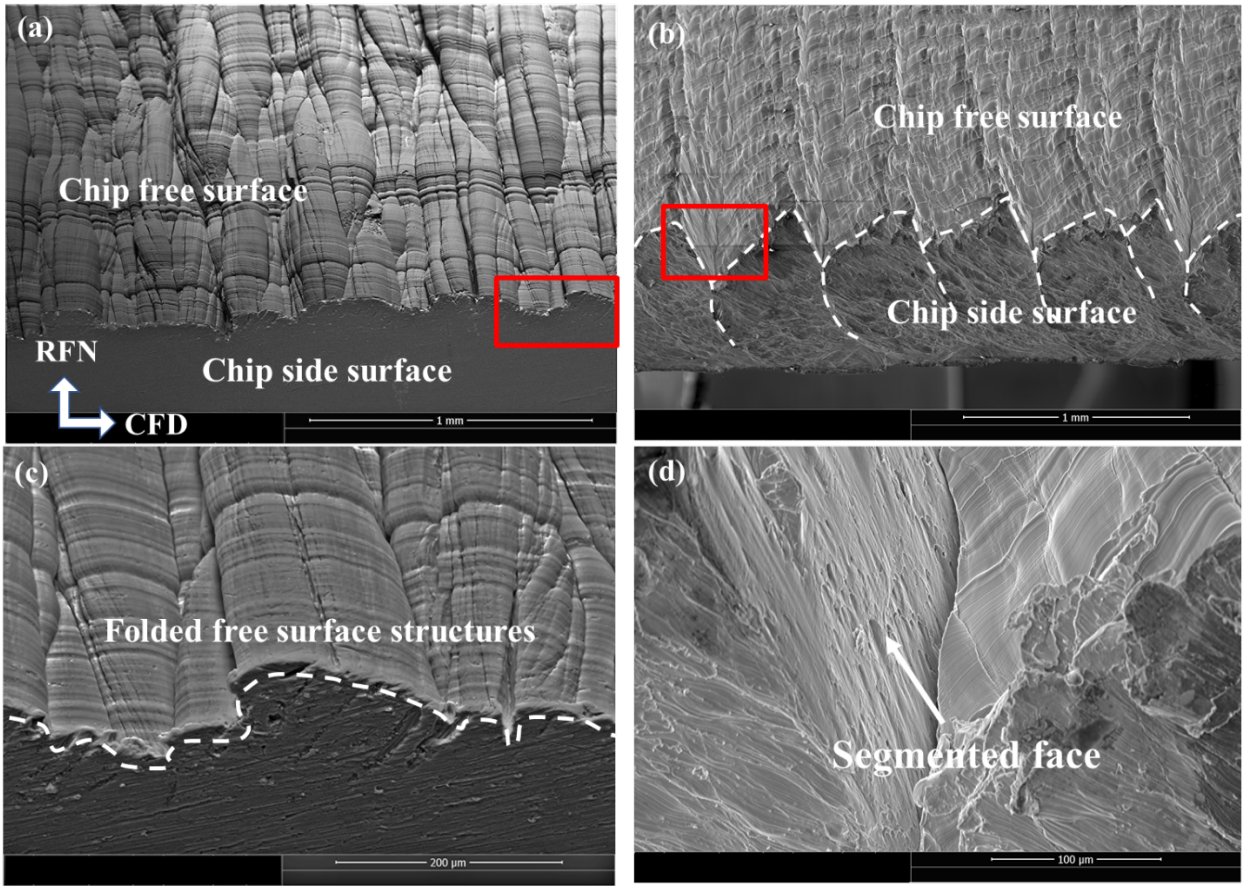

Fig. 4.1 SEM micrographs showing a) the chip surface morphology of soft and ductile AA 8040 that undergoes sinuous flow during cutting, b) the chip surface morphology of brass 260 that undergoes segmentation during cutting. The broken line traces reveal the saw-tooth surface morphology at the unpolished chip side surface. c) shows the magnified top edge view of the selection in a) with broken line traces of folded surface structures characteristic of sinuous flow, and d) also shows the magnified view of the segmented face in the selection in b).

When cutting ductile metals such as aluminum, copper, and single-phase brass, in the soft annealed condition, the chip that forms is usually very thick ($t_c \approx$ 5-15 t_o), with a characteristic morphology as shown in **Fig. 4.1a**. When viewed in the transverse direction, the surface appears to be constituted by a collection of mushroom-like features on its back surface [14,40,59,60]. This type (typical of the Type 1 chips in **Fig. 2.5**) of chip is also seen in cutting highly strain hardening materials such as niobium, tantalum and stainless steels, at low-to-medium speeds [36]. The chip

formation is characterized by unusually large cutting forces and large redundant strains, making them very difficult to cut. Ironically, these materials that are considered soft are rather difficult to cut.

A recent study by our group in Purdue University sought to better understand why commercially pure Cu in its soft annealed state is difficult to cut. By digitally processing high-speed images captured during the cutting process, it was discovered that the material flow is characterized by highly non-uniform (wiggly) flow; a mechanism described as sinuous flow [61]. The characteristic of this flow mode in the chip was mushroom-like structures seen on the back face of the chips caused by material folding (**Fig. 4.1a and b**) just like the type 1 chips in **Fig. 2.5**.

In this study, we further explore the fold formation in the cutting of soft and ductile commercially pure aluminum alloys. In addition to the mechanism of sinuous flow, stick-slip is explored as a secondary phenomenon that contributes to large fold formation in the chip. The contribution of stick-slip is investigated by examining the frictional conditions at the chip-tool interface vis a vis the chip surface morphology. Surface fold occurrence is treated in light of varying cutting conditions in a process map that allows for the selection of optimum cutting conditions to produce chips with limited folds.

Experimental

The model materials are the AA 8040 and Al 1100, in the as-cast and annealed conditions, respectively. The 8040 alloy was chosen simply because it was procured in the commercial as-cast condition as a wire bar; a condition that is representative of the softest state of the alloy. The similarities of the alloy with the Al 1100 in terms of composition (**Table 4.1**) and strength (hardness < 30), made it also a suitable candidate for comparison with the flow response of the 1100 under similar cutting conditions.

Table 4.1 Chemical composition of the alloys [48]

	Fe	Si	Cu	Mn	Zn	Zr	others	Al
AA8040	1.0		0.2	0.05	0.2	0.1-0.3	0.15	Rem
Al1100	1.0		0.05-0.2	0.05	0.1		0.15	99.0

Two cutting configurations (rotary and linear) were used in the experiments to study the distinct flow phenomena of sinuous flow and stick-slip. For studying stick-slip, experiments were done in the rotary configuration under dry cutting conditions. For these experiments, disk-shaped samples of diameter 60 mm were prepared for use as workpieces by machining using a band saw and a Fryer lathe (Model No: ET-18) for final trims. Using the wedge-shaped high-speed steel tools, continuous chips were produced at an undeformed chip thickness of 0.13 mm and at rake angles in the range of 5 to 45^{o}. At each rake angle, the deformation was carried out at cutting speeds in the range of 1, 3 and 6 m/s.

In the linear cutting mode, the experiments were channeled towards studying sinuous flow in the chips. A rectangular workpiece of dimensions 65 x 25 x 6 mm was used with a relatively low speed (3 mm/s), for rake angles between 20 and 40^{o}. Oil was also used as a lubricating medium to avoid any form sticking. This was necessary to isolate all stick-slip features and allow only the sinuous flow that produces the lamella (mushroom) structures to be observed. The use of the oil medium also enhances the imaging quality of the process. The image sequences were then processed, and the flow behavior characterized using PIV, an image correlation technique that quantifies the velocity fields of flow. The technique has been used widely in fluid and solid mechanics to quantitatively characterize flows [62,63]. In determining the velocity flow fields, pathlines and streaklines are generated and superimposed onto the images that tracks particle flow during the deformation. A pathline is the trajectory along which an individual particle (material point) travels whiles, a streakline tracks the particle flow path [64]. Streaklines are useful for flow visualization. The deformation parameters such as Von Mises effective strain, strain rate and strain rate tensors can be computed from PIV using a Matlab program.

Microstructure of workpiece and chip samples was characterized by optical metallography. Specimens were mounted in epoxy to avoid heating, ground with various grit sizes of SiC paper,

and final-polished with diamond and colloidal silica (0.06 μm). The specimens were etched by immersion in NaOH etchant (10 g in 100 mL H_2O) for 5 minutes. The microstructure was then observed under an optical microscope. High resolution SEM images of chip surfaces were acquired using Quanta 650 FEG. Macro images of the chips were examined using optical stereoscopy. Surface roughness and topography of the chips were examined using 3D optical profilometry (Zygo NewView 9000).

Chip Morphology

Long continuous chips of thicknesses 0.2 to 2.5 mm are produced from the workpiece. The chips exhibit varying degrees of surface folding on the free surface of the chips (**Fig. 4.2a**). The surface folding is shown to consist of two striking features; 1) a large-amplitude, low-frequency fold and 2) a low-amplitude, high-frequency mushroom-like structures that ride atop the large folds (**Fig. 4.2b**). The folds extend across the entire width of the chips (**Fig. 4.2c**). The high-frequency folds that are perceived as mushroom-like structures when observed in the CFD-RFN plane (**Fig. 4.2b**), appear to be long interweaving lamellae in the CFD-TD plane (**Fig. 4.2c and d**). These lamella structures cluster to form each large-amplitude fold (**Fig. 4.2c**).

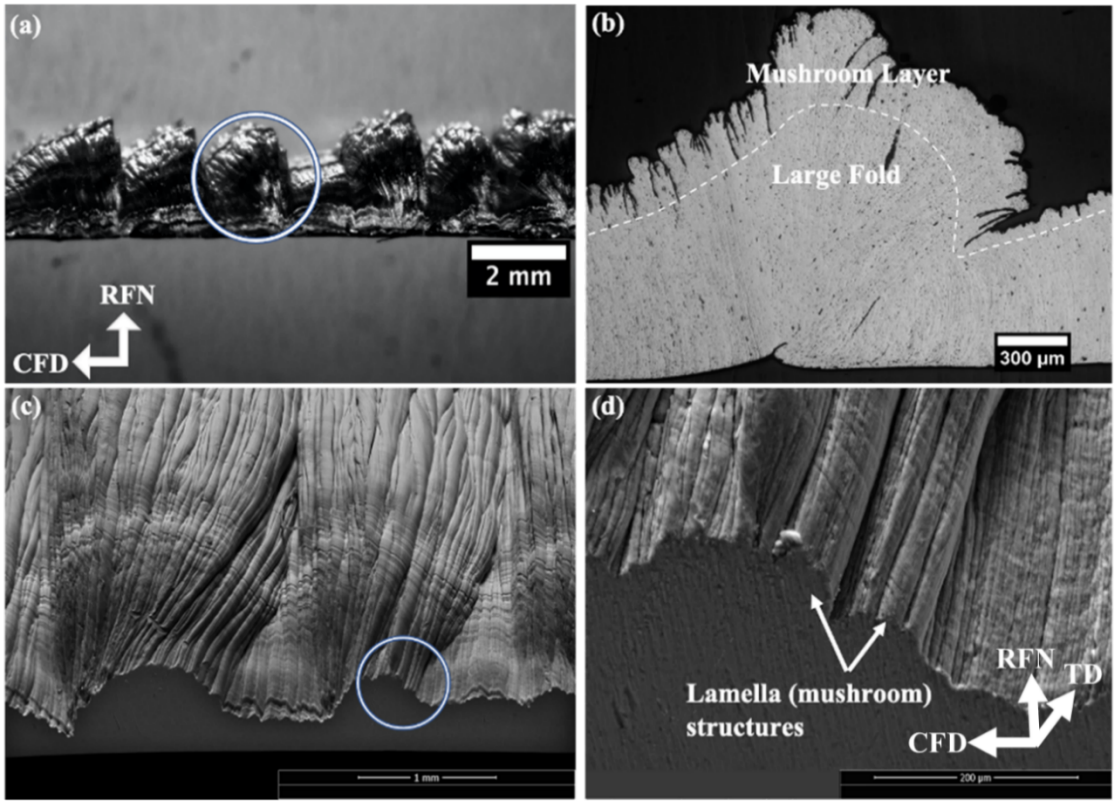

Fig. 4.2 Stereoscope image showing a chip with high amplitude surface folds at $\alpha = 5^{o}$ and V_o = 3 m/s, b) optical micrograph of the selection in a) showing mushroom structures atop the large amplitude bump, c) SEM image showing that the folds extend across the width of the chip, d) a higher magnification view of the edge in the selected area in c).

Fold Size Measurement

3D surface profilometry was employed to quantify the sizes of folds. In doing so, two independent parameters are considered, the height (amplitude) information and the wavelength (peak-to-peak spacing) information of the folds. On the wavelength information, Power Spectral Density (PSD) analysis was performed on the generated 3D surfaces (**Fig. 4.3a**) to decompose the original surface profile into the various spatial frequencies corresponding to the folds. Shown in **Fig. 4.3b and c** are high-density peaks with spatial frequencies corresponding to the average spacing of the large folds (2 mm) (**Fig. 4.3b**) and of the lamella structures (0.15 mm) (**Fig. 4.3c**).

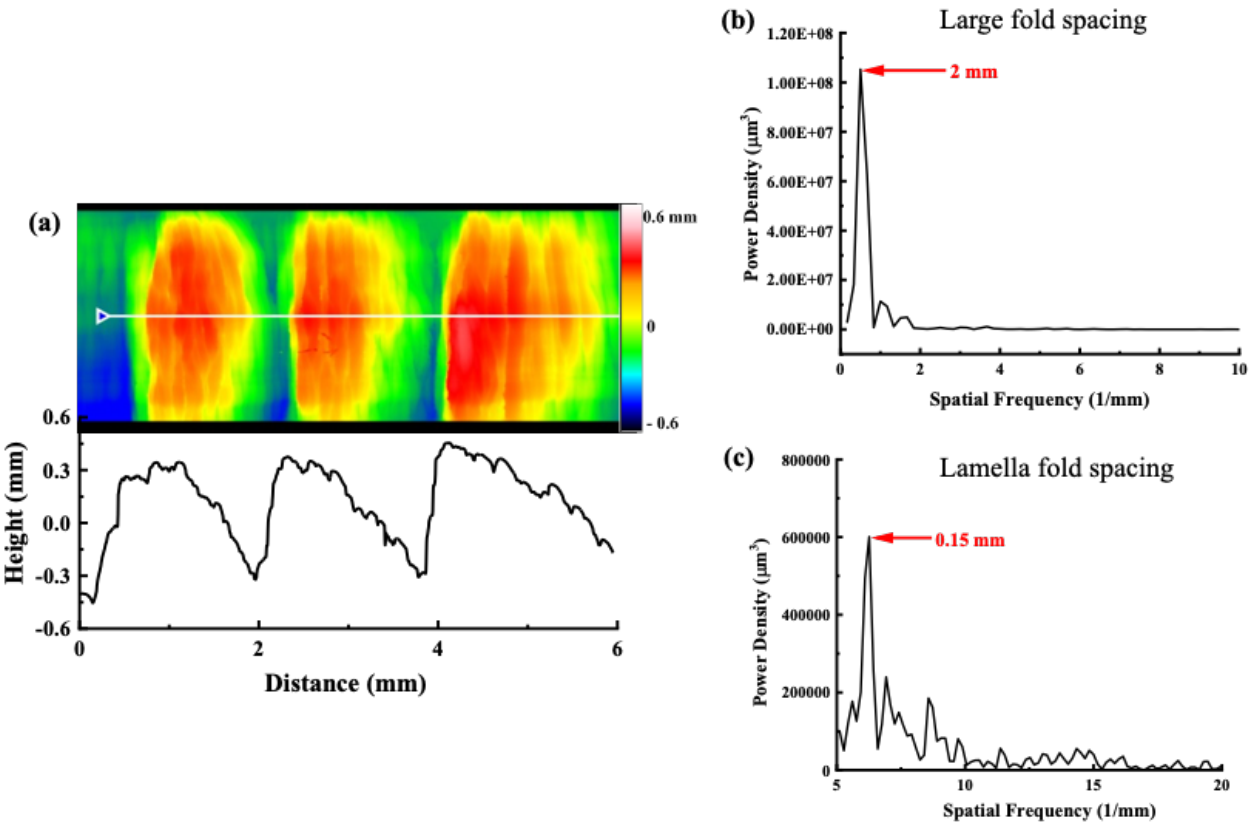

Fig. 4.3 a) 3D profile data, showing the topography of the chips at $\alpha = 5^{o}$ and $V_o = 6$ m/s. b) and c) are PSD plots showing b) peaks for spatial frequencies corresponding the large fold spacing of 2 mm and c) a mushroom spacing of 0.15 mm.

In determining the height information, the maximum peak-to-valley heights (Rmax) of the folds were determined on Fast Fourier Transform (FFT) filtered surfaces of the original surface profiles. The filtering was done by applying a cutoff wavelength equal to the spacing determined in the PSD analysis (cutoff wavelength, $\lambda_c = 0.15$ mm). **Fig. 4.4a** shows the filtered surface containing all of the high-frequency lamella features, leaving the residual surface (**Fig. 4.4b**) free of the lamella structures. The maximum peak-to-valley height (Rmax) of the filtered surface and the residual surface are 0.09 and 0.57 mm respectively; over a factor of 6 amplitude difference between the two distinct surface folds. The Rmax values shows the depth to which these folds propagate into the thickness of the chip. To put this into perspective, for a chip with a measured thickness of 2 mm, only 4.5 % of the thickness will constitute the lamellae and about 28.5% for the larger folds.

This suggests that the large folds are far less desirable for many applications such as those requiring high chip packing (stacking) density.

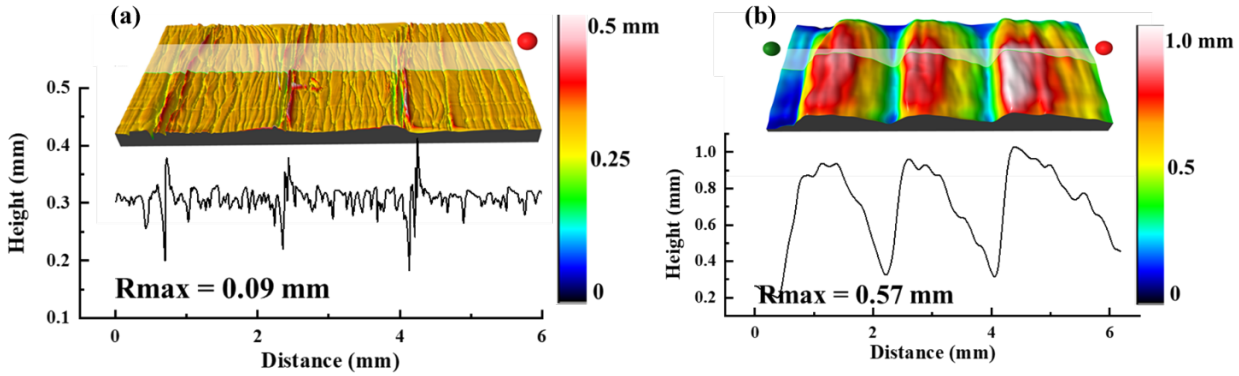

Fig. 4.4 FFT filtered surface showing the profiles and Rmax values of a) the lamella features, and b) the large surface folds.

4.2 Mechanisms of Fold Formation

It is useful to examine the nature of material flow and the intimate interaction between the material and the cutting tool during the chip formation to understand the origins of the surface folds. Therefore, two phenomena that are believed work in tandem to orchestrate the formation of the folds are discussed; sinuous flow phenomenon, which relates to the formation of the high frequency lamella structures, and stick-slip phenomenon, which is associated with the low frequency, large amplitude folds.

Sinuous Flow Phenomenon

The material flow behavior in machining is characteristic to the alloy and its initial deformation state [14]. In the cutting of soft and ductile alloys, such as the aluminum alloys under study, the plastic flow behavior is highly non-uniform, characterized by extensive redundant deformation and vortex-like flow components, a characteristic often referred to as ‘gummy’. This phenomenon also described as sinuous flow [61], is a non-uniform/unsteady mode of plastic flow responsible for the poor machinability of these alloys.

Through *in situ* imaging and particle image velocimetry (PIV), analysis of the material flow behavior is demonstrated in a relatively slow cutting condition (cutting speeds of 3 mm/s for α =20^{o}) using annealed Al 1100. This was also done under non-dry conditions with oil as the lubricating medium. These conditions are necessary for isolating conditions that promote sticking and allow for the easy observation of the low-amplitude lamella structures. The flow of the metal during the deformation was imaged *in situ* by high-speed camera (Photron FASTCAM Mini) coupled to an optical microscope. Images were collected at a frame rate of 500 fps. The image sequences were analyzed using PIV.

By superimposing streaklines on the chip, the material flow in the chip is shown to be wiggly (sinuous) consistent with the large inhomogeneous strain (**Fig. 4.5a and b**). The deformation zone is usually considered to be narrow and sometimes idealized as a plane, but in actuality, the region of influence of the deformation can extend far (50 -100 μm) ahead of the shear plane, especially in highly strain-hardening materials. It is in this region that the onset of the wiggly flow (initial bump in **Fig. 4.5a**) is initiated. The initial bump goes on to become a fold after exiting the primary shear zone (**Fig. 4.5b**). The process is repeated with a follow-on bump formation (**Fig. 4.5b**) ahead of the shear plane which will go on to become a fold as the deformation continues. These folds are what we observe as mushroom (lamella) structures on the free surface of the chip in *ex situ* observations. Prior studies in thermally etched Cu, where the grains of the workpiece are visible, it is observed that, when sinuous flow is initiated, the surface grains ahead of the shear plane are pinned down at the grain boundaries to form the initial bump [61]. As the deformation progresses, the compressive stresses exerted on the material in the primary deformation zone, causes the grains to plastically fold (buckle), thus forming the mushroom-like (lamella) structures on the free surface of the chip.

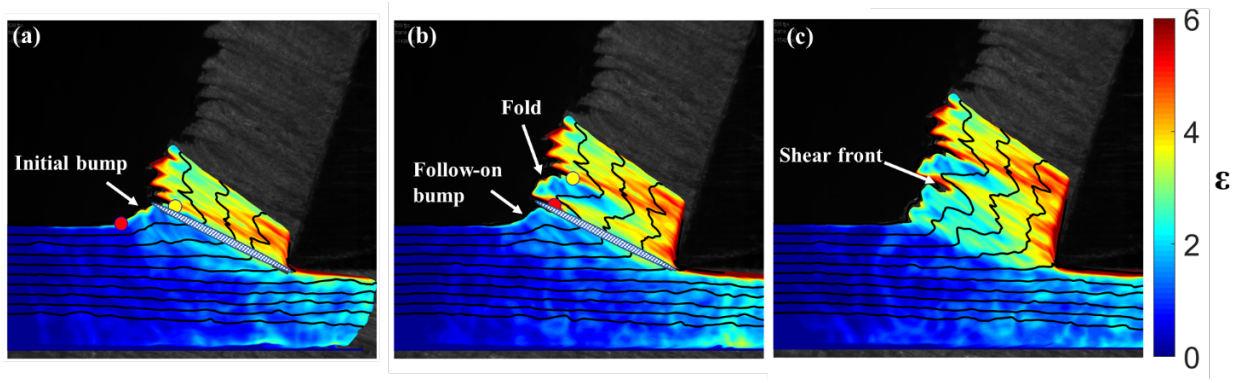

Fig. 4.5 Micrographs showing a) wiggly flow of streaklines in cutting Al 1100, b) inhomogeneous strain in the chip.

Another characteristic feature of the sinuous flow phenomenon is the large inhomogeneous strains (effective strains measuring up to 6 in **Fig. 4.5**). The distribution of the strain in the chip shows a particularly high strain concentrations in the narrow regions between lamellae (the shear front in **Fig. 4.5c and Fig. 4.6a**). These shear fronts represent the boundaries between two lamella structures. Also noticeable are intra-lamella strains (**Fig. 4.6b**) occurring as bands of medium-to-high shear possibly due to the plastic buckling effect of the grains as a secondary response to the concentrated shear in the primary deformation zone. The lamellae are also highly interwoven suggesting that the shear fronts separating each lamella structure do not run along the entire width of the chip. They also do not propagate to greater depths in the chip; consistent with the Rmax values of the lamellae (0.09 mm) in **Fig. 4.4a**.

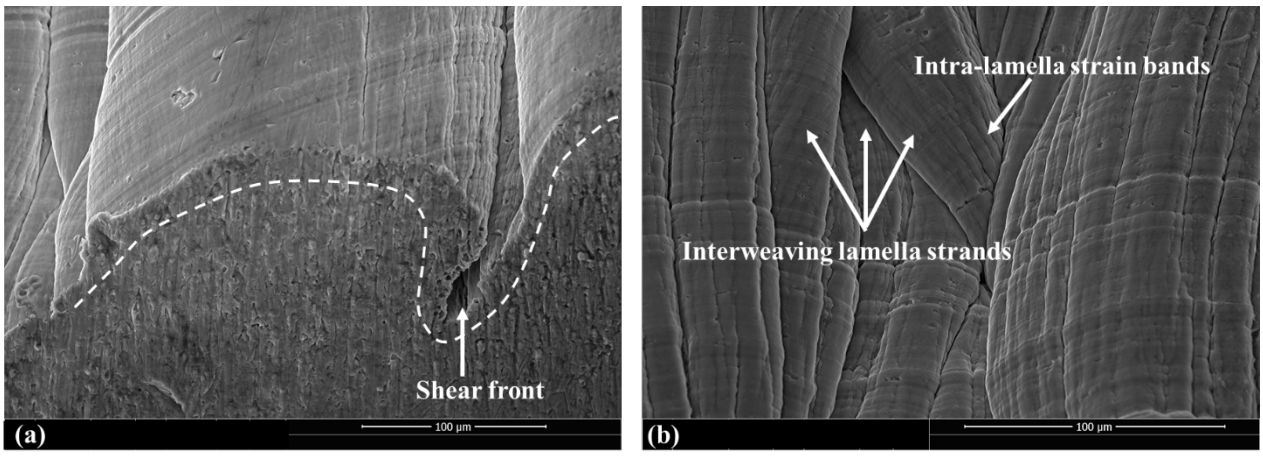

Fig. 4.6 SEM images showing a) lamella formation by grain folding at the edge of a FM chip, b) interweaving strands of lamella resulting due to sinuous flow.

Due to the wiggly flow nature of the deformation and the extensive thickening of the chip (t_c/t_o > 5), the cutting forces are very high. **Fig. 4.7** compares the specific cutting forces of the 8040 alloy which undergoes sinuous flow with brass 260 that undergoes segmentation. The chips from both materials were of the same width (6 mm) and cut under the same deformation conditions (t_o = 125 µm, V_o = 4 m/s). The specific cutting forces of the 8040 due to sinuous flow is > 50% higher than what is seen in the case of segmentation in brass 260 even though the flow stress of the brass is much higher than the Al.

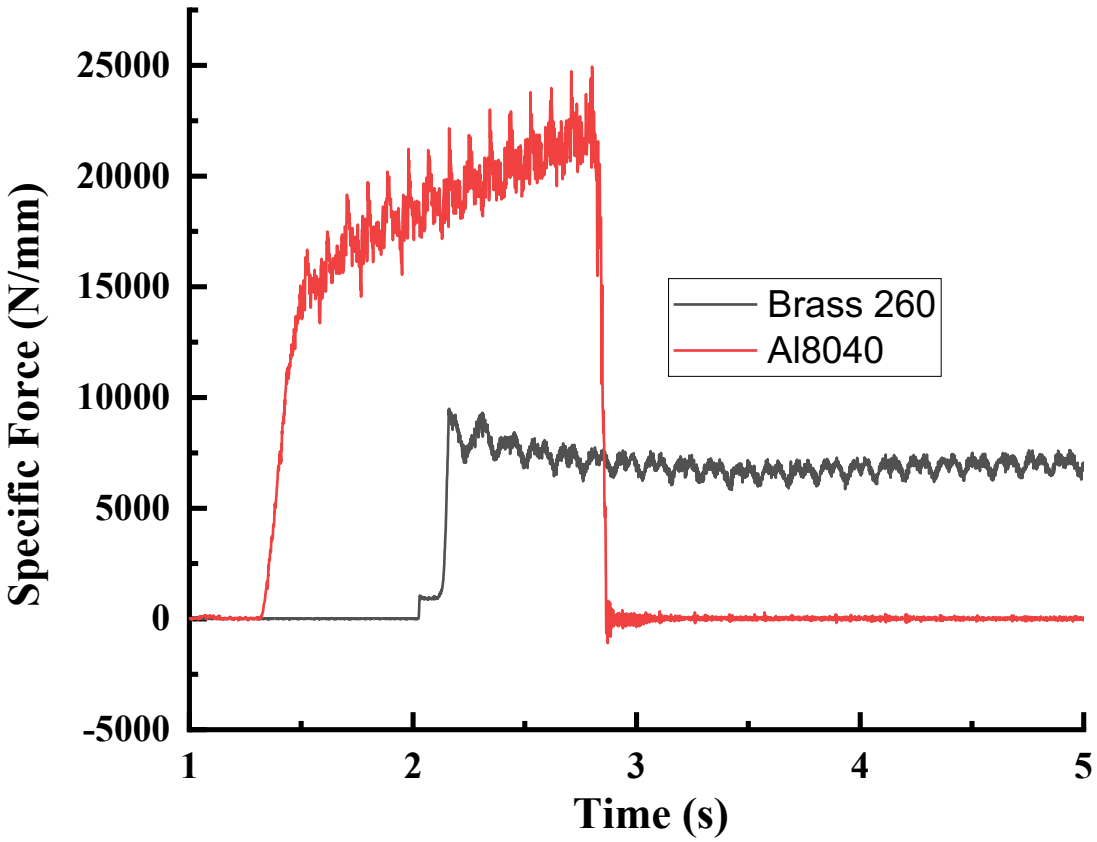

Fig. 4.7 A plot of the specific cutting forces for brass 260 and Al 8040. The latter undergoes sinuous flow while the former undergoes segmentation. Both materials were processed under same deformation condition.

Stick-Slip Phenomenon

When a layer of material is removed in the form of a chip from a bulk workpiece by machining, two new surfaces are produced; the top free surface and the underside surface that is in contact

with the tool rake face. The interaction between the tool and chip has mainly been characterized by considering the contact length, the stress distributions and the conditions of friction at the interface [35,65–73]. In analyzing the contact and frictional conditions at the interface, two contact regions are identified; a region of chip-tool sticking near the tool edge and a sliding region farther away from the tool edge **(Fig. 4.8a)** [35,72,73]. The sum of the lengths of these regions constitutes the chip-tool contact length, L_{ct}. This parameter is critical for controlling the cutting forces, cutting temperatures, tool wear and tool life [72], and as a result, it has great influence on the finished surface quality of the chips.

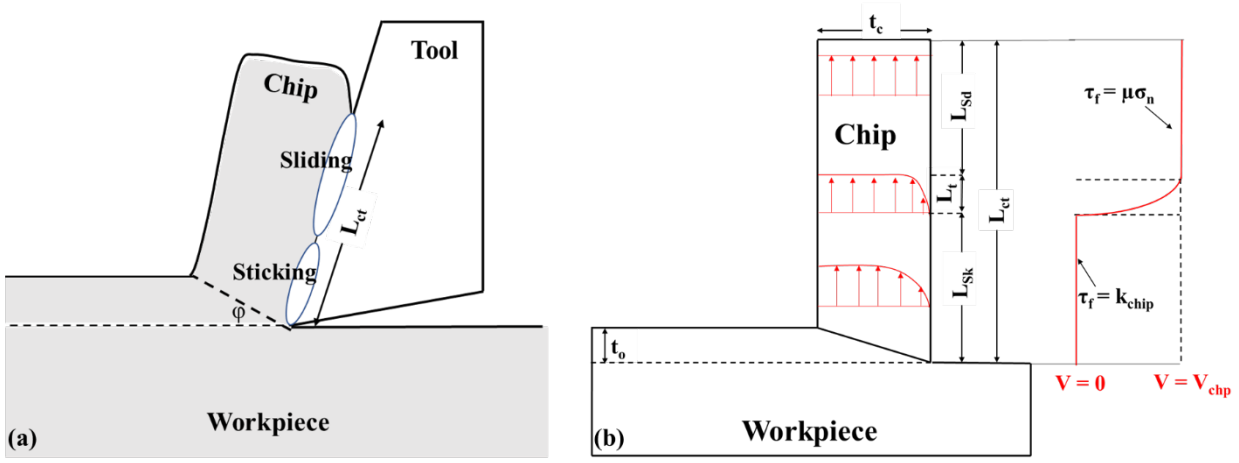

Fig. 4.8 Linear cutting schematics showing a) the contact regions at the chip-tool interface (Modified after [70] and b) the chip velocity profile during the deformation (After [74])

The conditions for sticking are favored when the actual chip-tool contact area approaches the geometric interface area under high compressive forces acting normal (σ_n) to the chip-tool interface. This allows the clean surfaces of the chip to atomically bond to the rake face of the tool, thus, promoting a seizure in relative motion between the chip and the tool at the interface. Away from interface however, the chip flows only in adjacent layers until the shear velocity (V) reaches the bulk velocity of the chip (V_{chp}) to transition the flow from the sticking phase to the sliding phase (see chip velocity profile in **Fig. 4.8b**). The distribution of the material velocity in the chip along the contact length is obtained from the material conservation principle ($V_o t_o = V_c t_c$). A condition of zero chip velocity (V_c) at the sticking interface promotes the extensive thickening of

the chip via material pileup to form large bumps. These bumps are what we refer to as large amplitude folds (see **Figs. 4.3**).

In the sliding phase, coulombs frictional law ($\tau_f = \mu\sigma_n$) applies where sliding friction becomes the dominant resistive force to chip flow. The onset of sliding is however, preceded by a secondary shear either at the interface or within the chip itself, depending on the strength of the bond (degree of sticking). The strength of the bond depends to a large extent, on the type of tool, the work material, and the deformation conditions. There are a number of possible ways that the chip may break away from the tool: 1) At low-to-medium interface bond strength, the bond can be broken at the interface allowing the chip to transition into the sliding mode without significant damage to the tool and the chip rake face. 2) The chip may adhere to the tool so strongly that it can separate either with a damage to chip or a damage to the tool. In cases where cemented carbide tools are used, the strength of the adhesion may cause the tool itself to fracture near the tool edge leaving the fragmented edge attached to the underside (rake face) of the chip. The other scenario depicted in **Fig. 4.9a** results in damage to the chip. When two materials of different strengths are atomically bonded as described in the sticking phase, the force required to slide one over the other becomes the force needed to shear the weaker material across the region of contact. Since the chip is the weaker material at the interface in the case of the soft ductile alloys, then the shear will occur within the chip at the onset of sliding (chip breakaway). This usually leaves remnants of the chip material on the tool face which are manifested as tear surfaces (grooves) on the rake face of the chip as shown in **Fig. 4.9a**. This is what is observed in the chips with large amplitude folds over the regions of sticking – the sticking grooves (**Fig. 4.9b**). The grooves manifest the extent of tear within the chip which suggests that the stress required to break the bonds at the interface is higher than the shear strength of the material. Analysis of the tear surfaces (sticking grooves) reveals dimpled fractured surfaces; an indication that the chips break away by ductile fracture (**Fig. 4.9c**). It is notable that, directly above (free surface) each sticking groove is a highly thickened material (large fold), a consequence of the seizure of material motion during the sticking phase. The average groove length (L_g) gives a close estimate of the sticking length.

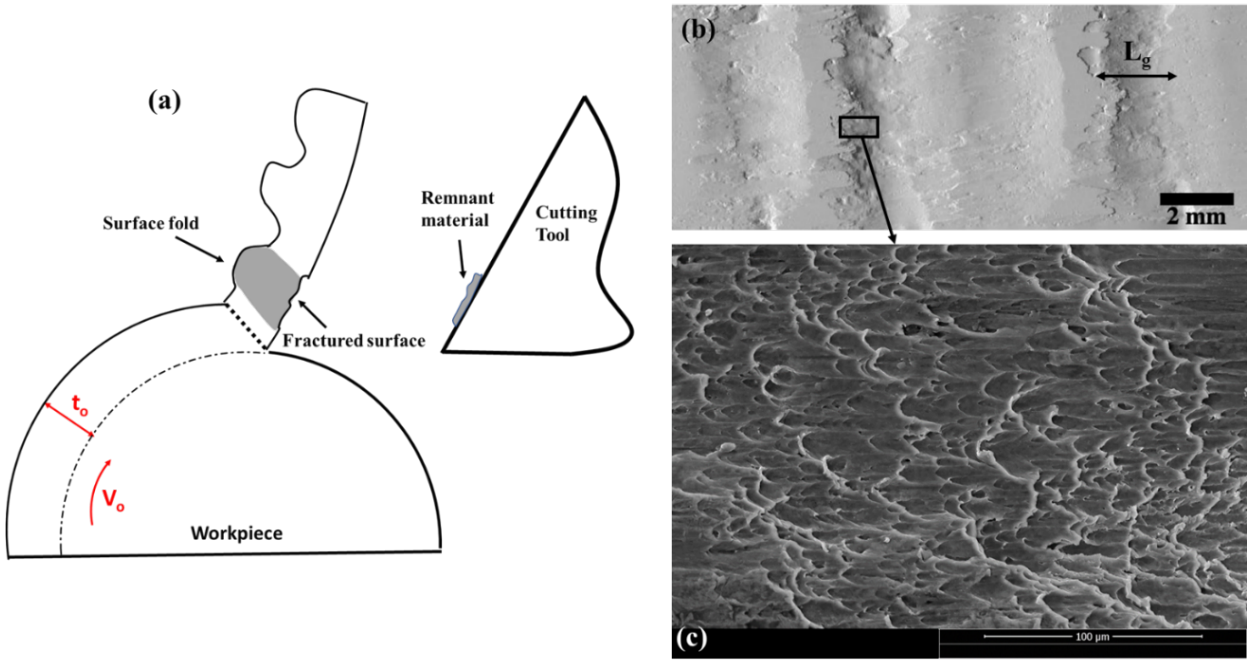

Fig. 4.9 a) Schematic showing sticking grooves after chip break away during sliding. Remnants of the chip material are often left on the tool face if the tear occurs within the chip. b) a micrograph showing sticking grooves on the rake face of an 8040 chip, suggestive of tear within chip and c) SEM image of the sticking groove showing a ductile fracture mode during the break away.

Chip Flow in Sticking and Sliding Conditions

It is useful to examine the chip flow to understand the origins of the large amplitude folds. Primary deformation along the shear plane is often reflected in the chip as shear flow lines inclined at angles determined by the rake and shear angles [35]. Observations of these flow lines at regions of the large-amplitude folds reveal 3 primary phases of deformation resulting from stick-slip as shown in **Fig. 4.10**. These phases arranged in the direction of chip flow include: 1) the sticking phase, 2) the transition (break-away) phase and 3) the sliding phase (**Fig. 4.10a**).

To understand the flow in this region however, we have to work backwards from region 3 (the sliding phase) in **Fig. 4.10**. When a chip leaves the PDZ and undergoes sliding along the rake face of the tool, the flow lines near the rake face are further dragged along the direction opposite to the direction of chip flow in what is described as secondary shear (see region (3) in **Fig. 4.10a** and **c**). The zone of secondary shear depends on the extent of the deformation and material conditions but

is typically a narrow region (~5 – 10 μm) from the rake face. As has been previously established, in the sticking region (region (1) of **Fig. 4.10a**), there is a seizure is the relative motion between the chip and the tool at the interface. This lack of motion prevents the occurrence of the drag of the primary flow lines since there is no secondary shear occurring at this location. As a result, region (1) – the region of dominant sticking (**Fig. 4.10a**), leaves straight flow lines inclined an angle governed by the primary shear. **Fig. 4.10c** shows a higher magnification view near the rake face in the sticking region where there is no indication of secondary flow line drag. As the chip formation continues, the material flows in adjacent layers away from sticking interface. This type of motion rotates the primary flow lines in (1) towards the direction of chip flow (see reoriented flow lines in region (2) of **Fig. 4.10a**). With the chip still stuck to the tool, this flow mode tends to accommodate the extra material coming in from the PDZ by piling up the excess material into a large bump – the fold. When the force required to effect sliding reaches the shear flow stress (k_{chip}) of the material, the chip breaks away by a tear within the chip leaving a groove on the rake face. Once the chip breaks away, it then slides along the face of the tool, creating a drag of the primary flow lines near the rake face to form the secondary deformation zone (SDZ) (sliding region (3)) (**Fig. 4.10c**). The cycle of sticking and sliding continues for the length of the cut as long as cutting remains feasible. The stick-slip phenomenon dos not just promote the formation of the large amplitude folds on the chip free surface under dry cutting conditions of the soft aluminum alloys, it can also be detrimental to the rake face surface quality of the chip if the break away tears occur within the chip.

It is interesting to note that, the sinuous flow structures (lamellae or mushrooms), can be classified as the primary surface folds because they are initiated ahead of the shear plane. The large-amplitude folds are basically secondary folds resulting from the transformation of the primary shear structure under conditions of stick-slip. Therefore, when these two phenomena combine in the cutting of soft and ductile aluminum, the three key features that are likely to define the chip surface quality are the small-amplitude, high-frequency lamella (mushroom) structures, the large-amplitude, low-frequency surface folds and possibly the sticking grooves on the rake face if tears are within the material.

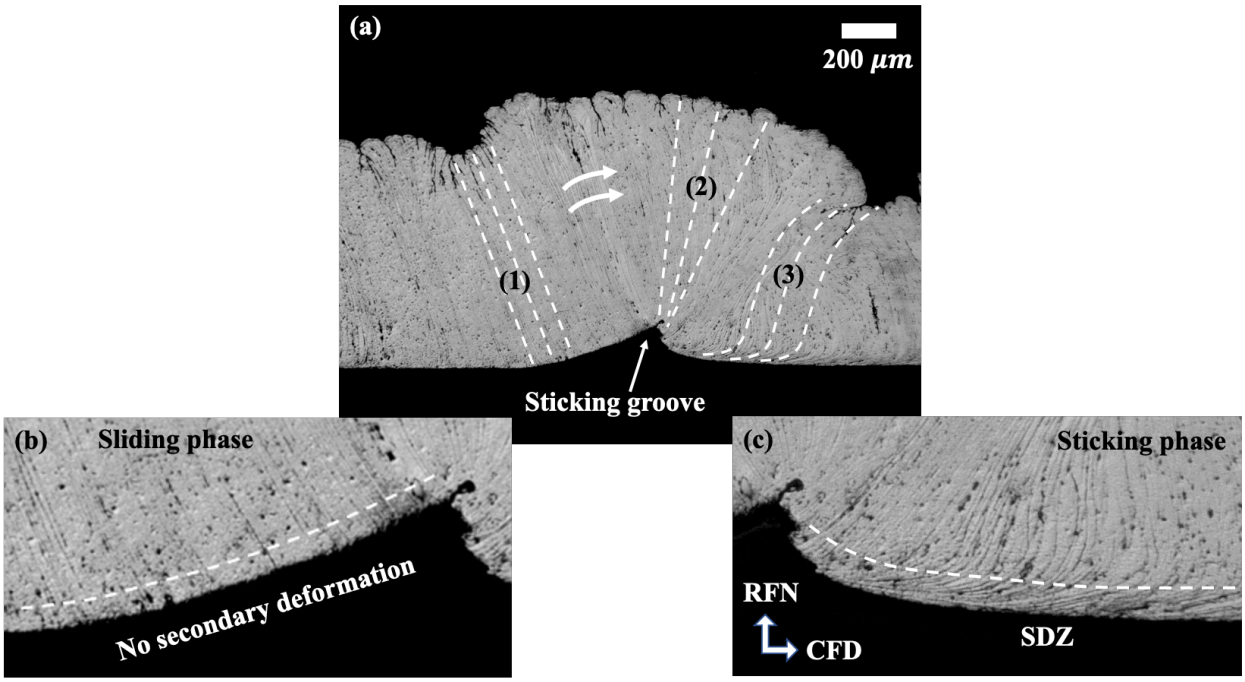

Fig. 4.10 Micrographs showing a) flow line pattern in a large amplitude fold, b) higher magnification view of the secondary deformation zone under sliding conditions and c) high magnification of the rake face under sticking conditions.

4.3 Suppressing Flow Instabilities

The mechanisms of fold development suggest the difficulty in cutting the very soft and ductile metals in the annealed state. This difficulty can be resolved if these mechanisms are suppressed or eliminated altogether. A number of approaches have been tried including pre-straining the workpiece before the deformation. Pre-straining a thin layer of the annealed material causes grain refinement and reduction in ductility of the surface layer. Doing so reduces the bulge formation on the free face as well as the tendency to sticking on the rake face. Evidence of this is demonstrated by Udupa et al. [75] in transforming the sinuous flow in annealed Cu to laminar flow in the H14 (half-hard) condition, with a drastic reduction in cutting forces. Much more homogeneous strains are also achieved due to the reduction in redundant deformation in the H14 condition. A more recent and intriguing approach to suppressing the fold formation is the use of surface-active agents that adsorb onto the workpiece surface [40,61,76]. The surface-active agents are found to cause local ductile-to-brittle transition in the deformation zone, causing the flow to switch from sinuous

to a somewhat laminar flow. Yeung et al. [61] shows the effectiveness of the surfactants in transforming the flow from sinuous to laminar by painting the surface of the workpiece with a layer of ink. This transformation also leads to a drastic reduction in cutting forces. Media that have been found to be effective include metal-marking inks, glues and sharpie [36,75]. In relation to sticking at the chip-tool interface, the use of lubricants is well documented to be a potent mechanism for lowering friction at the interface to enhance sliding [15,35].

In this work, two different approaches both involving deformation geometry design are used for suppressing the flow instabilities are explored. The first involves altering the cutting conditions and the second modifies the deformation zone geometry by the use of a constraint in what is referred to as Hybrid Cutting Extrusion (HCE).

Sinuous Flow Suppression via Cutting Conditions.

The sinuous flow structures are the small-amplitude, high-frequency lamella (mushroom) structures that define the chip surface even if there are no large-amplitude folds. These structures as indicated earlier are originated ahead of the shear plane by the development of a plastic buckle that then transform into a fold (bump) after exiting the primary shear zone. Suppressing the fold formation therefore requires a control of the initial plastic buckle ahead of the shear plane. This was done by changing the deformation geometry through the rake angle in the linear cutting configuration. The rake angle was increased from 20 to 40^{o} at a constant cutting speed of 3 mm/s.

By increasing the rake angle, the initial buckle formation (see the case of $\alpha = 20^{o}$ in **Fig 4.11**) which develops into the fold is not originated in the case of $\alpha = 40^{o}$ and therefore does not evolve into a fold. The angling of the tool to more positive orientation allows the tool to easily plunge into the workpiece without straining a larger region around the plane. Thus, suppressing how much buckling is achieved ahead of the shear plane. The lack thereof of the initial bulge allows for the somewhat smooth flow of the material as shown clearly by the streaklines. This transformed, non-wavy flow is what we referred to as laminar flow.

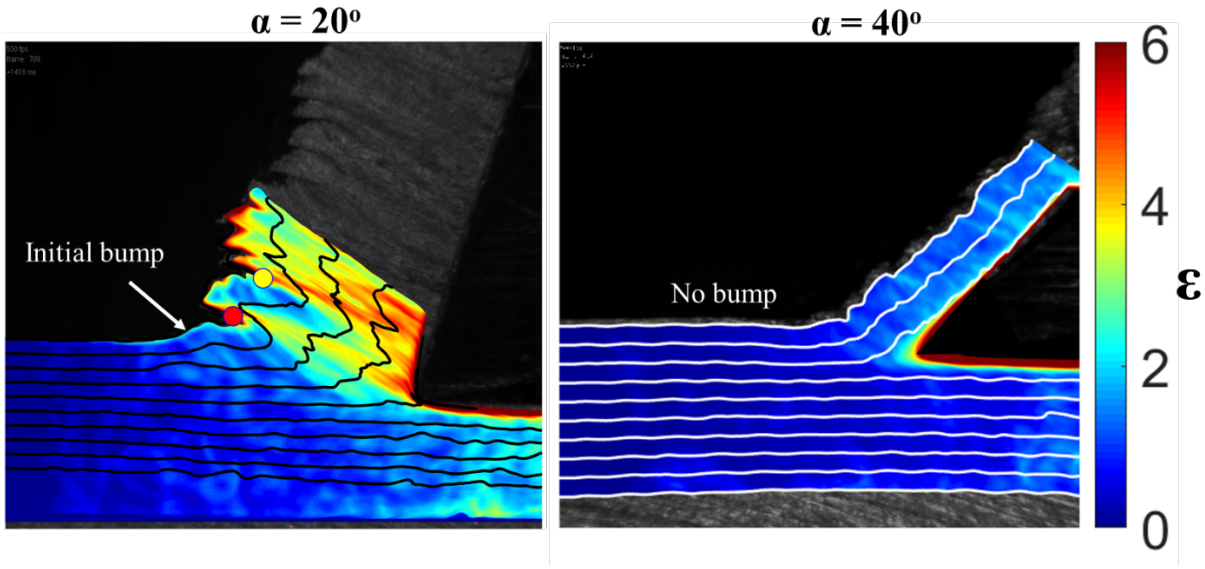

Fig. 4.11 Suppressing sinuous flow by increasing rake angle from 20° (highly sinuous) to 40° (laminar flow).

There are other key features of the transformation of the sinuous flow to laminar flow. As a characteristic of sinuous flow, the chips always tend to be very thick ($t_c > 5\ t_o$ for this case). This extensive thickening is controlled under laminar conditions. In fact, at $\alpha = 40^o$, $t_c \approx t_o$ in **Fig. 4.11**. Another important feature is the strain levels both in the chip and in the workpiece. Under the sinuous conditions, the strains are quite large reaching up to 6 in certain packets of the chip due to large amounts of redundant strains associated with the flow type. The workpiece also undergoes significant straining reaching to levels of 2. Such large strains are not seen under laminar flow conditions with only the maximum strain occurring right at the tip of the tool. Due to the large reduction in the strain and chip thickness, the cutting forces for the laminar case are also quite low compared to the case of $\alpha = 20^o$ where sinuous flow dominates the chip flow behavior (**Fig. 4.12**).

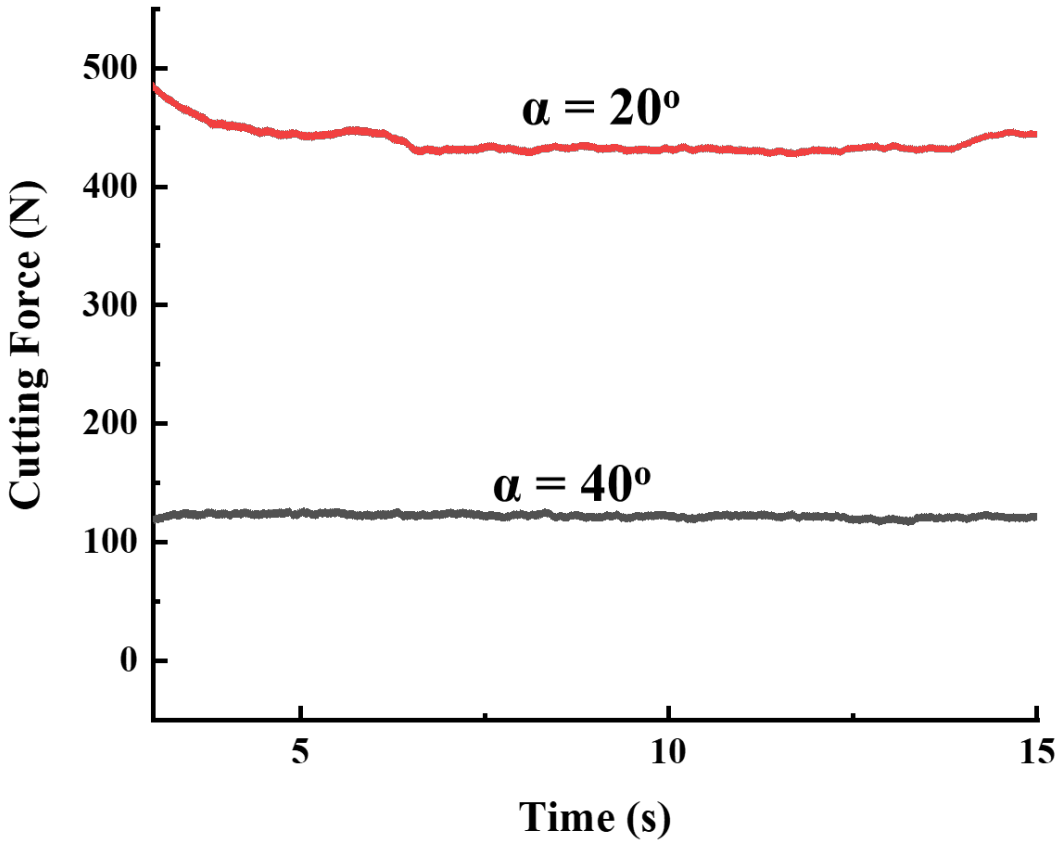

Fig. 4.12 Plots showing the cutting forces for the conditions of sinuous flow (α = 20°) and for laminar flow (α = 40°)

In quantifying the size of the features under the two striking flow conditions, 3D surface profilometry was performed on the chip surfaces. The surface profiles were collected along a slice running through the chip surface along the length of the chip. This orientation allows for the profiling of the surface features since it is perpendicular to the lay of the features. The peak-to-valley (Rmax) height of the surface is quantified along the slice. The Rmax parameter is an amplitude parameter that helps to determine how deep the folds penetrate into the thickness of the chip. **Fig. 4.13** shows the 3D reconstructed surfaces and the line plots of the line profiles. The surface features under the sinuous flow condition (α = 20°) rises to larger amplitudes with an Rmax value of 29.8 μm. This amplitude value is > 60% than the case of the laminar flow case (α = 40°). the reduced feature amplitudes under the laminar condition offers a significant benefit in using the chip as a final product for some applications or may be used as a half-product for light secondary

processing by cold rolling/drawing to improve the surface finish. There is, however, some concern that must be noted on the over reliance of the cutting conditions for transforming the flow. With increased rake angle, the plastic strains imposed on the chip and thus chip strength is compromised. The tool edge strength is also reduced at high rake angle and may accelerate wear and fracture especially if cutting speed is increased alongside the rake angle. The strongest tool edge is often achieved with negative rake angles and hence are used for cutting harder grade materials [15].

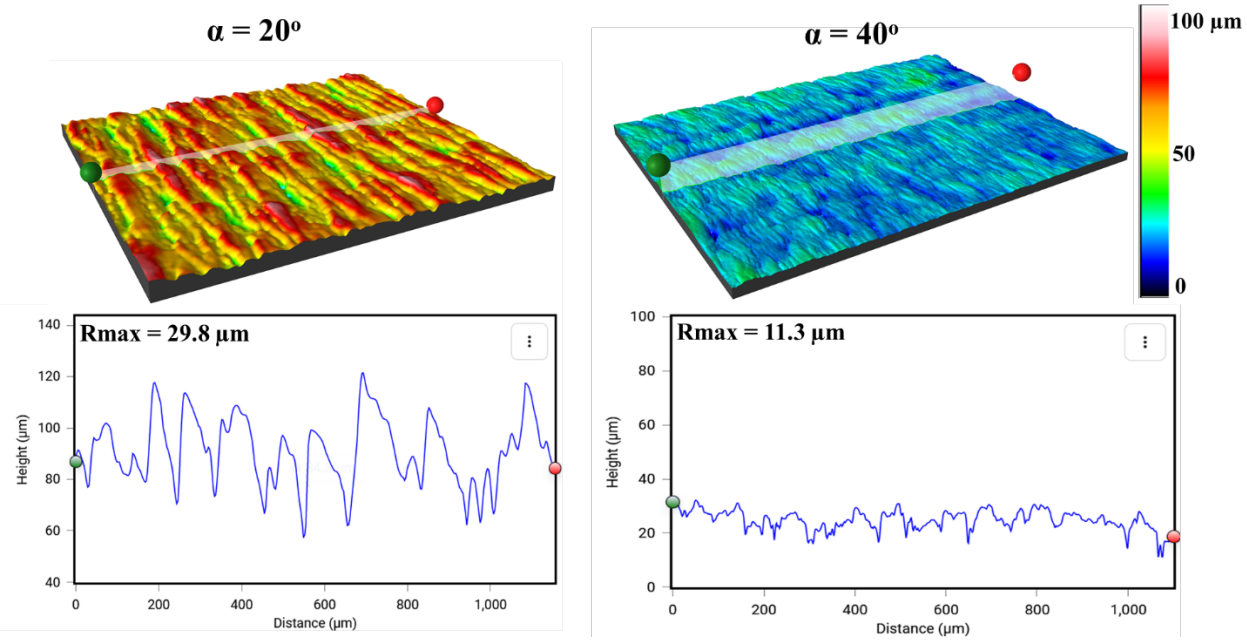

Fig. 4.13 Surface morphology of chips produced at a) $\alpha = 20^{o}$, and b) $\alpha = 40^{o}$ for a cutting speed of 3 mm/s. The surface profiles are plotted along a slice in the longitudinal direction to reveal the morphology of the folds. The peak-to-valley heights (Rmax) of the folds are shown to decrease from 29.8 µm to 11.3 µm as α is increased from 20 to 40°. This change is Rmax value is due to the flow transition from sinuous to laminar.

Suppressing Stick-Slip via Cutting Conditions

In order to study the effect of cutting conditions on the large-amplitude fold formation, the cutting speed and rake angle were varied under dry cutting conditions in the rotary configuration. This configuration was used in a high-power CNC Fryer lathe with spindle speeds ranging between 50-2500 rpm. The use of this lathe was meant to meet the high-power demands of the deformation under sticking conditions. A constant t_o = 0.13 mm was used for the rake angles ranging between

5-45° and cutting speeds of 1, 3 and 6 m/s. The t_o value was determined from preliminary experiments, to be suitable for the different chip shapes and sizes that will be produced under the varying cutting conditions and for ease of characterization.

Shown in **Fig. 4.14** is the effect of cutting speed on the surface morphology (rake face and free surface) of the chips at a rake angle of 20°. The large-amplitude folds are shown to be prevalent at low cutting speeds (V_o = 1 m/s) due to the intensity of sticking as registered by the fractured sticking grooves on the rake face. At higher cutting speed (V_o = 6 m/s), the dominant folds are the low-amplitude lamella structures with no registry of sticking grooves on the rake face except for the tool marks that run parallel to direction of chip flow. Similar trends in the morphology are observed at rake angles of 5, 30 and 35° for the speeds of 1, 3 and 6 m/s. On the rake angle effect, the surface folds also decrease with increasing rake angle for any given cutting speed.

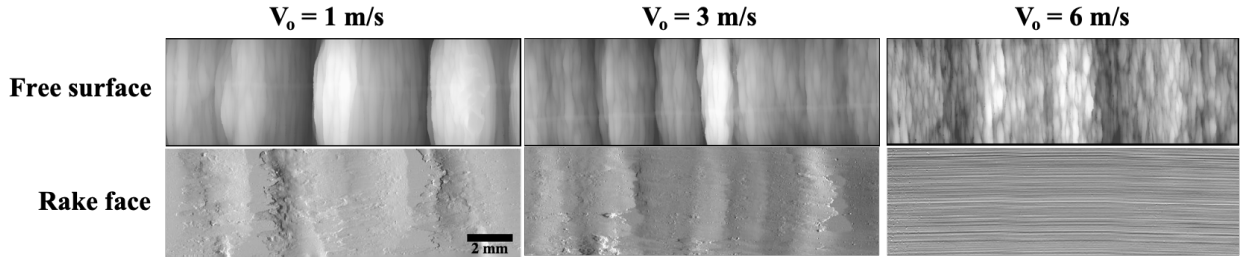

Fig. 4.14 Micrographs showing the change in surface morphology of the chips for different cutting speed at a rake angle of 20°. Intense sticking conditions at V=1 m/s are observed tending to the occurrence of large-amplitude fold. At 6 m/s, less intense sticking conditions results in the prevalence of low-amplitude lamella folds.

The observed trends in the surface morphology can be understood by analyzing the chip-tool contact and frictional conditions. As indicated previously, the formation of the folds is linked to chip-tool sticking and thus depends on L_{ct} and the resulting frictional conditions. Although *in situ* measurements of the contact length is difficult at higher cutting speeds, the most common technique for measuring the contact length is microscopic examination of the wear traces left by the chips on the tool rake face [71]. Many of such measurements reported in the literature show a decrease in contact length when cutting speeds are increased [71,77–79]. In this study, L_{ct} is evidenced by the area of the sticking grooves left on the chip rake face. At low cutting speed (V_o = 1 m/s), the sticking conditions appear to be extreme as manifested in the large groove areas (**Fig.**

4.14). As the speed increases, the chip-tool contact area reduces and thus, reduces friction at the interface. **Table 4.2** shows the friction forces (F) calculated from the dynamometer reading of the cutting force (F_c) and thrust forces (F_t) following Merchants model of the friction at the interface [33] (**eq. 4.1**). Evidently, the frictional forces decrease with increasing cutting speed which is consistent with the decrease in the contact areas as shown on the rake faces of **Fig. 4.14**.

$$F = F_c \sin\alpha + F_t \cos\alpha \tag{4.1}$$

The change in the tool geometry, specifically the rake angle, also influences the contact conditions and friction at the interface. Increasing the rake angle allows for the tool to plunge easily into the work material, lowering the contact length and friction at the interface (**Table 4.2**). By reducing the chip contact length and friction through changes to the geometry, the intensity of sticking (chip-tool bond strength) is reduced, which suppresses how much pileup is obtained at the sticking zones. It worth also to note that, the lack of sticking grooves on the chip rake face is not an indication that sticking does not occur. It does, just that the intensity of it under certain conditions might be too low to allow extensive pileups that are seen in soft and ductile aluminum alloys.

Table 4.2 Effect of cutting speed and rake angle on the cutting, thrust and friction forces.

Cutting conditions		**F_c (N)**	**F_t (N)**	**F (N)**
	V (m/s)			
α = 20 deg	1	800	780	1006.2
	3	620	550	728.2
	6	360	280	386.2
	Rake angle (deg)			
V = 6 m/s	5	600	570	620.1
	20	360	280	386.2
	35	180	50	144.2

Process Map

For any machining process, achieving an absolutely smooth surface is almost impossible, but regulating both the material and cutting conditions can result in improved chip and workpiece surfaces. Increasing the cutting speed and rake angle have been shown to play crucial roles in suppressing the phenomena for fold formation by reducing sticking conditions and redundant deformation. Although beneficial to regulating fold formation, altering the cutting conditions can also lead to undesirable chip properties and tool damages. Therefore, an optimum cutting condition is necessary for machining these complicated materials that are prone to multiscale folding.

Presented over a wide range of experimental conditions is a collection of chips in a process map (**Fig. 4.15**) that shows varying fold shapes and sizes based on the cutting conditions. At low rake angles ($\alpha < 20$ deg) and cutting speeds ($V < 6$ m/s), the flow mechanism is dominated by a strong combination of stick-slip and sinuous flow which results in chips consisting of both the large-amplitude and lamella folds on the free surfaces. At higher rake angles ($\alpha > 35$ deg), the cutting speed effect is minimized with barely any change in chip morphology for the range of cutting speeds. The dominant flow mechanism under these conditions is lamina flow that results in thinner chips with limited redundant deformation and improved surface finish. The shear strain imposed on the chips also reduces due to the decreased chip thickness. The conditions between these two extremes (i.e., $20^o \leq \alpha \leq 35^o$ for $V > 3$ m/s) offer a transition where cutting can be optimized to produce chips with minimal folds at appreciable strains. Depending on the application and property requirements, such chips may be suitable for use as final products or half-products for secondary processing either through cold rolling or wire drawing [44].

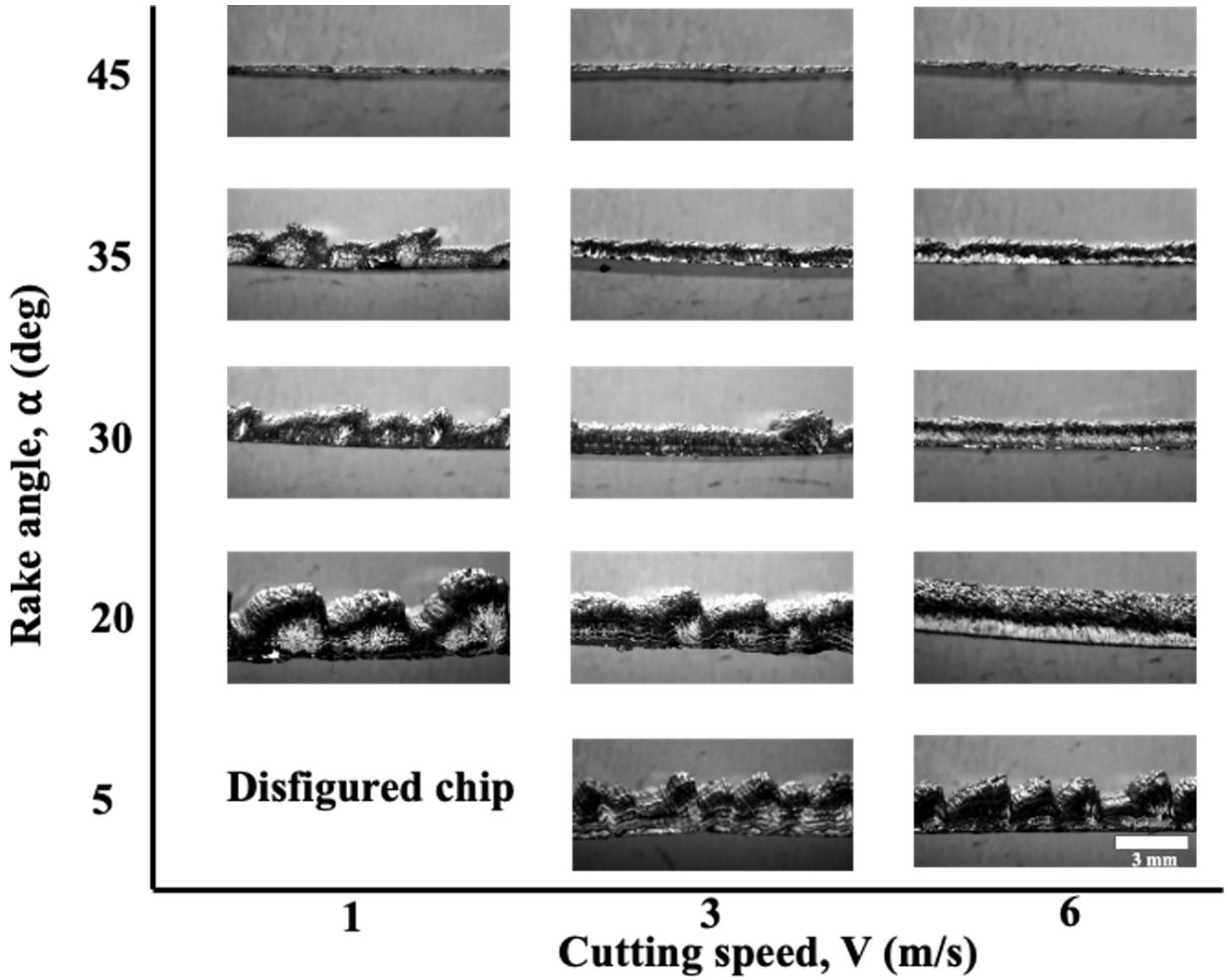

Fig. 4.15 Process map showing chip surface morphology controlled by the rake angle and cutting speed under dry cutting conditions of as-cast AA8040. Images are unpolished side-view of chips taken with optical stereoscope.

The flow characteristics of the soft and ductile alloys as evidenced by the multiscale folding proves challenging when appropriate deformation conditions are not selected. Under conditions of dominant stick-slip (rake angle, $\alpha = 5^o$ and $V_o = 1$ m/s for $t_o = 0.13$ mm) in **Fig. 4.15** the deformation causes large material pileup ahead of the upper tool (**Fig. 4.16**). Typically, the cutting tool assembly in FM is similar to the constrained configuration in HCE with the exception being that a very large chip exit channel is created in FM to avoid any constraining effect on the chip. Even under such conditions, the formation of the large folds spare no room to fill the exit channel and pileup ahead of the upper tool. Instances like these catastrophically stall the chip formation process. This also becomes a challenge for applying constrained deformation through HCE if

appropriate cutting conditions are not selected. It is for this reason that the process map (**Fig. 4.15**) is developed as a reference chart for the chip morphology that is likely to occur at a given rake angle and cutting speed on materials with similar deformation characteristics as the 8040 and 1100.

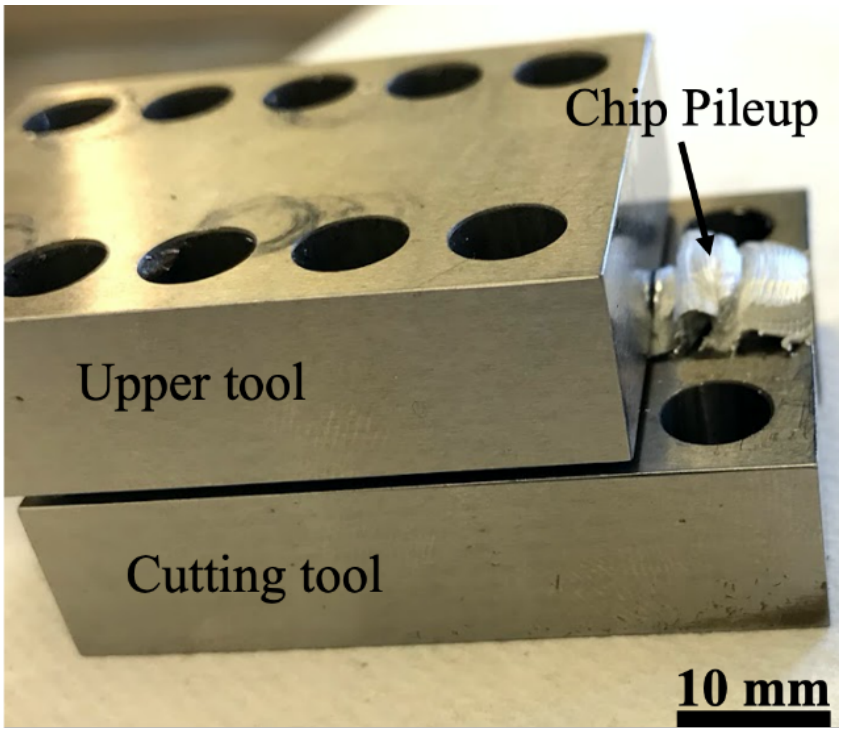

Fig. 4.16 An image cutting tool assembly showing chip pileup under conditions of dominant stick-slip.

Flow Suppression via HCE

Plastic deformation at small length scales on surfaces is intrinsic to machining processes. The near-surface plastic flow determines how the material is separated from the workpiece due to the action of the cutting tool. The plastic flow also determines the characteristics of the newly generated surface such as the surface quality, microstructure, and strength [80]. Unlike in bulk deformation processing, the unique feature of machining processes is the unconfined nature of material flow which has been recognized to trigger plastic flow instabilities of various kinds [36,40,81]. The variety of observed chip types such as the saw-tooth chips resulting from shear banding and segmentation; the lamella structures from sinuous flow, and the large amplitude folds from stick-slip all bear testament to the diversity of the unconstrained flow instabilities in machining. These

observations suggest that if the chip formation process could be modified by the application of a suitable constraint, then opportunities may exist for suppressing the flow instabilities. This is what is explored using HCE (**Fig. 2.6b**) – the hybrid cutting and extrusion model that couples the cutting tool with the constraining tool for purposes of constraining the flow to limit the occurrence of flow instabilities, specifically, the multiscale folding in the soft aluminum alloys.

Fig. 4.17 demonstrates the successful outcome of the constrained HCE process in suppressing the fold formation in the 1350 and 8040 alloys. The imposed constraint level $\lambda_{Imp} = t_c/t_o$, was 5.0 for 1350 and 7.0 for the 8040 following the unconstrained chip thickness ratios, λ_{Nat}, of 6.9 and 10.0, respectively. The uniformity of the HCE chip (**Fig. 4.17b and d**) microstructure is an unambiguous signature of the flow suppression effect of the HCE process especially when contrasted with the FM chips (**Fig. 4.17a and c**). The transformation of the mushroom-like structures in the FM cases to the smooth constrained faces in HCE is quite remarkable. The HCE process has also been successful in suppressing segmentation in Mg alloys and shear banding in Ti alloys [80].

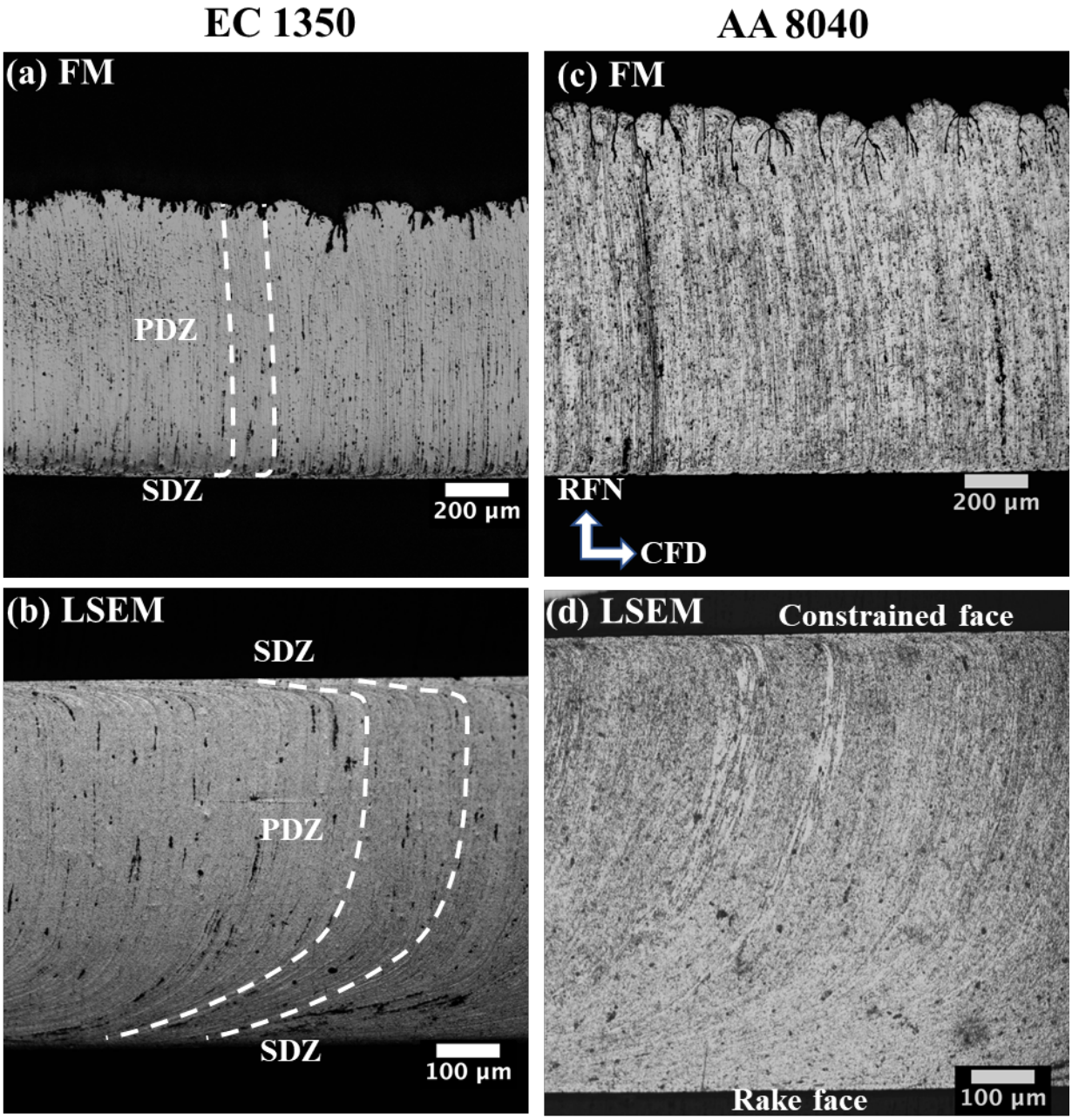

Fig. 4.17 Suppression of fold formation by constrained cutting. a) and c) FM chips with mushroom folds in 1350 and 8040 alloys and b) and d) HCE chips with suppressed folds on the constrained surface. b) is produced at a $\lambda_{imp} = 5.0$ and d) at $\lambda_{imp} = 7.0$.

Examination of the entire microstructure of both FM and HCE chips provides usefulness for understanding the nature of the deformation in the chips under these processes. Based on the flow line pattern in FM, two regions of intense deformation can be identified. The first is due to the

primary shear plane deformation, which gives rise to the nearly straight flow lines in the bulk of the chip that are oriented nearly perpendicular to the chip rake face (see PDZ in **Fig. 4.17a)**. These flow lines are lines of maximum elongation and not the direction of maximum shear (shear plane), as is sometimes mistakenly assumed [82]. The second is due to frictional deformation at the tool-chip contact along the rake face, region SDZ (Secondary Deformation Zone) in **Fig. 4.17a**. Because of the frictional drag along the rake face, these lines are inclined at an acute angle, almost parallel, to the chip rake face in contact with this tool face. The large deformation within these zones causes the grains and second phase particles to be reoriented along the flow lines. The angle between the flow lines and shear plane is directly related to the shear strain imposed in the PDZ. In contrast to the primary deformation, which is imposed throughout the chip, the SDZ arising from friction is quite shallow, extending only about 5-10 μm deep into the chip from the rake face. The free (back) surfaces of the chips have the mushroom-like structures, all along this surface. These structures arise from the unconstrained flow of the material as noted earlier. The applied deformation conditions on the chips were also selected within the region where sinuous flow is the dominant flow mechanism as described in **Fig. 4.15**. Under these conditions, stick-slip is minimal, allowing for decreased occurrence of the large amplitude folds.

The application of the constraint via HCE suppresses of the formation of the mushroom-like structures (unsteady flow/instability) on the back side of the chip **(Fig. 4.17a and c)**. Hence, in contrast to the FM chip, the HCE chips show negligible surface waviness along the chip flow direction (CFD). Unlike FM, the HCE chip microstructure contains an additional SDZ due to the chip drag-interaction with the constraining tool (**Fig. 4.17b and d**). The SDZs are highly deformed regions, as revealed by the flow line structure, and the depth to which these lines extend into the chip thickness shows the extent of the surface strain. The SDZ on the rake face side of the chip due to the main cutting tool extends to a greater depth than the one due to the constraining tool. It is a consequence of the larger stresses imposed by the cutting tool. These differences in the secondary shear zone extent are enhanced with decreasing λ.

The commercially pure aluminum alloys in strain-hardened conditions are highly susceptible to recovery and recrystallization, even at temperatures as low as 80^{o}C [8]. The calculated adiabatic temperature rise, based on measured cutting forces for λ = 5 in the 1350, is 100^{o}C to 125^{o}C and increases with decreasing λ [13]. Due to greater deformation-induced adiabatic heating, the HCE

chips can undergo dynamic recovery or recrystallization depending upon the extent of the constraint used. **Figure 4.18b** show recrystallized microstructure in HCE chip with $\lambda = 1.5$ for the 1350 alloy. This is reflected in the substantially smaller grain size of ~5 μm in the chip, as against a starting grain size of ~200 μm (see **Fig. 3.1**). This example of deformation control in HCE illustrates how finished chips with an annealed microstructure can also be produced in a single step, by making use of *in situ* dynamic recrystallization, without need for a separate annealing heat treatment.

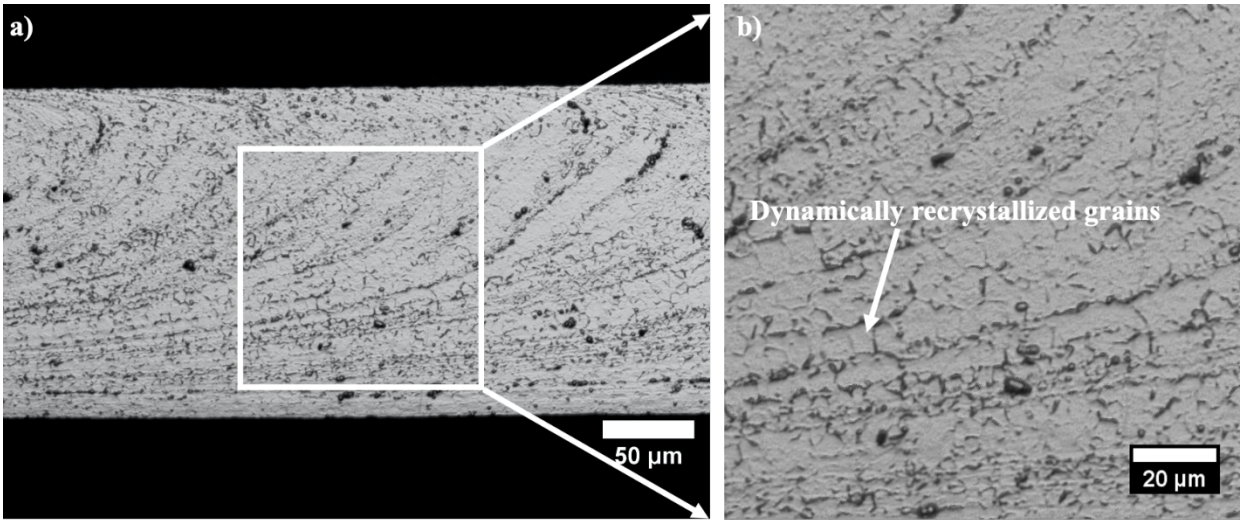

Fig. 4.18 Optical micrographs of microstructure of EC1350 HCE chips: a) $\lambda = 1.5$. b) is higher magnification view of the demarcated region in a), with dynamically recrystallized grains resulting from adiabatic deformation-induced heating during wire formation.

Although HCE promises deformation control through the constraining capability, large deformation forces higher than FM conditions are typically seen in HCE, suggesting of higher energy requirements of the process to produce the chips. **Fig. 4.19** compares the cutting forces in HCE with FM in the 8040 alloy. It is interesting that although the chip thickness, and thus the imposed strain in HCE is lower compared to FM, higher cutting forces are required to produce the chips. In fact, as λ decreases (thiner chips), the cutting forces increase. This can be attributed to the large volume of material that must be compressed and forced through the die (chip exit channel). These large forces can potentially make the HCE process a little more expensive to its FM counterpart.

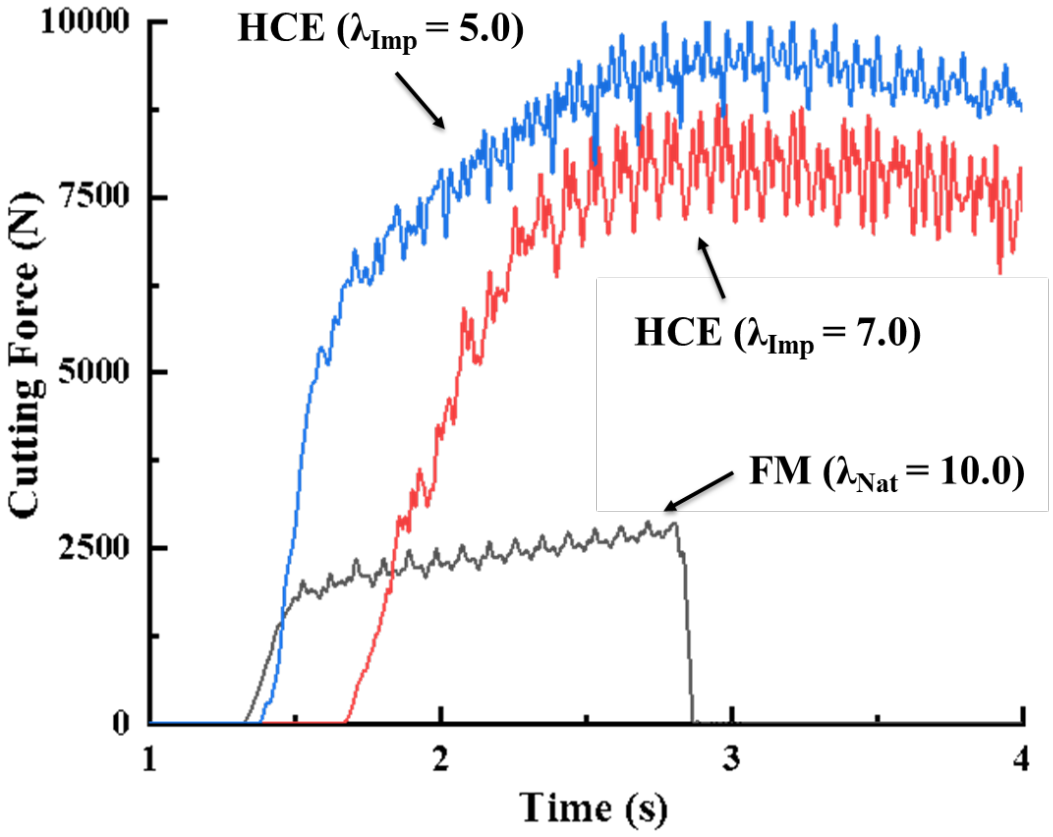

Fig. 4.19 A time domain plot of cutting forces for FM and HCE in 8040 alloy. HCE Cutting forces are more than 2X the forces in FM. There is also a slight rise in the forces as the λ decreases.

5. SURFACE METROLOGY OF MACHINED CHIPS

This chapter presents an overview of the nature of surfaces that are characteristic to machining processes. The nature of surfaces has long been recognized as having a major impact on product performance, longevity and reliability [83]. Surface alterations due to mechanical, metallurgical, chemical and other factors can limit the component quality or may, in some cases, render the surface unacceptable [84]. A basic understanding of the changes in the condition of the surface is therefore required to improve the product quality. The first part of the chapter reviews the fundamental theories of surface metrology that are used for characterizing surface quality. The second part discusses the nature of the surfaces of FM and HCE chips and the implications on the chip performance.

5.1 Fundamental Theories of Surface Roughness

The satisfactory functioning of many modern technologies depends on the nature of the surfaces of the components. This is especially true in wear-resistant components, as their surfaces must perform many engineering functions in a variety of complex environments [85]. Machining processes applied in industry to produce the desired shapes in the components often leave features that mar the strict dimensional tolerances and surface quality requirements of those components. Surface topography and texture is a foremost characteristic among the surface quality properties that are impacted by the machining production method and the parent material flow behavior during the deformation [36,86]. Over the years, the evaluation and characterization of surface texture has constituted a challenging metrological problem especially when high precision or functional requirements are desired [87–89]. For instance, the distinction between a smooth and rough surface may be evaluated and characterized by touch and/ or by visual inspection because the surfaces may feel different when handled or may reflect light differently. But these methods of inspection, although, helpful in enabling us to differentiate between these surfaces, are in actuality, subjective to the observer, especially for the surfaces that are fairly rough or fairly smooth. In engineering applications, the exact degree of the roughness can be of considerable importance to the functioning of the component and therefore requires in numerical terms, descriptors that universally quantify how rough or smooth a surface is [90]. This led to the development of

standards that globalizes the understanding of surface texture. Some of those standards includes ISO 25178 and ASME B46.01-2019 [91,92].

When surfaces are studied carefully on a fine scale, they are all found to be rough; the roughness being a characteristic of asperities of varying amplitudes and spacing [83]. The asperities can be directional when the finishing process is direction dependent, such as in milling and turning [93]. They can also be homogeneous for non-directional finishing such as in electropolishing [83,94]. Surface textures are usually a complicated mixture of surface features which may include roughness (nano and microroughness), waviness (macroroughness), lay and flaws (Fig. 5.1) [83]. The roughness consists of features of shorter wavelengths resulting from intrinsic production process while the longer wavelength features constitute the surface waviness. The wavy features are typically related to machine or workpiece deflections such as vibrations, chatter, and warping strains [95]. The lay of the surface shows the principal direction of the predominant surface patterns, and flaws are expected interruptions in the texture.

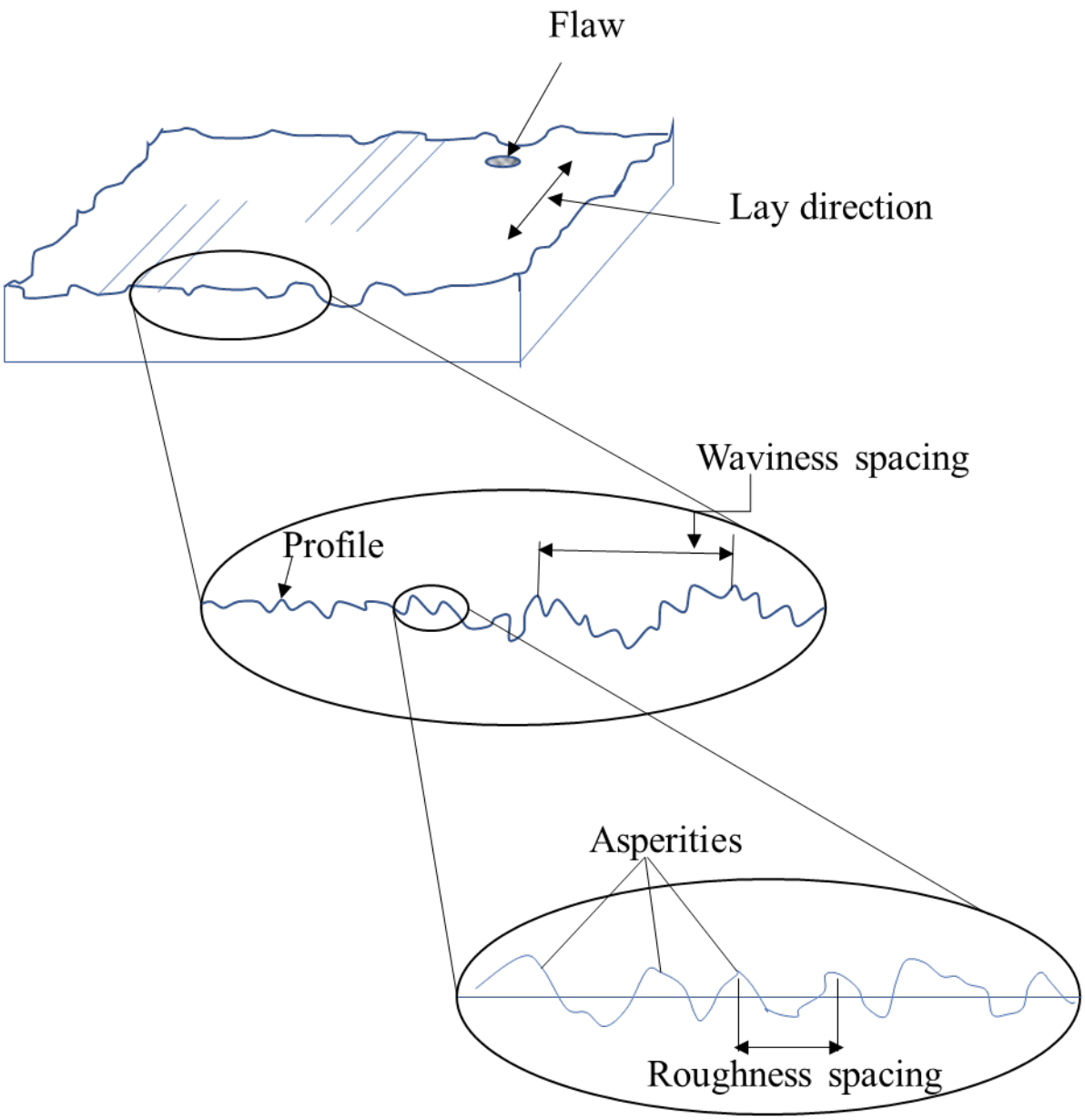

Fig. 5.1 A schematic of surface texture showing the surface features at different length scales. Figure modified after [86].

Surface Texture Parameters

Surface texture as already indicated is a complex combination of many surface features that define a surface based on the production method applied to it. It has also been pointed out that subjective techniques such as touch or visual inspection are not adequate in providing a universal connotation

for describing surface texture. Therefore, numerical assessment is adopted via surface texture parameters. Because of the complexity of surfaces, no one parameter has been found to quantify all the various features on a surface. The parameters are grouped into three categories depending on the characteristics of the feature that is quantified [90,92,95–97]:

1) Amplitude parameters: These are solely determined by peak or valley heights or both.

2) Wavelength (Spacing) parameters: These are determined by the spacing of irregularities along the surface.

3) Hybrid parameters: Considers the combination of amplitude and spacing parameters.

For the purposes of this study, only the amplitude and spacing parameters will be reviewed in detail, because the hybrid parameters are largely concerned with features that are less critical to our investigation such as the profile slope and peak curvatures.

Amplitude Parameters

These parameters are usually characterized by the height descriptors advocated by the international Standardization Organization (ISO) and the American National Standards Institute (ANSI) [96,97]. They include the center-line average roughness (R_a), the Root Mean Square values (R_q), the highest peak (R_p) and deepest valley (R_v) [95]. Two other statistical height descriptors that are rarely use are Skewness (S_k) which measures the symmetry of the height discrepancies, and kurtosis (K) which is concerned with the measure of the sharpness of the peaks [83,91].

The R_a value is the arithmetic mean deviation of the surface height from the mean line profile (**Fig. 5.2**). Mathematically it is given by **equation 5.1** [86,92]. The mean line of the profile is not selected arbitrarily but it is drawn to have equal areas above and below the line. Generally, the line is drawn parallel to the general profile of the surface. This criterion, however, is not unique as there may be many other such lines that meet this condition but differing in slope relative to the profile. Thus, a different reference line called the least squares mean line is sometimes used [90]. This line is positioned such that the sum of the squares of the deviations of the profile is a minimum.

$$R_a = \frac{1}{L}\int_0^L |Z(x)|\,dx \tag{5.1}$$

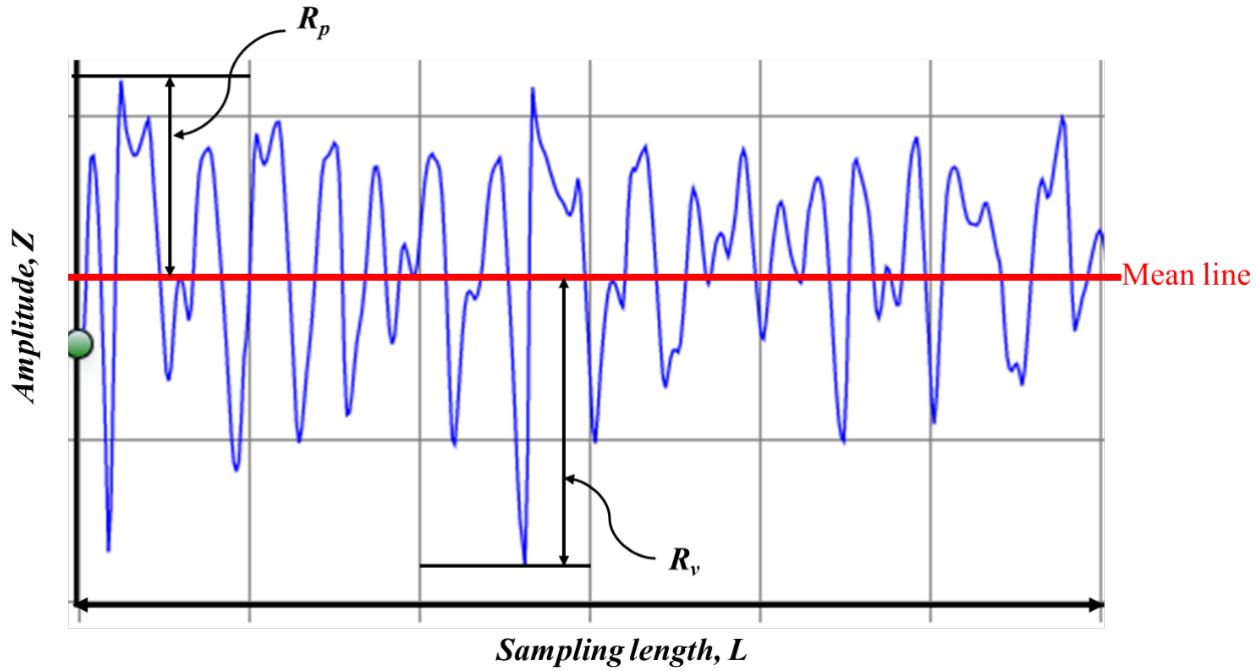

Fig. 5.2 Center-line average of the amplitude, Z of a surface profile over a sampling length, L.

It is useful to underscore the importance of the sampling length as well. Usually, surfaces exhibit both roughness (short wavelength features) and waviness (long wavelength features), both of which are substantially repetitive and thus, requires a representative sampling length that will be true over the entire profile. Consider **Fig. 5.3**, if a sampling length, x is selected for this profile, the roughness pattern at A and B will provide a close estimate of the surface roughness because they only differ in minor details that can be overlooked. However, if a shorter length, y is chosen, the roughness patterns at C and D will provide a misleading picture of the surface roughness. To avoid these discrepancies, a cut-off sampling length is typically specified to give meaning to the R_a values and to enhance the replicability of the measurement. The R_a is only repeatable if the same cutoff is used on a given surface profile. In surface profile measuring instruments, filters are usually applied to modify the profile waveform to give the cut-off length. Based on experience for manufactured surfaces, the standard cut-off lengths that have been recognized to roughly represent the boundaries between waviness and roughness are 2.5, 0.8, 0.25 and 0.08 mm. These values are

nominally chosen to have a ratio of $\sqrt{10}$, one to the next [88,95].

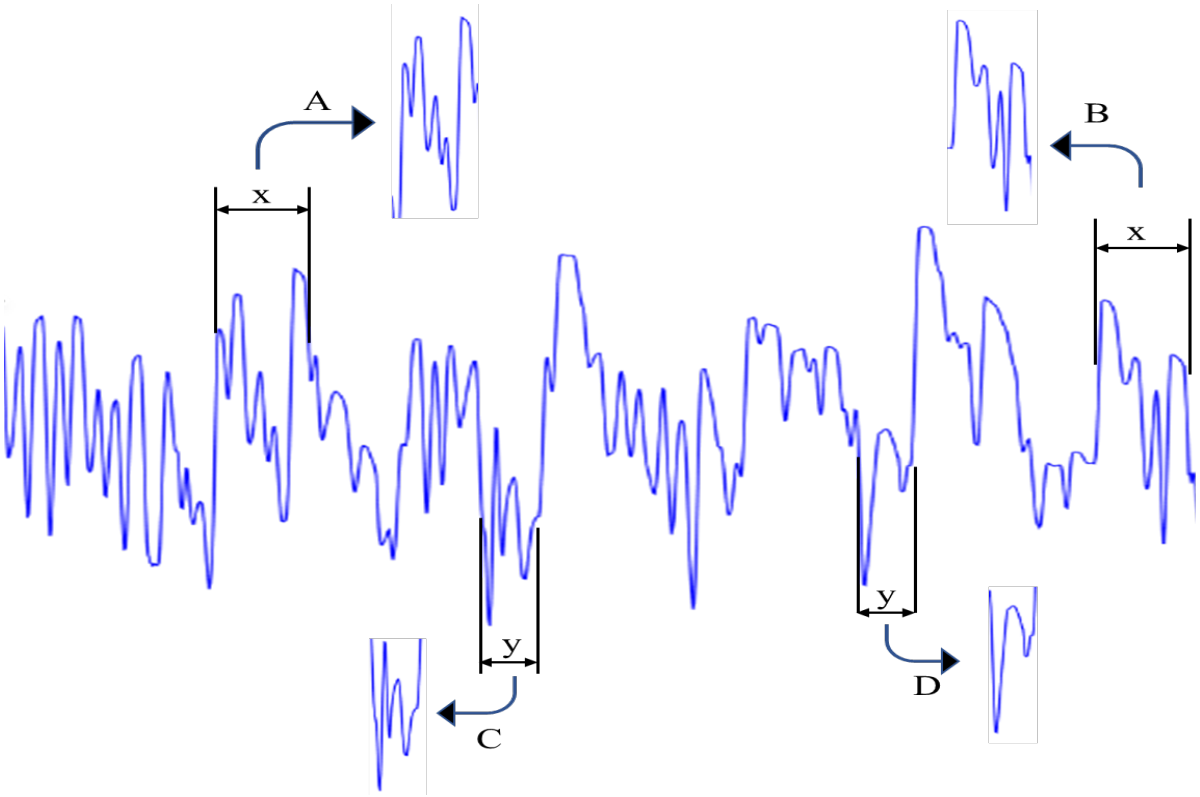

Fig. 5.3 A sample profile showing the effect of sampling length. Modified after [90]

The R_q parameter is the root mean square value of the surface profile and represents the standard deviation of the distribution of the surface heights about the mean line. This parameter is more sensitive to the variations in the peaks and valleys than the R_a [83]. It is represented mathematically by **equation 5.2** [91,92].

$$R_q = \sqrt{\frac{1}{L}\int_0^L [Z(x)]^2 \, dx} \tag{5.2}$$

It is sometimes desirable to specify the peak (R_p) to valley (R_v) heights (see **Fig. 5.2**) rather than the R_a values. The peak-to-valley heights often designated as R_{max} represents the maximum roughness height. For very rough surfaces, this parameter correlates well with tactile assessments when the surface is handled [90].

Spacing Parameters

The amplitude parameters are mostly specified for machined components but for a complete characterization of a surface, these parameters are not sufficient [91,92]. The amplitude parameters are primarily concerned with the relative departure of the profile in the vertical direction only with no information about slopes, shapes and sizes of the irregular surface features. Thus, the spacing parameters are used to supplement the information provided by the amplitude parameters.

The spacing parameters provide some index of the crest spacing or wavelength (λ) of the surface. This typically corresponds to the lateral or spatial distribution of the surface features [86]. Two parameters that are occasionally used are the peak density (S) and zero crossings (S_m) [86,95]. The peak density of the profile basically counts the number of peaks per unit length (**Fig. 5.4a**). The difficulty with this method lies in determining what constitutes a peak in a profile that has a complex combination of smaller (local peaks) and larger peaks (profile peaks) [90]. Consider **Fig. 5.4b**, A and B are considered profile peaks while a-f are local peaks. For a local peak to be considered in an evaluation of S, h must be greater than 1% of the R_p [90]. This criterion is referred to as amplitude discrimination [95]. By this criterion, local peaks e and f will be considered as peaks while a-d will be rejected in the evaluation of S (**Fig. 5.4b**). The zero-crossing parameter (S_m) on the other hand, measures the number of crossings of the profile through the mean line (**Fig. 5.4c**). Within an evaluation length, the mean value of the spacing between the irregular features can be estimated by S_m.

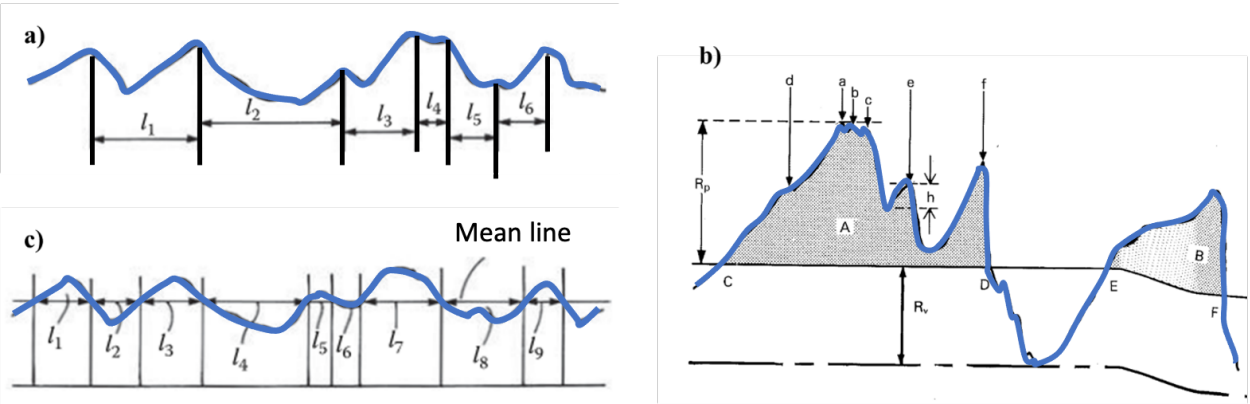

Fig. 5.4 Schematics showing a) peak count measurement of S, b) peak discrimination criterion used in determining what constitutes peaks or otherwise in a profile, and c) the zero crossing technique for measuring S_m. Figures modified after [90,95]

Power Spectral Density, PSD

To determine the average wavelength λ_a of surface irregularities, power spectral density analysis is typically performed by utilizing the information of both the S and S_m parameters [98–102]. In principle, PSD can be evaluated via the autocorrelation function or by Fourier transform of the data [103]. The former is essentially a process for determining the relationship of any point on the profile to all other points. If a profile is periodic, the relationship of a particular group of points will repeat at a distance equal to the wavelength. The precise relationship of random irregularities will not recur anywhere along the profile [95,98]. On the latter, PSD is determined by taking the square of the Fourier transform (FFT) of the surface profile (**equation 5.3**) to capture just the power and not the phase across the range of spatial frequencies [100,104]. The Fourier analysis decomposes the surface profile into a series of constituent sine waves (harmonics) having spatial frequencies which are multiples of the lowest frequency [90].

$$PSD(F) = \lim_{L\to\infty} \frac{1}{L} \left| \int_0^L y(x) e^{-i2\Pi Fx} dx \right|^2 \tag{5.3}$$

Where, L is the surface profile length, and F is the spatial frequency.

Figure. 5.5 shows the decomposition of the spatial frequencies in a PSD plot of the surface profile along a slice on the surface of an Al 1100 machined chip. The spatial wavelength (spacing) of a surface feature is the inverse of the spatial frequency (represented as peaks) for that feature. Generally speaking, to obtain a true PSD of the surface that has random roughness, an average of the PSD estimates calculated from single profile (such as the surface profile in **Fig 5.5** inset) is required for different locations on the surface. A PSD calculated from a single profile measurement will be meaningless since the measurement will not be representative and reproducible.

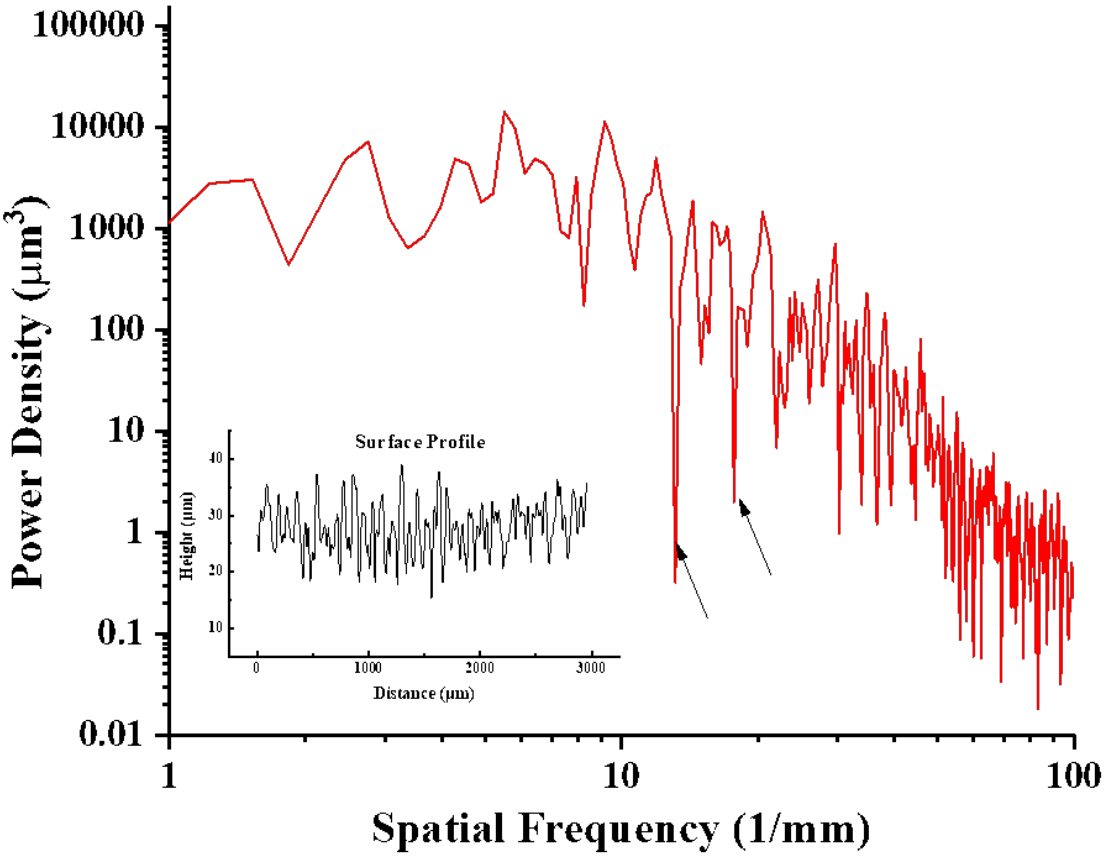

Fig. 5.5 Log-log PSD plot generated by decomposition of a line profile (inset) into the various frequencies corresponding to the spacing of the features on the surface. The inset is the line profile from which the PSD plot is generated.

5.2 Surface Topography of FM and HCE Chips

Long, continuous chips, 6 mm wide and 0.2 to 0.9 mm in thickness (rectangular cross-sections), were produced from disk-shaped workpieces using the FM and HCE (**Fig. 5.6**). The deformation was done at an uncut chip thickness, t_o = 0.13 mm, a rake angle, $\alpha = 20^o$, and V_o = 6 m/s. This condition was deemed optimal to limit stick slip (for avoidance of large-amplitude folds) and to maintain an appreciable amount of strain imposed on the chips for strengthening purposes due to plastic deformation. The HCE chips were produced at an imposed constraint, $\lambda_{Imp} = 5$, following a $\lambda_{Nat} > 6$ in the FM condition.

The FM chips exhibit a smooth and shiny appearance on one face – the side in contact with the tool rake face – and a matte (dull) surface on the other side (chip free surface). The latter is a

consequence of unconstrained flow of the material as already discussed in chapter 4. The HCE chips, on the other hand, show similar, smooth shiny surface finish on both of the chip faces - the rake and constraint face sides (**Fig. 5.6b).** The HCE constraint prevents material flow normal to the surface on the back side of the chip and this restraint is the primary reason for the improved smooth appearance.

Fig. 5.6 Coils of Al 1100 chip produced by a) FM and b) HCE. The chips are intentionally coiled after the processing to show long samples.

The Surface quality (topography, roughness) of the chips was measured with a 3D optical profilometer (Zygo NewView 9000). Surface profiles were generated from an area, 3 mm by 3 mm, at a lateral resolution of 2.9 µm. Both surfaces (rake face and free/constrained surfaces) of the chips were profiled. Following ASME (B46.1-2019) standards [92] and Rank Taylor Hobson [90] recommendations, the *Ra* values were determined by applying a Gaussian filter with cutoff wavelength of 250 µm. This filter cutoff was deemed to be best suited for the topographical features observed on the chip surfaces. A minimum of 20 line scans across the chip surfaces were considered. The direction of the line scans was selected to be parallel to the chip length-direction since this is perpendicular to the lay of the FM chip free surface. All three alloy system (1100, 1350 and 8040) were investigated but the results of the 1100 and 1350 are presented in this section.

This is because the FM chips produced under predominant sinuous flow cutting conditions have similar surfaces.

FM Chips

Optical profilometry **(Figs. 5.7a and b)** revealed that the unconstrained sinuous flow occurs across the entire width of the free (back) surface of the FM chips, resulting in ridges running perpendicular to the chip flow direction (CFD). Additionally, fine tool marks can be seen along the CFD arising from nonuniformity of the tool cutting edge.

The surface roughness along the wire back surface, expressed in terms of the arithmetic mean height (R_a), is 4.5 μm and 8.9 μm for the Al 1100 and EC1350 alloy, respectively. These represent somewhat rough surfaces, especially when compared with commercial strip products. Typical finish limits for commercially drawn flat wires are in the range of R_a = 0.8 to 3.3 μm [90], and between 0.4 to 0.8 μm for rolled products [105,106]. The roughness of the chips arises mainly from the sinuous flow mode coupled with the large initial workpiece grain size (50 - 200 μm), and may necessitate the use of a follow-on, light cold drawing or rolling step to improve the surface finish. As will be seen, this roughness is minimized in the HCE by use of the constraint, which suppresses the sinuous flow. In contrast, the shiny chip surfaces that arise from contact with the tool rake face (**Fig. 5.6a**) have much smaller R_a values, between 0.24 and 0.31 μm (**Fig. 5.7c and d**), for both the Al 1100 and EC1350 alloy. This is more than an order of magnitude smaller than the R_a on the FM chip free surface, and far superior to that of drawn or rolled products.

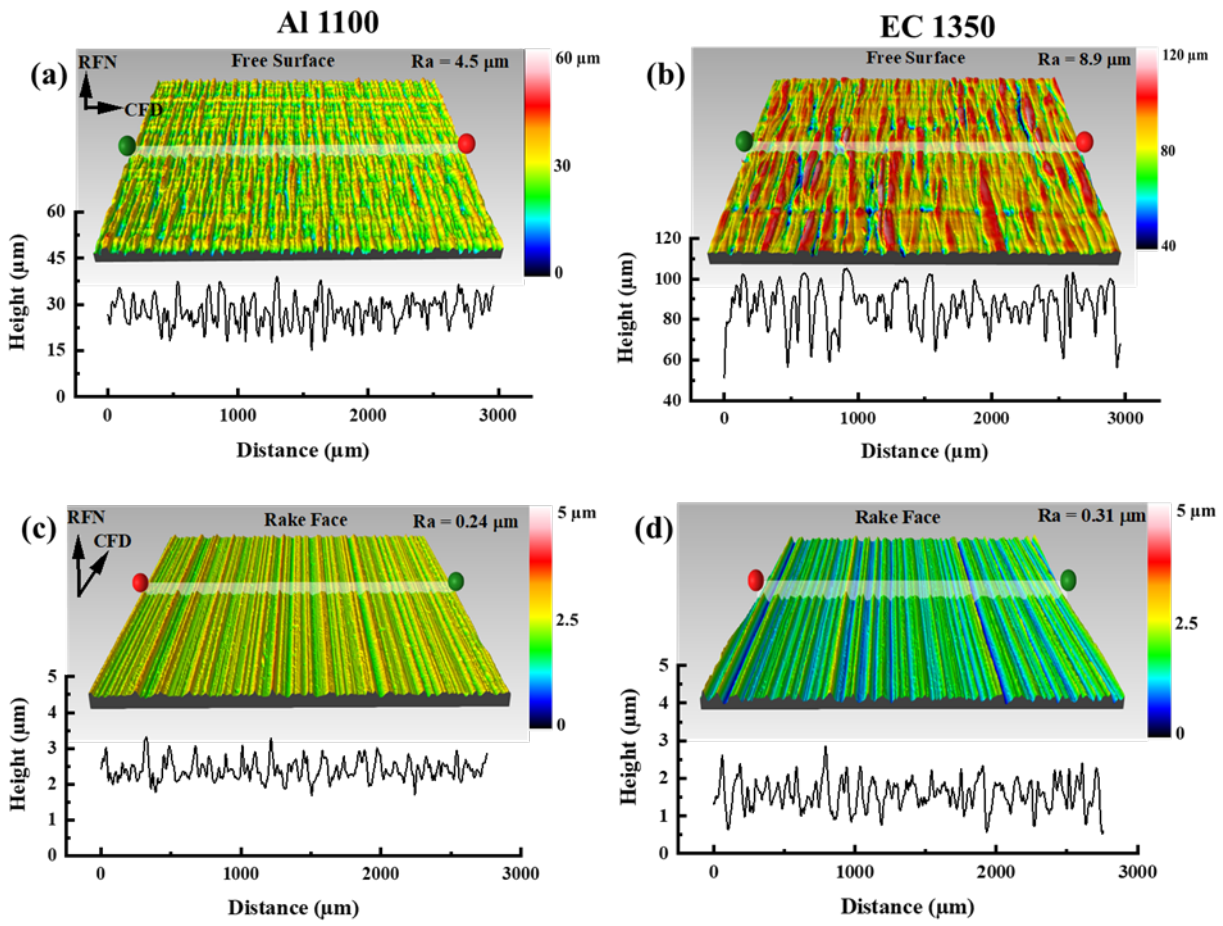

Fig. 5.7 3D profilometry data showing surface topography of the FM wires on the free surface (a and b) and rake face (c and d). Also shown are line profiles along specific marked sections of the wire. Ra values are calculated with a Gaussian cutoff wavelength of 250 µm.

Sinuous flow is triggered by plastic buckling of grains followed by material folding in the deformation zone [61]. The higher frequency of the ridges on the free (unconstrained) surface (**Fig. 5.7a**) in the Al 1100 alloy, as shown by the height profiles in the CFD-RFN plane along the length, correlates with the smaller starting grain size of the Al 1100 alloy (~50 µm), as against a smaller frequency in the larger grain size (~200 µm) EC1350 alloy (**Fig. 5.7b**). This was confirmed by PSD analysis performed on the surface profiles generated from the free surfaces of the FM chips. High power density peaks at spatial frequencies (**Fig. 5.8 b and c**) corresponding to the spacing of the mushroom features were seen to be consistent with the initial grain sizes of the materials. The feature spacing corresponding to the low frequency 1350 peak (**Fig. 5.8b**) is ~200 µm and that

for the 1100 (**Fig. 5.8c**) is ~50 µm. Interestingly, with fine-grained/pre-worked alloys, with less ductility, the flow is usually uniform with much smaller ridges on the chip back surface [36]. The PSD analysis can be a useful technique to predict grain size of the material based on the spacing information of the free surface features if deformation conditions permit sinuous flow.

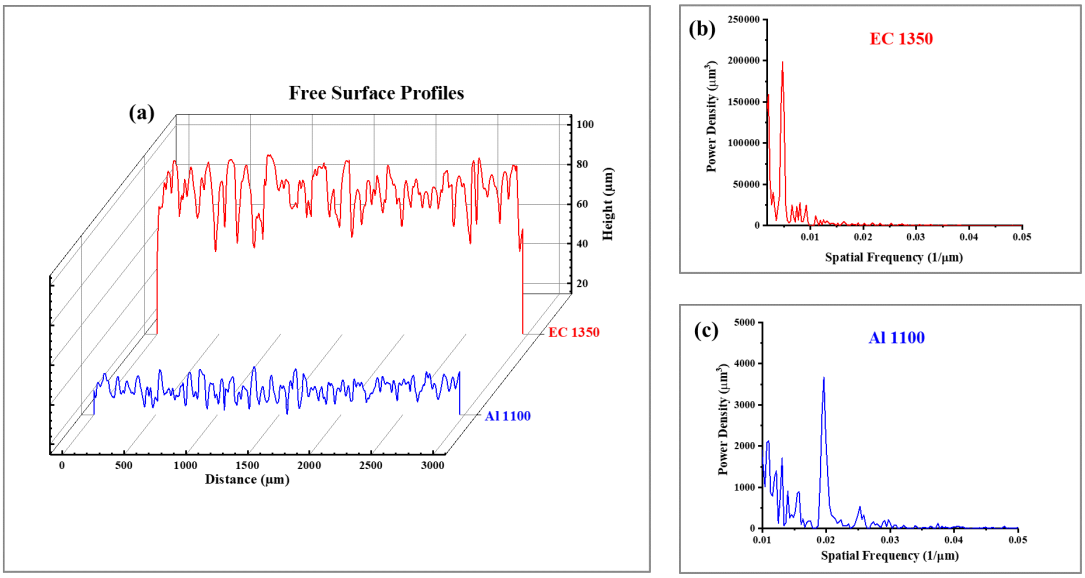

Fig. 5.8 Plots showing a) free surface profiles of the 1350 and 1100 FM chips, b) and c) are the power spectral density plots showing peaks with spacing consistent with the spacing of the mushroom features in both alloys.

HCE Chips

By applying a sufficient constraint to the chip back surface, the degree of freedom available for sinuous flow development within the deformation zone is removed [36]. This is what is done in HCE by adjusting the constraint level (λ) in the deformation zone. The HCE constraint greatly reduces the surface roughness (R_a = 0.36 µm) on the chip back surface (see **Fig. 5.9)**, compared to that in the FM. In fact, this roughness is now close to that recorded (R_a = 0.25 µm) on the chip rake-face side. It also shows that the constraint contact condition is very similar to that on the rake face. Overall, the HCE chip surface roughness is superior to that of strip products by cold rolling or drawing [105]. The very good surface finishes resulting from the HCE offer a promising

pathway to producing chips directly from annealed/as-cast workpieces, with significantly reduced processing steps compared to traditional processing routes.

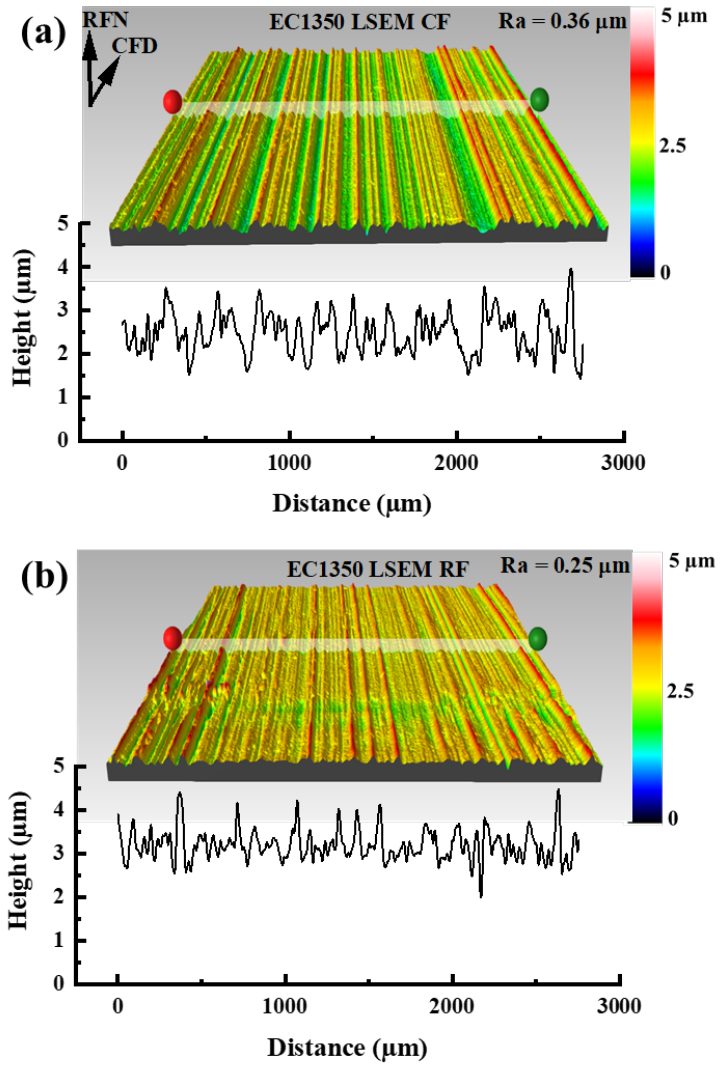

Fig. 5.9 3D optical profilometry data showing surface topography on the HCE chips on a) constraint face (CF) and b) rake face (RF); $\lambda = 5.0$.

6. IMPLICATIONS OF SHEAR-BASED DEFORMATION PROCESSES

This chapter shows the potential of the FM and HCE techniques in the production of electrical conductor wires. The key performance indicators for electrical wires (strength, electrical conductivity, and surface finish) are discussed and compared with conventionally processed wires.

6.1 Production of Electrical Conductor Wires

Before the advent of continuous wirebar casting over 50 years ago, delivering wire products in the various temper conditions was achieved through a long and expensive, three-stage processing route - casting ingots, rod rolling and wire drawing [107]. Still a standard today, coilable wirerod commonly called redraw rod, is produced in standard sizes of 9.5 and 12.7 mm diameter [107–109]. From the rod rolling stage, the redraw rod is then processed through a series of incremental wire drawing or cold rolling passes/steps (typically 10 to 20) to the final round or flat wire form. Standardized flat wire dimensions range between 1.6 mm and 12.5 mm in width, and 0.6 mm to 7 mm in thickness [110]. Typical final round-wire diameter ranges between 0.2 mm and 6.5 mm [111]. To reduce the number of production steps and cost of producing wire-rod, almost all of the recent industrial casting practices have fused the casting and rod rolling stages into a single continuous in-line process. Wheel-belt continuous casting machines feed the cast bar directly into a multi-stand rolling mill **(Fig. 6.1)**. Properzi and Southwire continuous casting systems are examples of commercial processes used in production of continuously cast and rolled Al wirerods [112]. Nevertheless, multiple reduction steps (typically 10 to 20) by hot rolling are still an intrinsic feature of wire-rod production by these in-line processes.

While there have been the aforementioned advances in wirerod production, the cold-working stage in the process stream, which provides the preferred means of strengthening due to its small effect on electrical conductivity, has not seen any revolutionary measures that can reduce the number of deformation steps and yet deliver wire with the required properties. To avoid defects such as cracks and wrinkles, the typical area reduction per pass in cold rolling and wire drawing is seldom greater than 30% [113]. This low reduction per pass necessitates the use of many deformation passes, typically 10 to 20, to achieve the large shape change and desired mechanical properties in the wire products, especially hard-drawn wires (see stages enclosed in dotted rectangle in **Fig. 6.1**).

The overall wire process efficiency can be greatly improved if the number of passes in the plastic deformation processing stage can be reduced, preferably to a single pass. This is what comes in handy with the shear-based processes (FM and HCE).

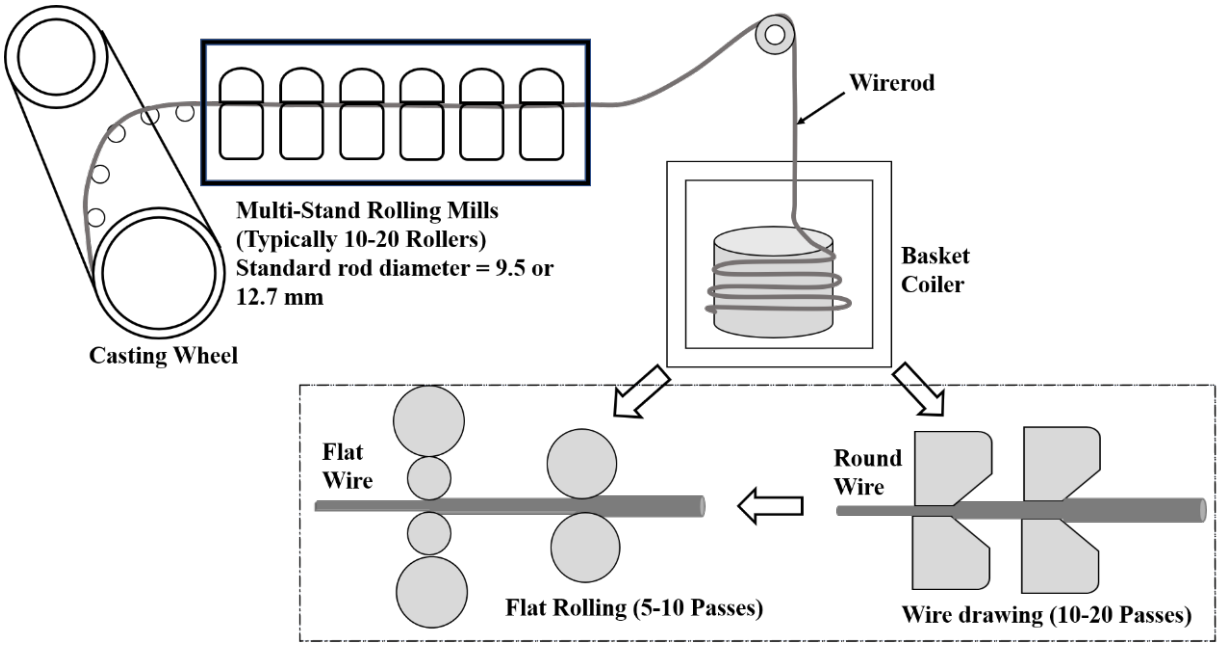

Fig. 6.1 Schematic of general the layout of continuous casting and rolling of aluminum rod (adapted based on [112])

It is noteworthy that severe plastic deformation (SPD) techniques, which can impose large strains well beyond what is achievable with conventional cold rolling and drawing methods, offer very little solution to the numerous processing passes in the plastic deformation stage. Equal Chanel Angular Pressing (ECAP) and some of its variants are prime examples of SPD techniques, which have shown promise in enhancing mechanical strength through grain refinement. But ECAP processes also involve multiple passes of deformation, with as many as 7 to 9 passes typically reported to reach the desired large strains [114–117]. Another drawback of ECAP is its inability to produce long continuous product forms of small cross-section due to the discrete (small length) billet workpiece. This has been partially rectified by development of ECAP-Conform, which combines ECAP and the continuous extrusion process known as Conform, to produce continuous wire forms [118,119]. In as much as ECAP-Conform can also effect grain refinement and improve mechanical properties, it is a complex process to set up and requires a workpiece that is already

available in long lengths. And, equally importantly, achieving a high degree of strain hardening still requires multiple passes of deformation [118,120–122].

The shear-based deformation processes, however, demonstrate a fundamentally different approach to producing chips that can be used as Al wire products; more remarkably so, in single-step of deformation. These techniques have the potential to replace the many steps in the current hot/cold rolling processing, thus making wire products less complex.

In assessing electrical conductor wires, three key property performance attributes are mechanical strength, electrical conductivity (=1/resistivity) and surface finish. These performance attributes of the FM and HCE chips (wires) are assessed in comparison with the conventional techniques of rolling and drawing.

Mechanical Properties

The material flow behavior in machining is characteristic to the alloy and its initial deformation state [14]. In conventional cutting or FM, ductile alloys such as the commercially pure aluminum of the present study exhibit a highly unsteady mode of material flow during chip formation – sinuous flow – characterized by extensive redundant deformation and vortex-like flow components [61]. The unsteady nature of this flow is responsible for the poor machinability of these alloys (workability), a characteristic often referred to as "gummy." This results in unusually thick wires in FM, with thickness ratios of $\lambda > 5$ in both alloys **(Table 6.1)**. The extensive thickening also implies that large strains are imposed in the wires **(Eq. 2.3)**. Based on dimension measurements on the wire, as well as direct *in situ* analysis of material flow via high-speed imaging, the effective strains in the FM wires were estimated, by the upper bound model, to be in the range of 3 to 4 for the two alloys **(Table 6.1)**. These estimates are necessarily conservative, given the redundant deformation resulting from the sinuous flow. At a $\lambda = 5$, effective strains as high as 2.8 are achievable in HCE wires. Keeping the undeformed chip thickness (t_o) constant, thinner wires, with smaller strain ~ 0.9, could be produced by setting $\lambda = 1.5$ **(Table 6.1).** It should be noted that HCE offers independent control of strain and thickness via the t_c and λ parameters.

Table 6.1 FM and HCE conditions and resulting strains in the wires.

	Cutting conditions			FM			HCE		
Alloy	t_o (mm)	α	V_o (m/s)	t_c (mm)	λ_{Nat}	ε	t_c (mm)	λ_{Imp}	ε
Al 1100	0.13	20°	6	0.72	5.7	3.2	0.64	5	2.8
EC1350				0.87	6.9	3.9	0.19	1.5	0.9

The high strain levels (~1 to 4) in the FM and HCE wires **(Table 6.1),** and associated hardening (**Table 6.2**), are similar to those occurring in SPD processes like ECAP. An important distinction is that in the machining-based processes, unlike the SPD processes and conventional rolling/ drawing, the shape changes and large plastic strains are accomplished in a single deformation pass.

Table 6.2 compares Vickers hardness and electrical conductivity of the machined wires with those of cold rolled and drawn wires in the H18 and H19 conditions. The H18 condition corresponds to a maximum cold rolling reduction of 75%, with residual ductility of only 1-4% uniform elongation (EL) depending on the form and process. The H19 temper, the highest commercial strain-hardened temper, corresponds to the maximum possible plastic reduction that leaves a minimum ductility of 1.2% EL [111] in round wire forms. Stranded conductors such as the Aluminum Conductor Steel Reinforced Cable (ACSR) are hard-drawn to the H19 condition to meet the high strength requirements of outdoor power transmission. The utility of the shear-based processes in increasing the hardness (strength) of the wires is evident. The hardness of these wires is 1.5 to 2.5 times that of the annealed workpieces (~25 HV), this increase being a consequence of the large strains imposed. The hardness of the FM and HCE wires compare favorably with those processed by multi-step cold rolling and wire drawing (H18 and H19 hard-rolled/drawn temper hardness), see **Table 6.2**. They are also close (within 15%) to that of commercially pure Al wires produced by the ECAP-Conform process after 4 passes [118]. The flexibility in controlling the deformation in the wires, via the shear-based processes, adds to the versatility of these processes.

Table 6.2 Vickers hardness and electrical conductivity of FM and HCE wires, and typical H18 and H19 tempers; HCE data is for $\lambda = 5$.

Alloy	Condition	HV	Electrical Conductivity (%IACS)
Al 1100	Annealed	27 ± 2	57.9 ± 0.2
	FM	63 ± 1	56.0 ± 0.2
	HCE	48 ± 1	58.2 ± 0.1
	H18	49[1]	57.0
EC1350	Annealed	25 ± 2	63.5 ± 0.5
	FM	56 ± 1	60.2 ± 0.7
	HCE	45 ± 3	62.3 ± 0.4
	H19	56[1]	61.0

Hardness values are from ASM Metals Handbook [10]. Al 1100-H18 is converted from BHN using an ASTM hardness conversion standard [123] and EC1350-H19 is estimated as HV ≈ $3\sigma_{UTS}$ (MPa) with UTS = 185 MPa [124]

Another mechanical property attribute, i.e., formability, of the FM and HCE wires is illustrated in **Fig. 6.2**. Despite the very large level of plastic strain imposed during the FM ($\varepsilon = 3.2$), the wires are seen to exhibit surprisingly high formability in 0T bend testing. At the bend radius of "zero", where the wire is flattened onto itself, the maximum circumferential (bend) strain is at least $\varepsilon \sim 1.0$ on the tension side of the bend, as determined from the bend radius and wire thickness [10]. And there is no visible evidence of cracking on this surface despite the highly strained outer fibers (**Fig.6.2**). Based on this attribute seen in the bend test, the wires should also have a higher ductility in tension compared to the H19 temper at similar strength [10]. Further work is needed to establish, more quantitatively, the origins of this high ductility. It is hypothesized that this high ductility is a consequence of strong crystallographic shear textures imposed in the wire by the machining [45], unlike the case of rolling or drawing [125,126].

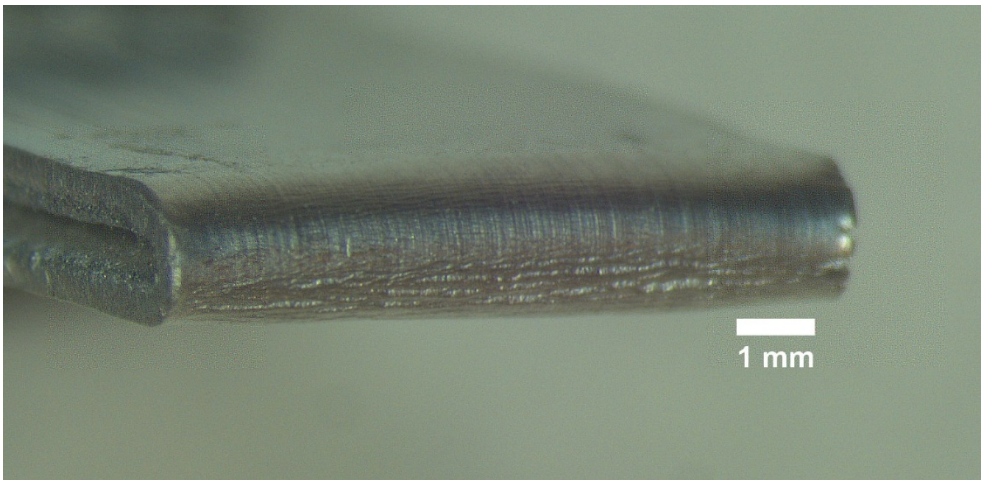

Fig. 6.2 Large formability of the FM wire as illustrated by bending to "zero radius" in 0T bend test.

Electrical Properties

Aluminum alloys in the 1xxx, particularly, Al1100, EC1350 and Al1370, are the main commercially pure aluminum alloys used in electrical conductor applications, because of their high electrical conductivity and inherent capability to be strengthened by cold-working. In the annealed (O-temper) condition, these alloys have very low strength (UTS < 90 MPa), but high ductility (elongation > 40% in 50 mm) and high electrical conductivity (57 – 62 % IACS, depending on purity) [10]. This low strength precludes their direct use in the annealed (or as-cast) condition in many electrical applications. Therefore, various strain-hardened tempers, ranging from H12 (quarter-hard) to H18 (full-hard) and H19 (extra-hard), to improve strength, have been developed utilizing plastic deformation techniques such as wire drawing and rolling [8,9]. Strain hardening is the preferred mode of strengthening, as it does not significantly reduce the electrical conductivity, in contrast to solid solution strengthening. This is due primarily to the low potency of dislocations to cause scattering of conducting electrons [127,128]. This small effect of plastic deformation on conductivity is consistent with the measured data in the FM and HCE wires (**Table 6.2**). Only a very small decrease (< 5%) in electrical conductivity, with respect to the annealed condition, occurs in wires produced both by the single-step, shear-based processes and the multi-step, conventional processes. On the other hand, the effect of the chemical composition on conductivity is much greater. Due to its lower impurity content (Fe + Si = 0.5 wt% max), the

EC1350 shows a much higher electrical conductivity (63.5 IACS) in the annealed condition than the Al 1100 (57.9 IACS). Thus, for purposes of strengthening without compromising on electrical conductivity through application of high plastic strains, the efficacy of the single-step FM and HCE techniques cannot be overemphasized.

Surface Finish

The surface roughness as measured in terms of the arithmetic mean height (R_a) for the FM and HCE wires are summarized in Table 6.3. The R_a for the FM back surfaces are somewhat rough (Ra > 4 μm) especially when compared with the finish limits for commercially drawn flat wires (R_a = 0.8 to 3.3 μm) [90], and for rolled products (0.4 to 0.8 μm) [105,106]. The rake faces of the FM wires, however, have much smaller R_a values, between 0.24 and 0.31 μm (**Table 6.3**), for both the Al 1100 and EC1350 alloy. This is more than an order of magnitude smaller than the R_a on the FM wire free surface, and far superior to that of drawn or rolled products.

In HCE, the constraint greatly reduces the surface roughness (R_a = 0.36 μm and 0.32 μm) on the wire free surface (**Table 6.3**), compared to that in the FM. These roughness values are in fact close to that recorded (R_a = 0.25 μm and 0.23 μm) on the wire rake-face sides in both alloys. It also shows that the constrained surface has very similar roughness to that on the rake face. Overall, the HCE wire surface roughness is superior to that of strip products by cold rolling or drawing [105].

Table 6.3 Summary of the surface roughness values (R_a (μm)) for FM and HCE wires. RF is rake face, FS is wire free surface, and CS is the constrained surface in HCE.

	FM		**HCE**	
	RF	**FS**	**RF**	**CS**
EC 1350	0.31	8.9	0.25	0.36
Al 1100	0.24	4.5	0.23	0.32

Since one (back) surface of the FM wires is quite rough relative to drawn/rolled products, utilizing the potential high ductility in the FM wires, small drawing reductions to the wires, post FM, was investigated as a means of improving the surface finish. This combined process is termed FM + D process. **Figure 6.3** shows FM Al 1100 alloy wire after a small 20% cold-drawing reduction using a tool steel draw plate with rectangular die openings. The mushroom-like structures on the original

wire free surface are nearly completely eliminated. Surface profilometry showed a reduction in the free surface roughness from ~4.5 µm R_a (initial FM condition) to 0.93 µm R_a in the FM + D condition **(Fig. 6.3b)**. This is well within the range of commercial wire products [28], as discussed earlier. Interestingly, the mushroom-like features at the free surface do not bend or fold due to the drawing. Likewise, no significant changes in the FM flow line profiles occur after drawing, nor are any fractures observed. These observations show that the FM wires, despite the high degree of strain-hardening by the cutting shear-deformation, still have significant residual workability and can be drawn to substantial reductions if needed. This workability is most likely a consequence of favorable shear textures imposed by the cutting process [45]. Thus, applying a secondary process such as drawing, with small reduction (<20%), provides a practical route to producing FM wire with surface similar to commercial wire products. However, this finish is still inferior to HCE wire products. Although the FM + D process uses an additional processing stage beyond FM for improving surface finish, it still offers substantial reduction in number of processing steps vis-a-vis rolling/drawing. The latter processes require at least 10 steps, to reduce a standard wire rod, 9.8 mm initial diameter, at a typical reduction of 35% per pass, to a wire product of equivalent dimensions as the FM + D wire.

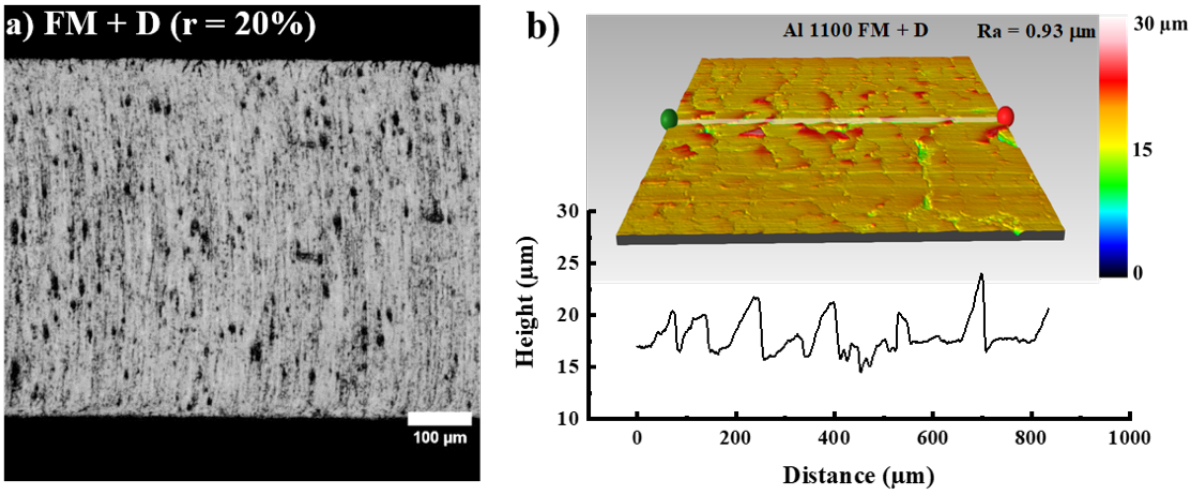

Fig. 6.3 Al 1100 FM wire (as in Fig. 5a) after small 20% drawing reduction through a rectangular die (a) optical micrograph (b) surface profile of free surface of wire.

7. SUMMARY AND FUTURE WORK

7.1 Summary

Two machining-based processes, Hybrid Cutting Extrusion (HCE) and Free Machining (FM), are demonstrated for single-step, shear-based deformation processing of commercially pure aluminum alloys. Long, continuous chips of varying dimensions can be produced in a single step by these processes. With the FM process, while one of the chip surfaces is quite smooth, the other back surface of the chip can have roughness higher than that of commercial rolled/drawn sheet products. Detailed analysis through high-speed imaging, microscopy and particle image velocimetry, PIV revealed the chip back surface roughness is a consequence of the nature of the flow of the material during the deformation. The material flow mode spawn plastic instabilities such as multiscale fold formation during the deformation. Although flow instabilities generally occur in machining, the multi-scale folds (i.e., the high-frequency lamella (mushroom-like) structures, and the low-frequency, large amplitude folds) in the commercially pure aluminum alloys are uniquely different compared to other instabilities seen in materials such as Cu, brass, Ti- alloys and steel.

Controlling the flow behavior is essential to producing good chips using the shear-based processes outlined above. In examining the nature of material flow, two independent phenomena that are uniquely peculiar to the soft and ductile commercially pure aluminum alloys are identified to work in tandem to orchestrate the formation of the flow instabilities; a sinuous flow phenomenon which relates to the formation of high-frequency lamella (mushroom-like) structures, and stick-slip phenomenon, which is associated with the formation of low-frequency, large amplitude folds.

These mechanisms governing the flow and fold formation outline the difficulty in cutting the very soft and ductile metals. Besides the obvious impairment of the surface quality of the chips, the occurrence of the folds is often accompanied by high cutting forces, thus, high deformation energies and accelerated tool wear. Hence, the need for suppressing or possibly eliminating these mechanisms that promote the flow instabilities became ever important. This was achieved through the use of two strategies: 1) modifying cutting conditions and 2) using constrained deformation by HCE. All of these strategies involved the modification of the deformation zone geometry to suppress the flow instabilities.

Modifying the cutting conditions was targeted at eliminating initial plastic bump formation during sinuous flow altering the chip-tool contact and friction conditions during stick-slip. These were achieved by increasing the rake angle to more positive configuration for less rigorous interaction with the workpiece and increasing the cutting speed to reduce the friction at the chip-tool interface. Combining the rake angle and cutting speed resulted in the creation of a process map containing the likely chip morphology that may arise at any given cutting condition due to the dominant flow mechanism associated with that condition. The process map also allows for the selection of optimal cutting conditions based on the tradeoffs between strain and surface finish.

The use of HCE is another untried method for flow suppression in the commercially pure alloys. By applying a sufficient constraint to the chip back surface, the degree of freedom available for flow development within the deformation zone is removed. This is what is done naturally in HCE by adjusting the constraint level (λ) in the deformation zone. The HCE constraint greatly reduces the surface roughness compared to that in the FM and the smooth rake face side of the chip. The very good surface finishes resulting from HCE offered a promising pathway for producing strips directly from annealed/as-cast workpieces, with significantly reduced processing steps compared to traditional wire processing routes.

Implications of the processes were demonstrated in the production of flat electrical conductor wires. The wires produced by the shear-based processes were compared to H18 or H19 commercial wires of the alloys and the results are promising. The FM and HCE wires exhibit better or comparable properties with the conventional counterparts in the three key property performance measures for wires, i.e., strength, conductivity, and surface finish. In relation to strength, the imposition of deformation strains of up to 4 in the shear-based processing, caused a remarkable increase in strength without compromising on electrical conductivity. HCE, as a process, is more flexible than FM or multistage cold rolling, since the wire thickness and strain can be independently controlled; and a range of microstructures, from highly cold-worked to partially annealed, can be produced by varying the deformation-induced heating. The wires even in the highly strain-hardened condition are found to possess sufficient formability, thus making them amenable to secondary processing through wire drawing or rolling. Although the FM wires required light secondary processing to improve surface finish, the HCE wires are demonstrated to be superior to the cold-rolled/drawn wires.

The results thus show that the shear-based processing can be used to produce wire and sheet products with high strength, conductivity, and formability, all in a single step of deformation in the pure and soft aluminum alloys. The wires/sheets can also be used as half-products for further processing by conventional forming methods. The single-step, shear-based processing framework likely uses less energy and has smaller production cost.

7.2 Future Work

The chips (strips and wires) produced by the shear-based processes were quite narrow (3 – 8 mm in width) and looking ahead, a scale up of the process should be the next target. However, increased dimensions of the strips will be accompanied by different challenges such as strip straightness and camber that would need to be resolved. Some of these challenges can be subdued by incorporating a tension mechanism to the FM and HCE setups that will apply the right amount of tension on the strip during the cutting process. A potential benefit of applying tension will be reduced cutting forces and increased tool life.

Optimization of the cutting processes requires a suppression of the mechanisms that promote flow instabilities (Sinuous flow and stick-slip). It has been demonstrated that these mechanisms are dominant at cutting conditions that enhance extended tool life, i.e., low cutting speeds and low rake angles. At optimized cutting conditions (medium-to-high cutting speeds and rake angles), the cutting tools are vulnerable to accelerated wear. Although accelerated tool wear in cutting the soft alloy is less likely, cutting at high rake angles and speeds increases the likelihood of tool damage and therefore, registers a need to characterize the tool wear and tool life in both FM and HCE.

The origins of the high formability of the FM chips still requires further work to establish it quantitatively. It is hypothesized that this high ductility is a consequence of strong crystallographic shear textures imposed in the chip by machining [45], unlike the case of rolling or drawing [125,126]. Texture analysis of the FM chips, therefore, is prudent to understanding this property.

The reduction in the number of processing passes to just a single pass in FM and HCE promises a significant decrease in the amount of resources required to produce the strip. Energy requirements are anticipated to be low compared to the traditional multi-step processes, thus, cost of producing strips is expected to be low. An economic analysis of the FM and HCE processes in a scale up,

will provide invaluable information into the suitability of commercializing the processes.

REFERENCES

[1] Olivares-Galván, J. C., De León, F., Georgilakis, P. S., and Escarela-Pérez, R., 2010, "Selection of Copper against Aluminium Windings for Distribution Transformers," IET Electr. Power Appl., **4**(6), pp. 474–485.

[2] Helms, H., and Lambrecht, U., 2007, "The Potential Contribution of Light-Weighting to Reduce Transport Energy Consumption," Int J Life Cycle Assess, **12**(1), pp. 58–64.

[3] Hinrich Helms, U. L., 2004, "Energy Savings by Light-Weighting - II Final Report," (June).

[4] Skillingberg, M., and Green, J., 2007, "Aluminum Applications in the Rail Industry," Light Met. Age, (October).

[5] Directorate, O. E., 2010, "OECD Global Forum on Environment Focusing on Sustainble Materials Case Study 2 : Aluminium," Environment, (October), p. 66.

[6] MacKenzie, G. E. T. and D. S., 2016, "Aluminum Alloy Nomenclature and Temper Designations," *ASM Handbook, Heat Treating of Nonferrous Alloys*, pp. 114–136.

[7] Cayless, R. B. C., Rolled, A., and Company, P., 2018, "Alloy and Temper Designation Systems for Aluminum and Aluminum Alloys," Prop. Sel. Nonferrous Alloy. Spec. Mater., **2**, pp. 15–28.

[8] Altenpohl, D. G., 1998, *Aluminum-Technology, Applications, and Environment : A Profile of a Modern Metal : Aluminum from within-the Sixth Edition*, Washington, D.C. : Aluminium Association, Washington, D.C. : Warrendale, Pa.

[9] Kaufman, J. G., 2000, *Introduction to Aluminium Alloys and Tempers*, ASM International, Materials Park, OH.

[10] ASM International Handbook Committee, 2001, "Metals Handbook Vol 2: Properties and Selection: Nonferrous Alloys and Special-Purpose Materials," ASM Int.

[11] Kustas, A. B., Sagapuram, D., Trumble, K. P., and Chandrasekar, S., 2016, "Texture Development in High-Silicon Iron Sheet Produced by Simple Shear Deformation," Miner. Met. Mater. Soc. ASM Int., **47**(A), pp. 3095–3108.

[12] Sagapuram, D., Kustas, A. B., Dale Compton, W., Tumble, K. P., and Chandrasekar, S., 2015, "Direct Single-Stage Processing of Lightweight Alloys Into Sheet by Hybrid Cutting–Extrusion," ASME J. Manuf. Sci. Eng., **137**, pp. 051002-1–10.

[13] Efe, M., Moscoso, W., Trumble, K. P., Dale Compton, W., and Chandrasekar, S., 2012, "Mechanics of Large Strain Extrusion Machining and Application to Deformation Processing of Magnesium Alloys," Acta Mater., **60**, pp. 2031–2042.

[14] Nakayama, K., 1974, "The Formation of 'Saw-Toothed Chip' in Metal Cutting," Proc. Int. Conf. Prod. Eng. Tokyo, pp. 572–576.

[15] Edward Trent, P. W., 2000, *Metal Cutting*, butterworth-Heinemann, Oxford.

[16] Clayton, M. C. M., 2006, "Metal Cutting Principles . Public Domain , Google-Digitized," pp. 1915–2006.

[17] Thomas childs, Katsuhiro Maekawa, Toshiyuki Obikawa, Y. Y., 2000, *Metal Machining Theory and Applications*, John Wiley & Sons Inc., New York.

[18] CNC, "CNC Cookbook: Dictionary" [Online]. Available: https://www.cnccookbook.com/cnc-dictionary/. [Accessed: 04-Feb-2021].

[19] Glossary, A. words, "Machining Glossary Terms" [Online]. Available: https://www.allwords.com/machining-glossary-164-594.php. [Accessed: 04-Feb-2021].

[20] Shi, H., 2018, *Metal Cutting Theory: New Perspectives and New Approaches*, Springer, Ottawa, Canada.

[21] Laboratory, F. P., 2010, *Wood Handbook: Wood as an Engineering Material*, USDA Forest Service, Madison, Wisconsin.

[22] David A. Stephenson, J. S. A., 2016, *Metal Cutting Theory and Practice*, CRC Press _ Taylor & Francis Group, New York.

[23] MacLeod, C., 2003, "Henry Maudslay and the Pioneers of the Machine Age.," Bus. Hist. Rev., p. 192.

[24] Woodbury, R. S., 1960, "The Legend of Eli Whitney and Interchangeable Parts," **1**(3), pp. 235–253.

[25] Woodbury, R. S. ., 1963, "The Origins of the Lathe," Sci. Am., **208**(4), pp. 132–143.

[26] Ashby, M., Shercliff, H., and Cebon, D., 2010, *Materials: Engineering, Science, Processing and Design*.

[27] Ortner, H. M., Ettmayer, P., and Kolaska, H., 2014, "The History of the Technological Progress of Hardmetals," Int. J. Refract. Met. Hard Mater.

[28] Fan, Y., Hao, Z., and Zheng, M., 2013, "Study of Surface Quality in Machining Nickel-Based Alloy," Int J Adv ManufTechnol, **69**, pp. 2659–2667.

[29] I. A Choudhury, M. . . E.-B., 1998, "Machining Nickel Base Superalloys : Inconel 718," Proc Instn Mech Engrs, **212**(B), pp. 195–206.

[30] Huang, H., and Liu, Y. C., 2003, "Experimental Investigations of Machining Characteristics and Removal Mechanisms of Advanced Ceramics in High Speed Deep Grinding," Int. J. Mach. Tools Manuf., **43**, pp. 811–823.

[31] 2006, *Handbook of Advanced Ceramics Machining*.

[32] Astakhov, V. P., 2005, "On the Inadequacy of the Single-Shear Plane Model of Chip Formation," Int. J. Mech. Sci., **47**(11), pp. 1649–1672.

[33] Merchant, M. E., 1945, “Mechanics of the Metal Cutting Process. I. Orthogonal Cutting and a Type 2 Chip,” J. Appl. Phys., **16**(5), pp. 267–275.

[34] Bryant, M. D., “Approach : Merchant ’ s Cutting Model,” pp. 1–15.

[35] Shaw, M. C., 2005, *Metal Cutting Principles*, Oxford University Press Inc, New York.

[36] Sagapuram, D., Udupa, A., Viswanathan, K., Mann, J. B., M’Saoubi, R., Sugihara, T., and Chandrasekar, S., 2020, “On the Cutting of Metals: A Mechanics Viewpoint,” ASME J. Manuf. Sci. Eng., **142**, pp. 110808-1–19.

[37] Vyas, A., and Shaw, M. C., 1999, “Mechanics of Saw-Tooth Chip Formation in Metal Cutting,” J. Manuf. Sci. Eng., **121**, pp. 163–172.

[38] Srinivasan Chandrasekar, Kevin Trumble, Wilfredo Moscoso, Mert Efe, D. S., Christopher J. Saldana, and Mann, James Bradley, W. D. C., 2014, “LARGE STRAIN EXTRUSION MACHINING PROCESSES AND BULK FORMS PRODUCED THEREFROM,” **US 2014/00**.

[39] De Chiffre, L., 1983, “Extrusion Cutting of Brass Strips,” Int. J. Mach. Tool Des. Res., **23**(2/3), pp. 141–151.

[40] Viswanathan, K., Udupa, A., Yeung, H., Sagapuram, D., Mann, J. B., Saei, M., and Chandrasekar, S., 2017, “On the Stability of Plastic Flow in Cutting of Metals,” CIRP Ann. - Manuf. Technol., **66**(1), pp. 69–72.

[41] Efe, M., 2012, “Extrusion Machining: A Thermo-Mechanical Process for Producing Htrips of Alloys Having Limited Workability,” Purdue University.

[42] Hosford, W. F., and Caddell, R. M., 2007, *Metal Forming: Mechanics and Metallurgy*, Cambridge University Press, NY.

[43] Hoshi, T., and Shaw, M. C., 1977, “Cut-Forming: A New Method of Producing Wire,” ASME J. Eng. Ind. Trans., pp. 225–228.

[44] M. N. Issahaq, S. Chandrasekar, K. P. T., 2020, “Single-Step Shear-Based Deformation Processing of Electrical Conductor Wires,” ASME J. Manuf. Sci. Eng.

[45] Sagapuram, D., Efe, M., Moscoso, W., Chandrasekar, S., and Trumble, K. P., 2013, “Controlling Texture in Magnesium Alloy Sheet by Shear-Based Deformation Processing,” Acta Mater., **61**, pp. 6843–6856.

[46] Kustas, A. B., 2015, “Shear-Based Deformation Processing and Characterization of Electrical Steel Sheet,” Purdue University.

[47] Hatch, J. E., 1984, “MicroStructure of Alloys,” *Aluminum Properties and Physical Metallurgy*, pp. 58–104.

[48] ASM International Handbook, V. 2, 1990, “Properties and Selection: Nonferrous Alloys and Special-Purpose Materials,” ASM Met. Handb., **2**, p. 1300.

[49] H. Okamoto, M.E. Schlesinger, and E. M. M., 2016, "Al (Aluminum) Binary Alloy Phase Diagrams," *ASM Handbook*, pp. 113–139.

[50] ASTM-B193-02, 2014, *Standard Test Method for Resistivity of Electrical Conductor Materials*.

[51] A.V Asting, 1956, *Copper Wire Tables, Google-Digitized*, U. S Government Printing Office, Washington.

[52] Shaw, M. C., Dirke, S. O., Smith, P. A., Cook, N. H., Loewen, E. G., and Y., and C. T., 1954, *Machining Titanium : A Report Prepared for the United States Air Force*.

[53] Rice, W. B., 1961, "The Formation of Continuous Chips in Metal Cutting," Can. J., pp. 41–45.

[54] Sagapuram, D., and Viswanathan, K., 2018, "Evidence for Bingham Plastic Boundary Layers in Shear Banding of Metals," Extrem. Mech. Lett, (25), pp. 27–36.

[55] Merchant, M. E., Krabacher, E. J., Young, H. W., and Miller, J. H., 1954, "Titanium Is Unorthodox When Machined...Here's Why," Am. Mach, (98), p. 118.

[56] Recht, R. F., 1964, "Catastrophic Thermoplastic Shear," ASME J. Appl. Mech. Trans., **31**(2), pp. 189–193.

[57] Davies, M. A., Burns, T. J., and Evans, C. J., 1997, "On the Dynamics of Chip Formation in Machining Hard Metals," CIRP Ann., **46**(1), pp. 25–30.

[58] Komanduri, R., and Hou, Z. B., 2002, "On Thermoplastic Shear Instability in the Machining of a Titanium Alloy (Ti-6Al-4V)," Metall. Mater. Trans. A Phys. Metall. Mater. Sci., **33**(9), pp. 2995–3010.

[59] Vandana, A. S., and Sundaram, N. K., 2018, "Simulation of Sinuous Flow in Metal Cutting," Tribol. Lett., **66**(3), p. 94.

[60] Williams, J. E., Smart, E. F., and Milner, D. R., 1970, "The Metallurgy of Machining. Part I: Basic Considerations and the Cutting of Pure Metals," Metallurgia, **81**(483), pp. 3–10.

[61] Yeung, H., Viswanathan, K., Compton, W. D., and Chandrasekar, S., 2015, "Sinuous Flow in Metals," Proc. Natl. Acad. Sci., **112**(32), pp. 9828–9832.

[62] Raffel, M., Willert, C. E., Wereley, S. T., Kompenhans, J., Willert, S., Wereley, S. T., and Kompenhans, J., 2007, *Particle Image Velocimetry: A Practical Guide*.

[63] Pan, B., Qian, K., Xie, H., and Asundi, A., 2009, "Two-Dimensional Digital Image Correlation for in-Plane Displacement and Strain Measurement: A Review," Meas. Sci. Technol., **20**(6).

[64] Guo, Y., Compton, W. D., and Chandrasekar, S., 2015, "In Situ Analysis of Flow Dynamics and Deformation Fields in Cutting and Sliding of Metals," Proc. R. Soc. A Math. Phys. Eng. Sci., **471**(2178).

[65] Dabade, U. A., Dapkekar, D., and Joshi, S. S., 2009, "Modeling of Chip-Tool Interface Friction to Predict Cutting Forces in Machining of Al/SiCp Composites," Int. J. Mach. Tools Manuf., **49**(9), pp. 690–700.

[66] Bahi, S., List, G., and Sutter, G., 2016, "Modeling of Friction along the Tool-Chip Interface in Ti6Al4V Alloy Cutting," Int. J. Adv. Manuf. Technol., **84**(9–12), pp. 1821–1839.

[67] Marinov, V. R., 2001, "Hybrid Analytical-Numerical Solution for the Shear Angle in Orthogonal Metal Cutting - Part I: Theoretical Foundation," Int. J. Mech. Sci., **43**(2), pp. 399–414.

[68] Carvalho, S. R., Lima e Silva, S. M. M., Machado, A. R., and Guimarães, G., 2006, "Temperature Determination at the Chip-Tool Interface Using an Inverse Thermal Model Considering the Tool and Tool Holder," J. Mater. Process. Technol., **179**(1–3), pp. 97–104.

[69] Karagöz, S., and Fischmeister, H. F., 1996, "Metallographic Observations on the Wear Process of TiN-Coated Cutting Tools," Surf. Coatings Technol.

[70] Brocail, J., Watremez, M., Dubar, L., and Bourouga, B., 2008, "Contact and Friction Analysis at Tool-Chip Interface to High-Speed Machining," Int. J. Mater. Form., **1**(SUPPL. 1), pp. 1407–1410.

[71] Fatima, A., and Mativenga, P. T., 2013, "A Review of Tool-Chip Contact Length Models in Machining and Future Direction for Improvement," Proc. Inst. Mech. Eng. Part B J. Eng. Manuf.

[72] Hwang, J., and Chandrasekar, S., 2011, "Contact Conditions at the Chip-Tool Interface in Machining," Int. J. Precis. Eng. Manuf., **12**(2), pp. 183–193.

[73] Ackroyd, B., Akcan, N. S., Chhabra, P., Krishnamurthy, K., Madhavan, V., Chandrasekar, S., Compton, W. D., and Farris, T. N., 2001, "Exploration of Contact Conditions in Machining," Proc. Inst. Mech. Eng. Part B J. Eng. Manuf., **215**(4), pp. 493–507.

[74] Bahi, S., Nouari, M., Moufki, A., Mansori, M. El, and Molinari, A., 2012, "Hybrid Modelling of Sliding-Sticking Zones at the Tool-Chip Interface under Dry Machining and Tool Wear Analysis," Wear, **286**–**287**, pp. 45–54.

[75] Udupa, A., Viswanathan, K., Ho, Y., and Chandrasekar, S., 2017, "The Cutting of Metals via Plastic Buckling," Proc. R. Soc. A Math. Phys. Eng. Sci., **473**(2202), p. 20160863.

[76] Chaudhari, A., Soh, Z. Y., Wang, H., and Kumar, A. S., 2018, "Rehbinder Effect in Ultraprecision Machining of Ductile Materials," Int. J. Mach. Tools Manuf., **133**(March), pp. 47–60.

[77] Gad, G. S., Armarego, E. J. A., and Smithj, A. J. R., 1992, "Tool-Chip Contact Length in Orthogonal Machining and Its Importance in Tool Temperature Predictions," Int. J. Prod. Res.

[78] Iqbal, S. A., Mativenga, P. T., and Sheikh, M. A., 2009, "A Comparative Study of the Tool-Chip Contact Length in Turning of Two Engineering Alloys for a Wide Range of Cutting

Speeds," Int. J. Adv. Manuf. Technol.

[79] Y. Avevor, A. Moufki, M. N., 2017, "Analysis of the Frictional Heat Partition in Sticking-Sliding Contact for Dry Machining: An Analytical-Numerical Modelling," Procedia CIRP, **58**, pp. 539–542.

[80] Sagapuram, D., Yeung, H., Guo, Y., Mahato, A., M'Saoubi, R., Compton, W. D., Trumble, K. P., and Chandrasekar, S., 2015, "On Control of Flow Instabilities in Cutting of Metals," CIRP Ann. - Manuf. Technol., **64**(1), pp. 49–52.

[81] Sagapuram, D., Viswanathan, K., Mahato, A., Sundaram, N. K., M'Saoubi, R., Trumble, K. P., and Chandrasekar, S., 2016, "Geometric Flow Control of Shear Bands by Suppression of Viscous Sliding," Proc. R. Soc. A Math. Phys. Eng. Sci.

[82] Townend, G. H., 1947, "Direction of Maximum Crystal Elongation during Metal Cutting," J. Appl. Phys., **18**, p. 784.

[83] Sahoo, P., 2011, *Surface Topography*, Woodhead Publishing Limited.

[84] Georgios P. Petropoulos, Constantinos N. Pandazaras, J. P. D., 2010, "Surface Texture Characterization and Evaluation Related to Machining," *Surface Integrity in Machining*, Springer-Verlag, pp. 37–66.

[85] Davim, J. P., 2010, *Surface Integrity of Machined Surfaces*, Springer.

[86] Bhushan, B., 2001, "Surface Roughness Analysis and Measurement Techniques," *Modern Tribology Handbook: Volume One: Principles of Tribology*, CRC Press LLC, pp. 49–119.

[87] Manske, E., Jäger, G., Hausotte, T., and Fül, R., 2012, "Recent Developments and Challenges of Nanopositioning and Nanomeasuring Technology," Meas. Sci. Technol., **23**(7).

[88] Jiang, X., Scott, P. J., Whitehouse, D. J., and Blunt, L., 2007, "Paradigm Shifts in Surface Metrology. Part II. The Current Shift," Proc. R. Soc. A Math. Phys. Eng. Sci., **463**, pp. 2071–2099.

[89] Schwenke, H., Härtig, F., Wendt, K., and Wäldele, F., 2001, "Future Challenges in Co-Ordinate Metrology: Addressing Metrological Problems for Very Small and Very Large Parts," Proc. IDW Conf. Knoxv., pp. 1–12.

[90] Dagnall, H., 1986, *Exploring Surface Texture*, Rank Taylor Hobson Ltd, Leicester, England.

[91] Aver'yanova, I. O., Bogomolov, D. Y., and Poroshin, V. V., 2017, "ISO 25178 Standard for Three-Dimensional Parametric Assessment of Surface Texture," Russ. Eng. Res., **37**(6), pp. 513–516.

[92] ASME-B46.1, 2019, *Surface Texture, Surface Roughness, Waviness and Lay*.

[93] Stout, K. J., Davis, E. J., and Sullivan, P. J., 1990, *Atlas of Machined Surfaces*.

[94] Davim, J. P., 2013, *Tribology in Manufacturing Technology*.

[95] Whitehouse, D. J., 2011, *Handbook of Surface and Nanometrology*.

[96] ISO 25178 Series, 2010, "Geometric Product Specifications (GPS) – Surface Texture: Areal," Int. Organ. Stand.

[97] Anon, 1978, "SURFACE TEXTURE (SURFACE ROUGHNESS, WAVINESS AND LAY).," ANSI Stand B46. 1.

[98] Alcock, S. G., Ludbrook, G. D., Owen, T., and Dockree, R., 2010, "Using the Power Spectral Density Method to Characterise the Surface Topography of Optical Surfaces," Proc. SPIE, **7801**(July), pp. 780108-1–8.

[99] Gong, Y., Misture, S. T., Gao, P., and Mellott, N. P., 2016, "Surface Roughness Measurements Using Power Spectrum Density Analysis with Enhanced Spatial Correlation Length," J. Phys. Chem. C, **120**(39), pp. 22358–22364.

[100] Jacobs, T. D. B., Junge, T., and Pastewka, L., 2017, "Quantitative Characterization of Surface Topography Using Spectral Analysis," Surf. Topogr. Metrol. Prop.

[101] Features, S., 2018, "Power Spectral Density (PSD) PSD and Surface Features," (800), pp. 1–8.

[102] Elson, J. M., and Bennett, J. M., 1995, "Calculation of the Power Spectral Density from Surface Profile Data," Appl. Opt., **34**(1), pp. 201–208.

[103] Lorbeer, R. A., Pastow, J., Sawannia, M., Klinkenberg, P., Förster, D. J., and Eckel, H. A., 2017, "Power Spectral Density Evaluation of Laser Milled Surfaces," Materials (Basel)., **11**(1), pp. 1–10.

[104] Vorbuguer, T.V., J. R., 1990, "Surface Finish Metrology Tutorial," Natl. Inst. Stand. Technol., pp. 1–159.

[105] Le, H. R., and Sutcliffe, M. P. F., 2000, "Analysis of Surface Roughness of Cold-Rolled Aluminium Foil," Wear, **244**, pp. 71–78.

[106] Tingting Mao, T. A., 2013, "Aluminum Sheet Forming for Automotive Applications, Part II," Stamp. J., pp. 12–13.

[107] Emley, E. F., 1976, "Continuous Casting of Aluminium," Int. Met. Rev., **21**(1), pp. 75–115.

[108] Wang, J., 2018, "Aluminum Alloy Ingot Casting and Continuous Processes," ASM Met. Handb., **2A**, pp. 108–115.

[109] Prysmian Group, 2019, *Report on Aluminum Rod*, Highland Heights, KY, United States.

[110] ASTM-B324-01, 2016, *Standard Specification for Aluminum Rectangular and Square Wire for Electrical Purposes.*

[111] ASTM-B230/B230M-07, 2012, *Standard Specification for Aluminum 1350–H19 Wire for Electrical Purposes*.

[112] Properzi, I., 1955, "Continuous Metal Casting Machine," United States Pat. Off., **2,710,433**.

[113] Dieter, G. E., 1988, *Mechanical Metallurgy.*, McGraw-Hill, NY.

[114] Horita, Z., Fujinami, T., and Langdon, T. G., 2001, "The Potential for Scaling ECAP - Effect of Sample Size on Grain Refinement and Mechanical Properties.," Mater. Sci. Eng. A, **318**, pp. 34–41.

[115] El-Danaf, E. A., Soliman, M. S., Almajid, A. A., and El-Rayes, M. M., 2007, "Enhancement of Mechanical Properties and Grain Size Refinement of Commercial Purity Aluminum 1050 Processed by ECAP," Mater. Sci. Eng. A, **458**, pp. 226–234.

[116] Azushima, A., Kopp, R., Korhonen, A., Yang, D. Y., Micari, F., Lahoti, G. D., Groche, P., Yanagimoto, J., Tsuji, N., Rosochowski, A., and Yanagida, A., 2008, "Severe Plastic Deformation (SPD) Processes for Metals," CIRP Ann. - Manuf. Technol., **57**, pp. 716–735.

[117] Azimi, A., Tutunchilar, S., Faraji, G., and Besharati Givi, M. K., 2012, "Mechanical Properties and Microstructural Evolution during Multi-Pass ECAR of Al 1100-O Alloy," Mater. Des., **42**, pp. 388–394.

[118] Raab, G. J., Valiev, R. Z., Lowe, T. C., and Zhu, Y. T., 2004, "Continuous Processing of Ultrafine Grained Al by ECAP-Conform," Mater. Sci. Eng. A, **382**, pp. 30–34.

[119] Green, D., 1972, "Continuous Extrusion-Forming of Wire Sections.," J Inst Met, **100**, pp. 295–300.

[120] Xu, C., Schroeder, S., Berbon, P. B., and Langdon, T. G., 2010, "Principles of ECAP-Conform as a Continuous Process for Achieving Grain Refinement: Application to an Aluminum Alloy," Acta Mater., **58**, pp. 1379–1386.

[121] Fakhretdinova, E., Raab, G., Ryzhikov, O., and Valiev, R., 2014, "Processing Ultrafine-Grained Aluminum Alloy Using Multi-ECAP-Conform Technique," *IOP Conference Series: Materials Science and Engineering*.

[122] Dobatkin, S., Zrnik, J., and Mamuzic, I., 2010, "Development of SPD Continuous Process for Strip and Rod Production," Metalurgija, **49**(4), pp. 343–347.

[123] ASTM-E140, 2013, *Standard Hardness Conversion Tables for Metals Relationship Among Brinell Hardness , Vickers Hardness , Rockwell Hardness , Superficial Hardness , Knoop Hardness , Scleroscope Hardness , and Leeb Hardness 1*.

[124] Zhang, P., Li, S. X., and Zhang, Z. F., 2011, "General Relationship between Strength and Hardness," Mater. Sci. Eng. A, **529**, pp. 62–73.

[125] Liu, W. C., and Morris, J. G., 2004, "Quantitative Analysis of Texture Evolution in Cold-Rolled, Continuous-Cast AA 5xxx-Series Aluminum Alloys," Metall. Mater. Trans. A Phys. Metall. Mater. Sci., **35**, pp. 265–277.

[126] Hirsch, J., and Al-Samman, T., 2013, "Superior Light Metals by Texture Engineering: Optimized Aluminum and Magnesium Alloys for Automotive Applications," Acta Mater.,

61(3), pp. 818–843.

[127] Çetinarslan, C. S., 2009, "Effect of Cold Plastic Deformation on Electrical Conductivity of Various Materials," Mater. Des., **30**, pp. 671–673.

[128] Islamgaliev, R. K., Nesterov, K. M., Champion, Y., and Valiev, R. Z., 2014, "Enhanced Strength and Electrical Conductivity in Ultrafine-Grained Cu-Cr Alloy Processed by Severe Plastic Deformation," *IOP Conference Series: Materials Science and Engineering*.

VITA

MOHAMMED NAZIRU ISSAHAQ
https://www.linkedin.com/in/issahaq-mohammed-naziru-b555a05b

EDUCATION

Ph.D., Materials Engineering 2016 - 2021
School of Materials Engineering
Purdue University, West Lafayette, IN.

B.S. Mining Engineering 2008 – 2012
Faculty of Minerals Resources Technology
University of Mines and Technology, Tarkwa, Western Region, Ghana,

RESEARCH / TEACHING EXPERIENCE

Graduate Research Assistant *Aug. 2016 to May 2021.*
Purdue University, West Lafayette, IN,

Graduate Teaching Assistant
Purdue University, West Lafayette, IN.
Courses Taught:

- Structure and Properties of Materials Spring 2019, Fall 2020
- Additive Manufacturing of Materials Spring 2021

PROFESSIONAL EXPERIENCE

Graduate Data Mine Researcher *Aug. 2020 to Dec. 2020*
CAT Digital / The Data Mine - Purdue University, West Lafayette, IN.

Mine Operations Superintendent *Sep. 2014 to July 2016.*
MAXMASS Ltd, Tarkwa, Western Region, Ghana.

Business Improvement Analyst *Aug. 2012 to Feb. 2014.*
Goldfields Ghana Ltd (GFGL), Tarkwa, Western Region, Ghana.

CONFERENCE PRESENTATIONS

The Minerals, Metals & Materials Society (TMS) Conference, San Diego, CA. Feb. 2020.
"Production of Commercially Pure Aluminum Strips via Single-Step, Shear-Based Techniques"

The Minerals, Metals & Materials Society (TMS) Conference, San Antonio, TX. March 2019.
"Surface Morphology of Commercially Pure Aluminum Electrical Conductor Wires Produced via Single-Step Machining-Based Techniques."

Materials Science & Technology (MS &T) Conference, Pittsburgh, PA. Oct. 2017.
"Shear-Based Processes for the Production of Strong Aluminum Electrical Conductors"

LEADERSHIP AND SERVICE

Secretary, Material Science and Engineering Graduate Students Association (MSEGSA).
Purdue University, West Lafayette. IN. USA. 2018/2019

Volunteer, MSEGSA Outreach on Materials Science / Renewable Energy
Jefferson High School, Lafayette. IN. USA. Mar. 2019

Volunteer, Materials Engineering Prospective Students Laboratory Tour
Purdue University, West Lafayette. IN. USA. Apr. 2018

PROFESSIONAL AFFILIATIONS AND MEMBERSHIPS

- American Society of Mechanical Engineers, ASME
- National Society of Black Engineers, NSBE Purdue Chapter
- Minority Engineering Program, MEP Purdue.
- Graduate Researchers for International Development, Purdue University
- Association for Iron & Steel Technology, AIST
- ASM International
- Minerals, Metals & Materials Society, TMS
- American Ceramic Society, ACerS

PUBLICATIONS

- M. N. Issahaq, S. Chandrasekar, K. P. Trumble, 2021, "Single-Step Shear-Based Deformation Processing of Electrical Conductor Wires," ASME J. Manuf. Sci. Eng. doi: https://doi.org/10.1115/1.4048984

- A.S Hadi, B. E. Hill, M. N. Issahaq, 2021, "Performance Characteristics of Custom Thermocouples for Specialized Applications", MDPI Crystals, 11(4), 377; https://doi.org/10.3390/cryst11040377

- N. Kedir, J. A. Hernandez, B. H. Lim, J. Gao, X. Zhai, Y. Nie, M. N. Issahaq, T. N. Tallman, W. W. Chen, 2021, "Time dependent response of carbon fiber reinforced plastic (CFRP) to irradiation by a short pulse near-infrared (NIR) laser", J. Laser Appl (Submitted)

- M. N. Issahaq, S. Chandrasekar, K. P. Trumble., "Multiscale Folding in Dry Cutting of Soft Commercially Pure Aluminum", (in draft).

- M. N. Issahaq, M. Saei, S. Chandrasekar, K. P. Trumble., "Suppressing Flow Instabilities in Metal Cutting", (In draft).

- S. P. Rodriguez, M. Saei, M. N. Issahaq, J. Mann, S. Chandrasekar, K. P. Trumble., "Metal Strip Production by Free Machining and Hybrid Cutting Extrusion: A Demonstration, (In draft).